Measurement of the low mass Drell-Yan cross section in the di-muon channel in proton-proton collisions at $\sqrt{s} = 7$ TeV with the ATLAS detector

Elisa Piccaro

A thesis submitted in fulfilment of the requirements of the degree of Doctor of Philosophy to Queen Mary University of London

Supervisor: Dr. Eram Rizvi

Co-Supervisor: Prof. Steve Lloyd

2012

Declaration

The work presented in this thesis is my own. Wherever contributions taken from other sources are involved, they are identified as such. The material produced has not previously been presented in identical or similar form, either in whole or in part, to any other examination board.

To my parents and sister, who only ever ask me to be happy.

Abstract

The low mass Drell-Yan di-muon process is investigated with the ATLAS detector at the LHC, in order to provide information that advances our knowledge of the Parton Density Functions in a region of phase space unaccessible at previous experiments.

A cut-based selection of di-muon events is performed, using 2010 data with a centre of mass energy of the proton-proton collisions of 7 TeV, and an integrated luminosity of $36\,\mathrm{pb}^{-1}$. The analysis probes the region of low muon transverse momentum ($p_T > 6\,\mathrm{GeV}$), and low di-muon mass region $12 < \mathrm{M} < 66\,\mathrm{GeV}$.

The main challenges of the analysis are the understanding of the muon isolation and the trigger efficiency. In order to reject the large QCD background the analysis relies on stringent isolation criteria. The efficiency of the chosen selection is presented in detail. The second main part of the analysis is the measurement of the trigger efficiency for low p_T threshold muon triggers. This is an important aspect of the cross section measurement, since the p_T spectrum of leptons from the low mass Drell-Yan process are soft and populate the trigger threshold region.

In order to measure the differential cross section in mass $\frac{d\sigma}{dM}$ in the fiducial region of $|\eta| < 2.4$ and $p_{T,\mu 1} > 9\,\mathrm{GeV}$ and $p_{T,\mu 2} > 6\,\mathrm{GeV}$ (asymmetric analysis) or $p_{T,\mu 1} > 6\,\mathrm{GeV}$ and $p_{T,\mu 2} > 6\,\mathrm{GeV}$ (symmetric analysis), a one dimensional bin-by-bin unfolding is adopted to account for detector reconstruction and resolution effects; all the associated uncertainties are also presented. The fiducial and extrapolated differential cross sections are measured at the Born level. Dressed level corrections are also given. The measured cross sections are shown to agree with theoretical predictions within the margin of error.

A precision of 9.7% is achieved in the asymmetric analysis in the lowest invariant mass bin between 12 and 17 GeV; the statistical and systematic uncertainties in the same bin are 4.2% and 8.7% respectively. In the remaining mass region the total uncertainty is smaller. The luminosity error during the 2010 data taking period is estimated to be 3.4%.

In addition to the Drell-Yan cross section measurement, the thesis describes the study performed in order to extract the Lorentz angle value in the ATLAS Semiconductor Tracker. The Lorentz angle is computed through the study of the SCT cluster width from both cosmic and collision data and comparison with simulation is shown. The track selection on collision data is defined and the fitting range is optimised to give robust results.

Throughout this thesis the convention $c = 1$ is adopted.

Acknowledgements

I would like to thank my supervisor, Eram, for having taught me what research is all about. His dedication and passion inspired me throughout my PhD. I cannot thank him enough for the time he spent teaching me and answering my questions and doubts. When everything seemed to be wrong and I felt lost, all I had to do was knock on his door and his positiveness would turn the day around, thank you Eram.

Thank you Matilde for being a good friend, and an efficient and helpful colleague. I enjoyed working with you and our social time together.

This is my chance to also thank everyone in the PPRC group, especially Marcella who supervised the LA study and the other PhD students and Post-Docs I have met in the past years. Many thanks to the IT support, for helping me with every problem I had, and special thanks to Alex for reading part of my thesis.

Thank you Jazmina, Kathy and Kate, for your kindness and support with administration. You are really precious to the department and you do a great job.

I would like to thank everyone I worked with in ATLAS, especially people in the Drell-Yan group, for their inputs and help; Dave for trusting me with the TX replacement work in USA15, and the SCT group with whom it has been a pleasure to work with.

Thank you Nick for your help with anything I ever had problems with during my PhD and for reading parts of this thesis.

Thanks to all my friends especially Ali, Ahmed, Chopo, Anita, Sheila, Daniele, Kutub, Tania, Anna and Silvia; you are my dearest friends who share my highs and lows and are always there for me.

Most importantly I would like to thank my family and relatives (especially Giuliana) for supporting and guiding me in all choices I make in life and for standing always by my side.

Thank you!

Contents

List of Figures

List of Tables

Chapter 1

Theory

1.1 The Standard Model

The Standard Model of particle physics (SM) is a theoretical framework which describes the structure of matter and the strong, weak and electromagnetic interactions among fundamental particles (the SM does not describe gravity).

Matter is made of spin-$\frac{1}{2}$ fermions, of which there are three families or generations, each containing two quarks, one charged lepton and a neutrino. According to the SM and to our experimental knowledge these particles are fundamental and therefore have no sub-structure. Ordinary matter is made of fermions in the first generation. A summary of fermions, and their features is shown in Table 1.1. For each fermion there is a corresponding antifermion with same mass and spin and opposite charge. Bound states of quarks are named *hadrons*. They have integer electric charge and are classified into three categories: *baryons*, *antibaryons* and *mesons*. The baryons (antibaryons) are bound states of three quarks (antiquarks) and have half integer spin, whereas the mesons are bound states of a quark and an antiquark and have integer spin.

The model is invariant under local transformations of the gauge symmetry group $SU(3)_C \times SU(2)_L \times U(1)_Y$, where the $SU(3)_C$ group (Quantum Chromodynamics or QCD) describes the strong interactions mediated by eight gluons, and $SU(2)_L \times U(1)_Y$ is the symmetry group of electromagnetic (EM) and electroweak interactions (EW), mediated by photons and by the neutral Z and charged $W^{\pm}$ bosons respectively.

The distinguishing feature of QCD is that it is a non-Abelian gauge theory, in which the gluons carry colour charge. Therefore, unlike the mediators of the electroweak interactions, gluons can interact among themselves.

In the SU_2 gauge theory the Z and $W^{\pm}$ bosons are described but must be mass-

Fermions	Generation						Electric Charge	Interaction
	First		Second		Third			
Quarks	Up	u	Charm	c	Top	t	+2/3	EM, EW, Strong
	Down	d	Strange	s	Bottom	b	-1/3	
Leptons	Electron	e^-	Muon	μ^-	Tau	τ	-1	EM and Weak
	Electron neutrino	ν_e	Muon neutrino	ν_μ	Tau neutrino	ν_τ	0	Weak

Table 1.1: *Generations of fermions in the Standard Model. The electric charge is given in units of the absolute value of the electron's charge $|e|$.*

less. Experimentally their mass has been measured accurately and found to be: $M_{Z^0} = 91.1876 \pm 0.0021\,\text{GeV}$ and $M_{W^\pm} = 80.385 \pm 0.015\,\text{GeV}$ [15]. The Standard Model solves this problem introducing a mechanism in order to break the SU_2 symmetry and a scalar particle called the Higgs boson is introduced. This couples to massive particles and gives them mass.

All the particles in the Standard Model have already been observed, most probably also the Higgs boson. An intensive search for the Higgs boson is being carried out at the LHC and in ATLAS. As announced on the 4th of July 2012 during the CERN seminar "Latest update in the search for the Higgs boson"[16], both experiment ATLAS and CMS observed a new particle consistent with the Higgs boson with mass in the region between 125 and 126 GeV. These results are preliminary and based on data collected in 2011 ($\sim 4.9\,\text{fb}^{-1}$) and 2012 ($\sim 5.9\,\text{fb}^{-1}$). More data is needed to study the properties of the new particle and confirm or disprove the hypothesis that it is the Standard Model Higgs. The discovery of the Higgs boson would solve some of the unknown problems in the Standard Model, but it will not make it a fully complete theory of nature. Its 19 parameters are all free and their values cannot be obtained from theory. Moreover, the SM does not include gravity, does not explain the existence of exactly three generations of fermions and does not explain the matter-antimatter asymmetry in the universe.

1.2 Proton structure and parton distribution functions

The first detailed insight into the structure of the proton has been achieved by high energy lepton-nucleon scattering experiments known as Deep Inelastic Scattering (DIS) experiments such as the fixed target linear electron accelerator at the Stanford

Linear Accelerator Centre (SLAC) [17] and the *ep* collider Hadron Electron Ring Accelerator (HERA) [18] at the DESY laboratory in Hamburg.

The diagram in Figure 1.1 shows the DIS process where k and k' are the four-momenta of the incoming and outgoing leptons, P is the four-momentum of the nucleon of mass M, and M' is the mass of the recoiling system. The exchanged particle can be a photon, or a $W^{\pm}$ or Z boson which transfer the four-momentum $q = k - k'$ to the nucleon. The process is called deep because $Q^2 = -q^2$ is much larger than M^2 implying a large momentum transfer. Furthermore it is called inelastic because the mass M' is much larger than M.

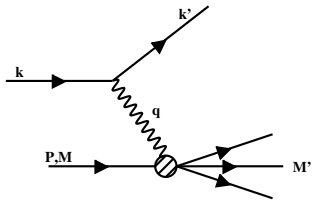

Figure 1.1: *Kinematic variables describing the DIS process.*

In 1968 the first DIS results from SLAC showed that for some fixed value of the variable $x = \frac{Q^2}{2P \cdot q}$ the cross section was independent of the scale of the interaction Q^2 in the range $1 < Q^2 < 10\,\mathrm{GeV}^2$ [19]. This behaviour was also predicted by Bjorken in 1969 and known as Bjorken scaling. In the same years Feynman developed an idea which would explain Bjorken scaling. It was assumed that the probe would scatter elastically off one of the point-like constituents of the proton called partons or quarks and therefore the cross section would be independent of the scale Q^2. The variable x was identified as the fraction of the proton's momentum carried by the struck parton, in a frame where the proton has infinite longitudinal momentum. This signified the beginning of the development of the Quark Parton Model (QPM). The concept of parton density functions (PDFs) $f_i(x)$ was introduced to express the probability for a parton i inside the proton to carry a fraction x of the proton's momentum. Nevertheless the QPM was not a complete theory. The most important problem was the contradiction of the inability of observing free quarks (confinement) in a model which assumed that the quarks were free (asymptotic freedom). Also, the momentum sum rule $\sum_i \int_0^1 x f_i(x) dx = 1$ was not satisfied by the measured PDFs. This gave a first hint of the existence of gluons to describe the quantum field of the strong interaction between quarks. The development of Quantum Chromodynamics (QCD) as the non-Abelian gauge theory of the strong interaction through the idea of a scale dependant coupling constant defined as:

$$\alpha_S(Q^2) = \frac{g^2(Q^2)}{4\pi}, \tag{1.1}$$

where g is the gauge field coupling, solved many of the open questions.

The strength of the coupling α_S increases for lower momentum transfer or equivalently for long distance interactions. As a consequence quarks and gluons are confined into hadrons. This property of QCD is called confinement. Conversely, for high Q^2 or short distance interactions, the strong coupling constant becomes weaker so that quarks and gluons are considered as free particles. This is called asymptotic freedom [20]. QCD was found to accommodate both of these features in a single theory. As already mentioned, in the QPM protons were thought to be made of partons, and these were thought to be only quarks. In the revisited version of the Parton Model protons are described as made of three valence quarks (two *up* type and one *down* type) and a so-called *sea* of virtual quarks and gluons. The three valence quarks determine the proton quantum numbers such as its charge. If probed at high momentum scales, a more detailed structure can be resolved, as valence quarks may radiate gluons. These can produce virtual quark-antiquark pairs ($q\bar{q}$) or gluon pairs. Virtual quarks are also called sea quarks and they can in turn radiate gluons. Valence quarks, sea quarks and gluons are jointly called *partons*.

In the region of phase space where the coupling α_S is small enough to allow cross section calculations to be performed as a convergent power series in the parameter α_S , perturbative QCD calculations (pQCD) are possible, whereas non perturbative QCD is referred to as the region where the coupling is large and perturbative calculations are not possible.

In general allowing for additional gluons to be emitted or exchanged by the interacting partons due to the strong interaction creates singularities and divergences in the cross section calculation. These are due to gluons emitted parallel to the incoming quarks (collinear divergences) or to very soft gluon emission (infrared divergences). QCD is a renormalisable theory in which collinear divergences are removed by fixing an arbitrary renormalisation scale (μ_R), usually the same for all divergent integrals, as in the modified minimal subtraction scheme ($\overline{\text{MS}}$) [21]. The scale dependence is absorbed in the coupling $\alpha_S(\mu_R)$ and for perturbative expansions summed to all orders its dependence vanishes. In the case of infrared singularities, these are absorbed into the PDFs and removed from the calculation. In this case a factorisation scale (μ_F) is arbitrary chosen.

This introduces the dependence of the parton densities on the scale as well as the already discussed x dependence, and therefore the PDF definition as a parton distribution function $f_{a/A}(x_a, Q^2)dx_a$, which more generally expresses the probability

for a parton a inside hadron A, probed at scale Q^2, to carry a fraction of momentum between x_a and $x_a + dx_a$. There are 13 PDFs, one for each quark, one for each antiquark and one for the gluon.

The redefined PDFs are not calculable using perturbative techniques; at fixed scale they can be parameterised using experimental data to measure the x dependence (but of course not the scale dependence). The starting value at which the PDFs are extracted must be large in order to ensure that the value of the coupling α_S is small enough for perturbative calculations to be performed. The parameters (such as the analytic form of the PDFs at the starting scale and the value of α_S) are determined using a χ^2 fit.

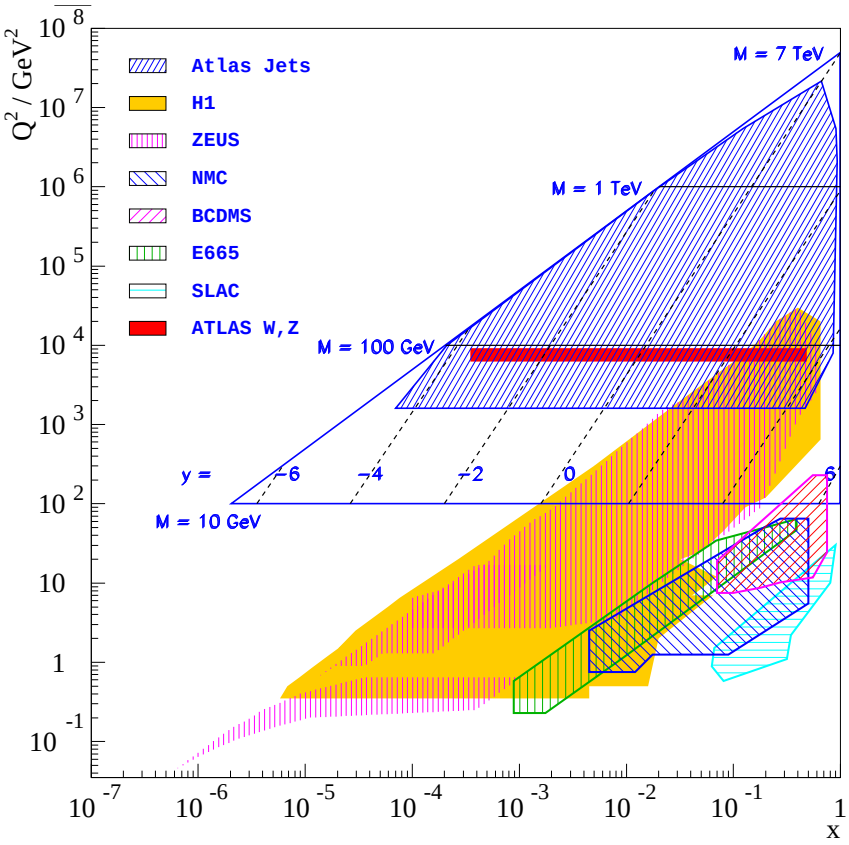

Figure 1.2: *Kinematic coverage of ATLAS and other experiments [1].*

The knowledge of PDFs is an essential input to precision measurements of the Standard Model at the LHC and allows the calculation of the cross section of any proton scattering process. The uncertainties on the PDFs are larger at low x (below about $x = 10^{-4}$) and at high x (above about $x = 0.5$). This is due to the limited amount of data available at these extreme regions of phase space, where the best current constraints come from the HERA experiments.

The kinematic range of partons in ATLAS as a function of x and Q^2 is presented in Figure 1.2 where a comparison to the kinematic reach of other experiments is also shown.

Although the PDFs are not calculable, their evolution with scale is. This is done using the Dokshitzer-Gribov-Lipatov-Altarelli-Parisi (DGLAP) QCD evolution equations [22, 23, 24, 25].

The DGLAP equations are a matrix equation of dimension $(2n_f + 1)$ where n_f is the number of quark and antiquark flavour which contribute. The equation can be expressed as:

$$\begin{aligned}\frac{\partial}{\partial \ln \mu_F^2}\begin{pmatrix} q_i(x,\mu_F^2) \\ g(x,\mu_F^2)\end{pmatrix} &= \frac{\alpha_S(\mu_F^2)}{2\pi}\sum_{q_i,\bar{q}_j}\int_x^1 \frac{dz}{z} \\ &\times \begin{pmatrix} P_{q_iq_j}\left(\frac{x}{z},\alpha_S(\mu_F^2)\right) & P_{q_ig}\left(\frac{x}{z},\alpha_S(\mu_F^2)\right) \\ P_{gq_j}\left(\frac{x}{z},\alpha_S(\mu_F^2)\right) & P_{gg}\left(\frac{x}{z},\alpha_S(\mu_F^2)\right)\end{pmatrix}\begin{pmatrix} q_j(z,\mu_F^2) \\ g(z,\mu_F^2)\end{pmatrix},\end{aligned} \tag{1.2}$$

where μ_F^2 is the factorisation scale and $q_i(x,\mu_F^2)$ and $g(x,\mu_F^2)$ are the quark and gluons PDFs respectively. Each equation gives a description of how the quark (antiquark, gluon) density changes as a function of $\ln \mu_F^2$ [26]. The splitting functions can be calculated as a power series of α_S such that:

$$\begin{aligned} P_{q_iq_j}(t,\alpha_S) &= \delta_{ij}P_{qq}^{(0)}(t) + \frac{\alpha_S}{\pi}P_{q_iq_j}^{(1)}(t) + ... \\ P_{qg}(t,\alpha_S) &= P_{qg}^{(0)}(t) + \frac{\alpha_S}{\pi}P_{qg}^{(1)}(t) + ... \\ P_{gq}(t,\alpha_S) &= P_{gq}^{(0)}(t) + \frac{\alpha_S}{\pi}P_{gq}^{(1)}(t) + ... \\ P_{gg}(t,\alpha_S) &= P_{gg}^{(0)}(t) + \frac{\alpha_S}{\pi}P_{gg}^{(1)}(t) + ... \ . \end{aligned} \tag{1.3}$$

To leading order (LO) the splitting functions are given by:

$$
\begin{aligned}
P_{qq}^{(0)}(t) &= C_F \left[\frac{1+t^2}{(1-t)_+} + \frac{3}{2}\delta(1-t) \right], \;\; C_F = \frac{4}{3}, \\
P_{qg}^{(0)}(t) &= T_R \left[t^2 + (1-t)^2 \right], \;\; T_R = \frac{1}{2}, \\
P_{gq}^{(0)}(t) &= C_F \left[\frac{1+(1-t)^2}{t} \right], \\
P_{gg}^{(0)}(t) &= 2C_A \left[\frac{t}{(1-t)_+} + \frac{1-t}{t} + t(1-t) \right], \\
&\quad + \delta(1-t) \frac{(11C_A - 4N_f T_R)}{6}, \;\; C_A = 3, N_f = 3,
\end{aligned} \tag{1.4}
$$

where the + sign as a subscripts on the singular parts of the functions denotes that:

$$
\begin{aligned}
\frac{1}{(1-t)_+} &= \frac{1}{(1-t)} \text{ for } 0 \leq t < 1, \\
\int_0^1 ds \frac{f(t)}{1-t}_+ &= \int_0^1 ds \frac{f(t) - f(1)}{1-t}.
\end{aligned} \tag{1.5}
$$

The next-to-leading-order (NLO) and next-to-next-to-leading order (NNLO) splitting functions have also been calculated [27, 28].

1.3 Total cross section in hadron collisions

The cross section of an interaction is a measure of the likelihood of a specific process to occur and is quantified as an effective area, σ.

Given two fermions c and d and any particle or multiple particle X, the factorisation theorem [29] states that the hadronic leading order total cross section σ_{LO} for the process $AB \to cd + X$ (see Figure 1.3) where hadrons A and B interact to produce the final state $cd + X$ can be obtained by weighting the cross section $\hat{\sigma}_{ab}$ for the process $ab \to cd + X$ with the parton distribution functions $f_{a/A}(x_a, Q^2)$ and $f_{b/B}(x_b, Q^2)$ [30]. The first contribution refers to the interaction between two partons, whereas the second describes the distribution of partons inside the hadron. At LO the parton model does not include any QCD corrections and the total LO cross section can therefore be expressed as:

$$
\sigma_{LO} = \sum_{a,b} C_{ab} \int dx_a \, dx_b \left[f_{a/A}(x_a, Q^2) \, f_{b/B}(x_b, Q^2) + (A \Leftrightarrow B)|_{a \neq b} \right] \times \hat{\sigma}_{ab}, \tag{1.6}
$$

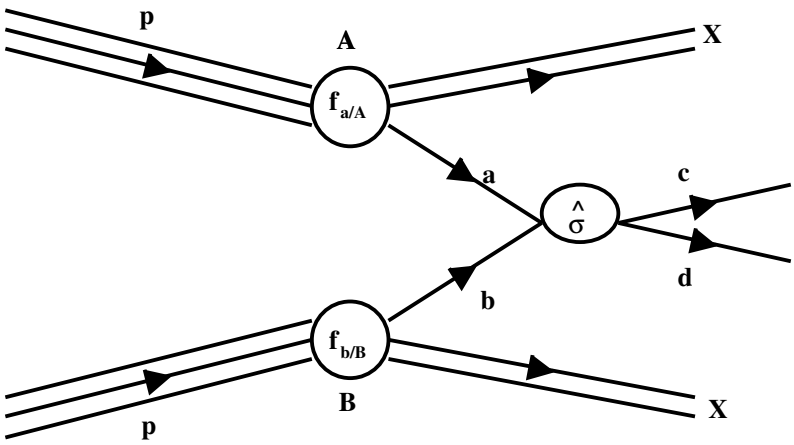

Figure 1.3: *Diagram showing a proton-proton collision, and subprocess interaction between partons a and b with final state fermions c and d.*

where $(A \Leftrightarrow B)|_{a \neq b} = f_{a/B}(x_b, Q^2)\, f_{b/A}(x_a, Q^2)$ accounts for the possibility of parton a coming from hadron B and carrying a momentum fraction x_b and parton b coming from hadron A and carrying a momentum fraction x_a. In Equation 1.6 the term C_{ab} is the initial colour averaging factor [1].

The four momentum of each hadron is correlated to the one of each interacting parton through the momentum fractions x_a and x_b such that $p_a = x_a p_A$ and $p_b = x_b p_B$, where the parton masses are negligible with respect to their momentum. Therefore, assuming the hadrons in the centre of mass frame with no relative angle between the interacting partons, the invariant mass squared of the parton pair is related to the Bjorken x_a and x_b by:

$$Q^2 = (p_a + p_b)^2 = x_a x_b s, \tag{1.7}$$

where s is the invariant mass squared of the hadron pair. By defining a new variable $\tau = x_a x_b = Q^2/s$, Equation 1.6 can be written as a function of τ and x_a as:

$$\sigma_{LO} = \sum_{a,b} C_{ab} \int_0^1 d\tau \int_\tau^1 \frac{dx_a}{x_a} [f_{a/A}(x_a, Q^2)\, f_{b/B}(\frac{\tau}{x_a}, Q^2) + (A \Leftrightarrow B)|_{a \neq b}] \times \hat{\sigma}_{ab}\,, \tag{1.8}$$

and the differential cross section with respect to τ is therefore:

[1] For quarks and gluons the value of C_{ab} is $C_{q\bar{q}} = \frac{1}{9}$, $C_{qg} = \frac{1}{24}$ and $C_{gg} = \frac{1}{64}$ since there are three different colour charges carried by each quark and eight by each gluon.

$$\left.\frac{d\sigma}{d\tau}\right|_{LO} = \sum_{a,b} C_{ab} \int_{\tau}^{1} \frac{dx_a}{x_a} [f_{a/A}(x_a, Q^2)\, f_{b/B}(\frac{\tau}{x_a}, Q^2) + (A \Leftrightarrow B)|_{a\neq b}] \times \hat{\sigma}_{ab}\,. \quad (1.9)$$

In hadron collisions, it is often convenient to use the rapidity Y for differential cross section calculations rather than $x_a x_b$, since the parton's centre of mass moves in the lab frame along the beam axis, and therefore the cross sections are not invariant under a boost. The rapidity is defined as:

$$Y = \frac{1}{2} \ln \left(\frac{E + p_L}{E - p_L} \right) = \frac{1}{2} \ln \frac{x_a}{x_b}, \quad (1.10)$$

where p_L is the momentum component of the ab system (in the AB centre of mass frame) along the longitudinal direction and E its energy. Under the class of Lorentz transformations corresponding to a boost in the longitudinal direction, the rapidity transforms additively. Therefore rapidity differences are boost invariant.

In Equation 1.10 the rapidity is also expressed as a function of the momentum fractions x_a and x_b. From this the Bjorken x of the two partons can be expressed in terms of τ and y as:

$$x_a = \sqrt{\tau} e^{Y} = \frac{Q}{\sqrt{s}} e^{Y}, \qquad x_b = \sqrt{\tau} e^{-Y} = \frac{Q}{\sqrt{s}} e^{-Y}\,. \quad (1.11)$$

The double differential cross section in Y and τ can be written as:

$$\left.\frac{d^2\sigma}{d\tau dY}\right|_{LO} = \left.\frac{d^2\sigma}{dx_a dx_b}\right|_{LO} = \sum_{a,b} C_{ab} [f_{a/A}(x_a, Q^2)\, f_{b/B}(\frac{\tau}{x_a}, Q^2) + (A \Leftrightarrow B)|_{a\neq b}] \times \hat{\sigma}_{ab}\,, \quad (1.12)$$

or in terms of $x = x_a - x_b$ (also called the Feynman x) and τ as:

$$\left.\frac{d^2\sigma}{d\tau dY}\right|_{LO} = \sqrt{x^2 + 4\tau} \left.\frac{d^2\sigma}{d\tau dx}\right|_{LO}. \quad (1.13)$$

The QCD improved version of the total cross section given in Equation 1.6 can be expressed as:

$$\begin{aligned} \sigma &= \sum_{a,b} C_{ab} \int dx_a\, dx_b\, [f_{a/A}(x_a, Q^2)\, f_{b/B}(x_b, Q^2) + (A \Leftrightarrow B)|_{a\neq b}] \\ &\times \left[\hat{\sigma}_0 + \frac{\alpha_S(Q^2)}{2\pi} \hat{\sigma}_1 + \left(\frac{\alpha_S(Q^2)}{2\pi} \right)^2 \hat{\sigma}_2 + ... \right], \end{aligned} \quad (1.14)$$

where the power of α_S is equal to the number of gluon emissions allowed in the

process.

1.4 The Drell-Yan process

In hadron-hadron collisions, the Drell-Yan process consists of the production of leptons by quark-antiquark annihilation to produce a virtual photon, or a Z, which decays to the lepton pair, $q\bar{q} \to Z/\gamma^* \to l^+l^-$. In this thesis the low mass di-muon channel is studied. A schematic diagram of a proton-proton collision is shown in Figure 1.4 in the specific case of the Drell-Yan process with muons in the final state.

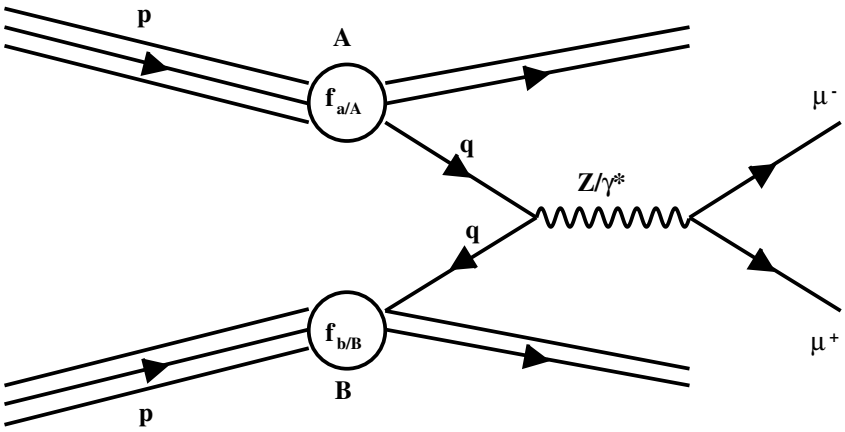

Figure 1.4: *Schematic diagram of a proton-proton collision including the tree level Feynman diagram of the Drell-Yan process.*

The total cross section for the Drell-Yan process at LO can be expressed in the parton model described in the previous section and is given by:

$$\sigma_{LO} = \sum_q \int dx_1\, dx_2\, [f_{q/A}(x_1, M_{ll}^2)\, f_{\bar{q}/B}(x_2, M_{ll}^2) + (q \Leftrightarrow \bar{q})] \times \hat{\sigma}_{q\bar{q}\to l^+l^-}, \qquad (1.15)$$

where M_{ll} is the invariant mass of the lepton pair and $\hat{\sigma}_{q\bar{q}\to l^+l^-}$ represents the subprocess cross section given by the annihilation process $q\bar{q} \to Z/\gamma^* \to l^+l^-$. Starting from the $e^+e^- \to q\bar{q}$ LO cross section:

$$\sigma_0 = \frac{4\pi\alpha^2}{3Q^2} C_q^2\,, \qquad (1.16)$$

the leading order subprocess for Drell-Yan cross section is given by

$$\hat{\sigma}(q(p_1)\bar{q}(p_2) \to l^+l^-) = \frac{4\pi\alpha^2}{3Q^2}\frac{1}{N}C_q^2, \tag{1.17}$$

where α is the EM coupling, p_1 and p_2 are the four-momenta of the quark and antiquark respectively, $Q^2 = (p_1 + p_2)^2 = M_{ll}^2$, C_q is the quark electric charge, and $\frac{1}{N} = \frac{1}{3}$ accounts for the fact that of nine colour combinations for quark and antiquark pair, only three give a colourless virtual photon. The subprocess differential cross section for the production of a lepton pair with mass M_{ll} is:

$$\frac{d\hat{\sigma}}{dM_{ll}^2} = \frac{4\pi\alpha^2}{3M_{ll}^2}\frac{1}{N}C_q^2\delta(Q^2 - M_{ll}^2), \tag{1.18}$$

and the total parton model cross section for the Drell-Yan process, differential in M_{ll}^2 is therefore:

$$\begin{aligned}\left.\frac{d\sigma}{dM_{ll}^2}\right|_{LO} &= \int_0^1 dx_1\, dx_2 \sum_q [f_{q/A}(x_1, M_{ll}^2)\, f_{\bar{q}/B}(x_2, M_{ll}^2) + (q \Leftrightarrow \bar{q})] \times \frac{d\hat{\sigma}}{dM_{ll}^2}(q\bar{q} \to l^+l^-) \\ &= \frac{4\pi\alpha^2}{3M_{ll}^2}\frac{1}{N}\int_0^1 dx_1\, dx_2\, \delta(x_1x_2s - M_{ll}^2) \\ &\times [\sum_q C_q^2 f_{q/A}(x_1, M_{ll}^2)\, f_{\bar{q}/B}(x_2, M_{ll}^2) + (q \Leftrightarrow \bar{q})],\end{aligned} \tag{1.19}$$

or, in terms of $\tau = x_1x_2 = \frac{Q^2}{s}$, and differentially in M_{ll}:

$$\left.\frac{d\sigma}{dM_{ll}}\right|_{LO} = \frac{8\pi\alpha^2}{3M_{ll}^3}\frac{1}{N}\tau \int_0^1 dx_1\, dx_2\, \delta(x_1x_2 - \tau) \times [\sum_q C_q^2 f_{q/A}(x_1, M_{ll}^2)\, f_{\bar{q}/B}(x_2, M_{ll}^2) + (q \Leftrightarrow \bar{q})]\,. \tag{1.20}$$

Note the strong dependence of the differential cross section $\frac{d\sigma}{dM_{ll}}$ to the inverse of the cube of the di-lepton mass $\frac{1}{M_{ll}^3}$.

Analogous to Equation 1.12, for the Drell-Yan process the double differential cross section in terms of τ and Y can be written as:

$$\left.\frac{d^2\sigma}{dM_{ll}dY}\right|_{LO} = \frac{8\pi\alpha^2}{3M_{ll}^3}\frac{1}{N}\tau \times [\sum_q C_q^2 f_{q/A}(\sqrt{\tau}e^Y, M_{ll}^2)\, f_{\bar{q}/B}(\sqrt{\tau}e^{-Y}, M_{ll}^2) + (q \Leftrightarrow \bar{q})]\,. \tag{1.21}$$

This equation shows how it is possible in principle to measure the PDFs $f_{a/A}(\sqrt{\tau}e^Y, M_{ll}^2)$ and $f_{b/B}(\sqrt{\tau}e^{-Y}, M_{ll}^2)$ by measuring the distribution of rapidity and mass of the di-lepton system.

All of the above expressions for the cross section do not include the contribution from the Z boson resonance at $M_{ll} \sim M_Z$. At such high energies the s-channel Z exchange becomes relevant. In practice to include this, the electric charge C_q^2 is replaced by three terms such that:

$$C_q^2 \;\rightarrow\; C_q^2 - 2C_q V_l V_q \chi_1(s) + (A_l^2 + V_l^2)(A_q^2 + V_q^2)\chi_2(s)), \tag{1.22}$$

where the two extra terms account for the photon-Z interference (second term) and the Z exchange (third term) and where:

$$\chi_1(s) = k\frac{s(s - M_Z^2)}{(s - M_Z^2)^2 + \Gamma_Z^2 M_Z^2}\,,$$

$$\chi_2(s) = k^2\frac{s^2}{(s - M_Z^2)^2 + \Gamma_Z^2 M_Z^2}\,,$$

$$k = \frac{\sqrt{2}G_F M_Z^2}{16\pi\alpha}\,. \tag{1.23}$$

In the above equations G_F is the Fermi constant and Γ_Z is the total decay width of the Z boson. Γ_Z has been determined experimentally. The vector and axial coupling of the fermions to the Z bosons (V_f and A_f respectively) are correlated so that:

$$V_f = A_f - 2C_f \sin^2(\theta_W) \quad (\theta_W \text{ is the Weinberg angle})\,,$$

$$A_f = +1/2 \quad \text{for } f = u, \nu, ... \text{ and } A_f = -1/2 \quad \text{for } f = d, e, ... \tag{1.24}$$

Note how the three terms in Equation 1.22 simplify to C_q^2 for scattering energies far below the Z resonance peak, since the ratio s/M_Z^2 becomes small and the χ_1 and χ_2 terms are negligible. Instead, at the Z pole where $\sqrt{s} = M_Z$, the χ_2 term dominates and gives rise to a resonance peak. In this case the cross section given in Equation 1.16 becomes:

$$\sigma_0 = \frac{4\pi\alpha^2 k^2}{3\Gamma_Z^2}(A_l^2 + V_l^2)(A_q^2 + V_q^2)\,, \tag{1.25}$$

Figure 1.5 [11] shows the different contributions to the total differential cross section with respect to the di-lepton mass calculated at NNLO.

The measurement of the Drell-Yan cross section in the low mass region of the phase space is of particular interest as it allows the separation between u type and d type quarks to be made. As already presented above, at low masses the cross section is dominated by the large electromagnetic (EM) coupling, while at high

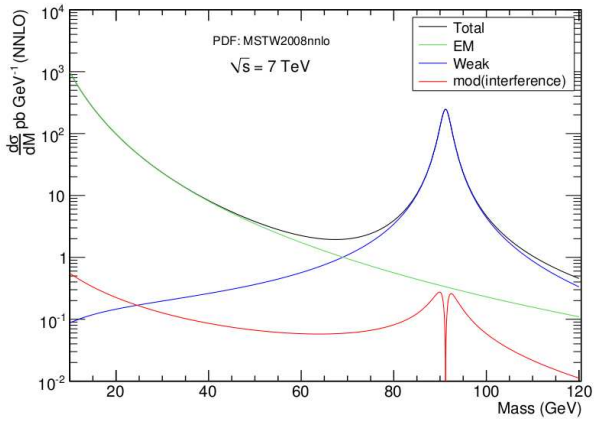

Figure 1.5: *NNLO contributions to the total Drell-Yan differential cross section with respect to the di-lepton pair.*

masses ($M_{ll} \sim M_Z$) the electroweak (EW) couplings dominate. Ignoring the small contribution of heavy quarks, in the two limits (EM and EW) the cross section can be approximated to:

$$\begin{aligned} \sigma_Z &\simeq (V_u^2 + A_u^2) \times u(x_1)\bar{u}(x_2) + (V_d^2 + A_d^2) \times d(x_1)\bar{d}(x_2) + [1 \leftrightarrow 2], \\ \sigma_{\gamma^*} &\simeq \frac{4}{9} \times u(x_1)\bar{u}(x_2) + \frac{1}{9} \times d(x_1)\bar{d}(x_2) + [1 \leftrightarrow 2], \end{aligned} \tag{1.26}$$

where $(V_u^2 + A_u^2) \simeq 0.29$ and $(V_d^2 + A_d^2) \simeq 0.37$. In the EM limit, the differential cross section at LO in Equation 1.21 can therefore be expressed as:

$$\left.\frac{d\sigma}{dM_{ll}dY}\right|_{LO} = \frac{8\pi\alpha^2}{3M_{ll}^3}\frac{1}{N}\tau \times [\frac{4}{9} \times U(x_1)\bar{U}(x_2) + \frac{1}{9} \times D(x_1)\bar{D}(x_2) + (1 \Leftrightarrow 2)], \tag{1.27}$$

where U ($\bar{U}$) and D ($\bar{D}$) are the sum of up-type and down-type quarks (antiquarks) respectively.

1.4.1 High order correction to the Drell-Yan process

The source of higher order QCD corrections to the Drell-Yan cross section is the interaction with gluons. In Figure 1.6 the NLO diagrams for the Drell-Yan process are shown. There are three different types of contributions: virtual gluon corrections to the initial state shown in Figure 1.6 (a) and (b), real gluon emission producing a gluon in the final state along with the Drell-Yan lepton pair as in Figure 1.6 (c), and the quark (antiquark) - gluon scattering process with an additional parton in

the final state as shown in Figure 1.6 (d) and (e).

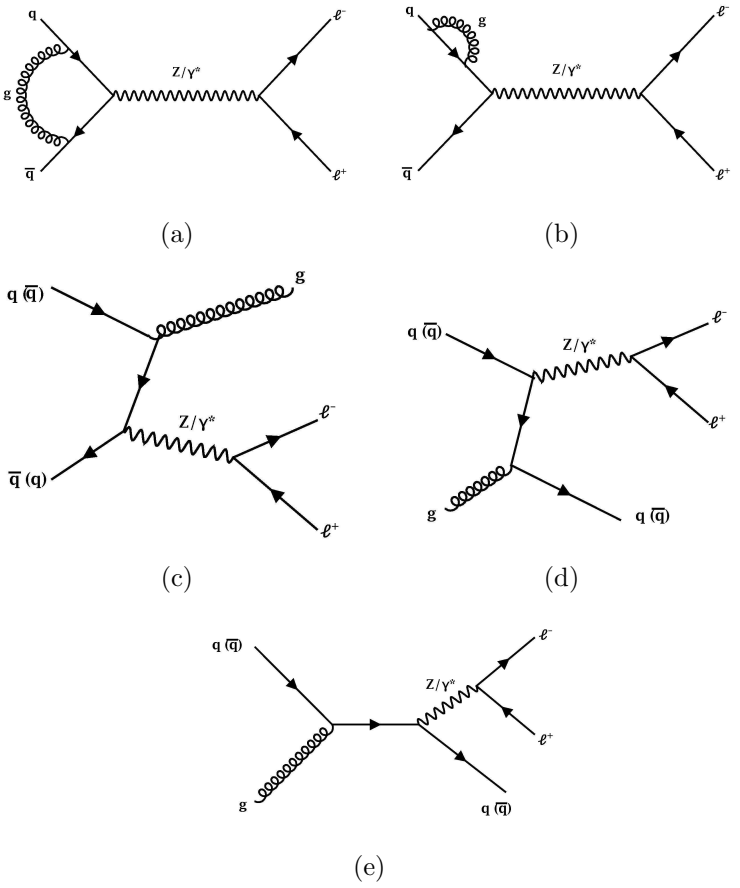

Figure 1.6: *Next to leading order contributions to the Drell-Yan process.*

The real and virtual gluon emission gives the infrared divergences, while the collinear divergences originate from the initial state partons splitting ($q \to qg$, and $g \to q\bar{q}$). The NNLO contributions to the Drell-Yan cross section come from higher order processes such as $qq \to qql^+l^-$ and $gg \to q\bar{q}l^+l^-$. The NNLO Drell-Yan cross sections has been calculated here [31].

The measure of the NLO and NNLO corrections depends on the collision energy and on the mass of the di-lepton pair. For pp collisions at $\sqrt{s} = 7\,\text{TeV}$ they can increase the LO cross section by about 30% as it will be shown in Section 5.

Often the knowledge of the NLO and NNLO cross section is used to correct LO Drell-Yan simulated event samples (MC) such as Pythia. This is done by calculating correction factors also known as k-factors as a function of the collision centre of mass energy, PDFs, mass and rapidity of the di-lepton pair, such that:

$$\sigma_{NLO} = k_{NLO}(\sqrt{s}, PDFset, M_{ll}, Y_{ll})\sigma_{LO}\,, \tag{1.28}$$

and similarly for the NNLO case.

VRAP [32] is a program used to calculate analytically such k-factors. In Section 5 the NLO and NNLO k-factors are calculated using VRAP and used to correct the LO and NLO Drell-Yan MC samples to NNLO, in order to have a better description and compare to collision data.

Chapter 2

Detector introduction and overview

ATLAS is a general purpose detector at the Large Hadron Collider (LHC) at CERN. Given the high energy achievable in the head-on collisions of protons at the LHC, the ATLAS detector is able to test the large variety of physics phenomena predicted at the TeV scale. It will also be able to explore and possibly make us understand present unknowns such as the origin of mass, the form of dark matter in the universe, the existence of super-symmetric particles, the presence of extra dimensions of space, and quantum gravity.

Although the LHC physics program is mainly based on proton-proton collisions, shorter running periods are dedicated to heavy-ion collisions, typically for about one month at the end of each calendar year. The aim of the heavy-ion program is to investigate the early universe existence of a quark-gluon plasma, and to study how it evolves into the matter that makes the universe today.

In this chapter, an overview of the LHC accelerator is given, as well as a description of the ATLAS detector and its subsystems.

2.1 The Large Hadron Collider

The Large Hadron Collider is a proton synchrotron with a circumference of 26.7 km, situated in a tunnel about 100 m underground at the border between France and Switzerland. It is the highest energy particle accelerator ever built and it is managed by CERN (European Council of Nuclear Research). The LHC is designed to collide protons at a maximum centre of mass energy of 14 TeV. After the protons are extracted by ionising hydrogen atoms, they are accelerated to an energy of 50 MeV in the linear accelerator (LINAC 2). Once this energy is achieved, the protons are injected in the Proton Synchrotron Booster (PSB) where they undergo further acceleration up to 1.4 GeV. Before entering the LHC beam pipe the protons are accelerated further by the Proton Synchrotron (PS) up to 26 GeV. Here the bunching structure is applied using 40 MHz RF cavities. The resulting minimum bunch spacing is 25 ns. The bunches enter the Super Proton Synchrotron (SPS). The SPS accelerates protons up to 450 GeV and then injects them into the LHC, where superconducting magnets bend and focus the proton bunches. Here the last step of the acceleration takes place, up to a maximum of 7 TeV of energy. Table 2.1 summaries the main LHC parameters.

Parameter	Value
Circumference	26659 m
Dipole operating temperature	1.9 K
Number of dipole magnets	1232
Number of quadrupole magnets	858
Number of RF cavities	eight per beam
Bunch spacing	25 ns (or multiples thereof)
Peak dipole magnetic field at 7 TeV	8.33 T
Design Luminosity	$10^{34}\,\mathrm{cm}^{-2}\,\mathrm{s}^{-1}$
Energy per beam, protons	7 TeV (design)
	3.5 TeV (2010-2011 operation)
	4 TeV (2012 operation)
Bunch crossing frequency	40 MHz
Number of bunches per proton beam (max.)	2808
Number of protons per bunch	1.15×10^{11} (25 ns) or 1.6×10^{11} (50 ns)
Number of collisions per second	600 millions
Total crossing angle (at the interaction point)	300 μrad

Table 2.1: *Main LHC parameters.*

Around the LHC tunnel there are four interaction points where the proton bunches are made to collide, and where four detectors have been built. These are namely ATLAS [33], ALICE [34], CMS [35] and LHCb [36]. Figure 2.1 shows the

LHC tunnel with the four experiments around it, and also shows a view of the other smaller accelerators listed above where the protons are initially accelerated before being injected into the LHC.

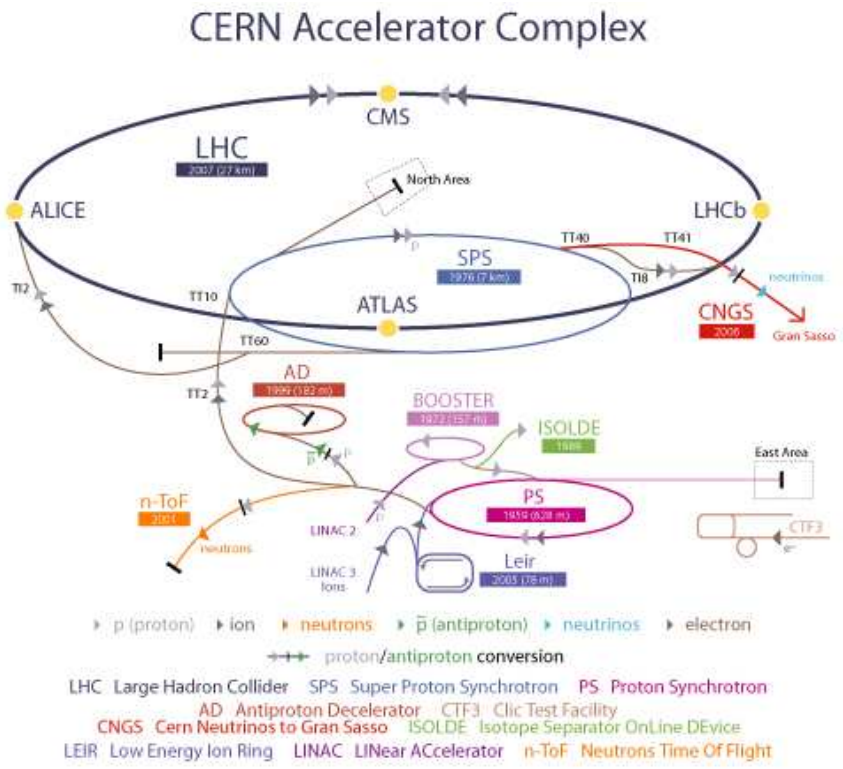

Figure 2.1: *Layout of the accelerator complex at CERN. ATLAS and the other three detectors built around the LHC are also shown [2].*

On the 30th of March 2010, the LHC started running at a centre-of-mass energy of 7 TeV. The LHC delivered a total of 48.1 pb^{-1} of integrated luminosity during the 2010 operation, and a total of 5.6 fb^{-1} during the 2011 operation. In 2012 the LHC has been operating at a centre-of-mass energy of 8 TeV, and $\sim$15 fb^{-1} of data were collected by October.

2.2 The ATLAS detector

ATLAS (A Toroidal LHC ApparatuS) is one of the four particle detectors built around the LHC. It is the largest of the four detectors, being about 45 m in length, more than 25 m high, and weighing about 7,000 tonnes. In order to identify the large variety of physics phenomena that are accessible at the TeV energy scale at the LHC, ATLAS has been designed such that it meets all the following requirements:

- Spatial position measured with high precision giving high granularity for track-finding;
- large coverage in pseudo-rapidity;
- full azimuthal coverage;
- good charged particle momentum resolution;
- good electron/photon identification in the electromagnetic calorimetry;
- high precision jet and missing transverse energy measurements in the hadronic calorimetry;
- good muon identification, including their charge and momentum resolution;
- efficient and robust data acquisition and trigger system.

ATLAS is comprised of four major components; these are shown in Figure 2.2. Starting from the beam line and proceeding outwards, in cylindrical layers around the beam axis we have:

- the inner tracker: measures the momentum of charged particles;
- the calorimeters: (electromagnetic and hadronic) measure the energy deposited by hadrons, electrons, muons and photons;
- the muon spectrometer: identifies and measures momentum and charge of muons.

The other component of ATLAS is the solenoidal and toroidal magnet system. This is designed to bend charged particles in order to measure their momentum. The solenoidal magnet surrounds the inner detector and produces a 2 T magnetic field. The toroidal magnet system is situated within the muon spectrometer. There are eight toroidal magnets in the Barrel producing a magnetic field of 3.9 T, and eight in each Endcap producing a magnetic field of 4.1 T. Each toroidal magnet is radially and symmetrically distributed around the beam axis.

The enormous amount of data delivered by each collision in ATLAS is handled by a trigger system and a data acquisition system (DAQ). The DAQ system records all the interesting events selected by the trigger system, for offline analysis.

ATLAS uses a right handed coordinate system. The x-axis points towards the centre of the LHC ring, the z-axis along the beam direction and the y-axis pointing upwards. Two angular coordinates are also defined. θ is the polar angle of the

particle's direction measured from the positive z-axis such that $0 \leq \theta \leq \pi$. ϕ is the azimuthal angle: it is zero along the positive x-axis and it ranges from -π to +π. The transverse momentum p_T is defined as the momentum of the particle in the plane perpendicular to the z-axis. Two more variables can be defined: the rapidity and pseudo-rapidity of a particle. The rapidity has already been introduced and defined in Section 1.3. The pseudo-rapidity is defined as:

$$\eta = -\ln\left(\tan\frac{\theta}{2}\right). \tag{2.1}$$

From this definition it can be seen that $\eta = 0$ for tracks which are orthogonal to the z-axis, $\eta = +\infty$ for tracks in the direction of the positive z-axis and $\eta =$ -∞ for tracks in the direction of the negative z-axis. The two variables η and Y coincide in case of massless particles ($m \to 0$). Experimentally η is a more convenient variable to use since the polar angle of a particle is measured directly in the detector. A useful separation distance often used is ΔR, relating the η and ϕ variables and defined as:

$$\Delta R = \sqrt{(\Delta\eta)^2 + (\Delta\phi)^2}. \tag{2.2}$$

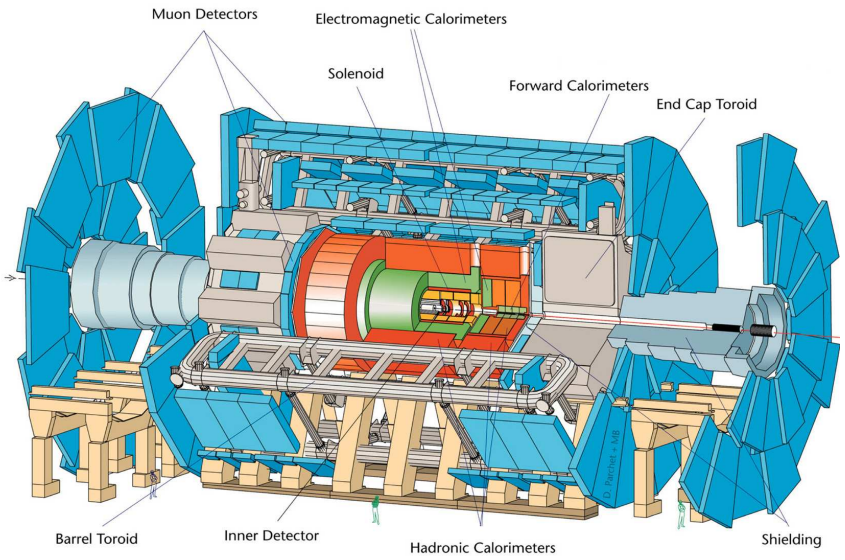

Figure 2.2: *Drawing showing the ATLAS detector and its subsystems [3].*

The following sections describe the main features of each subdetector including the trigger and DAQ systems.

2.2.1 Inner Detector

The Inner Detector (ID) is the closest subdetector of ATLAS to the interaction point (IP) and it covers a pseudo-rapidity range up to $|\eta| = 2.5$. There are three components which make up the ID; starting from the closest to the beam line these are: the silicon pixel detector, the Semiconductor Tracker (SCT) and the Transition Radiation Tracker (TRT). Each of these subsystems is described individually below. The ID is surrounded by a 2 T solenoid magnet; this supplies the magnetic field needed to measure the momentum of charged particles in this region of the detector. Figures 2.3 and 2.4 show the layout of the ID subsystems.

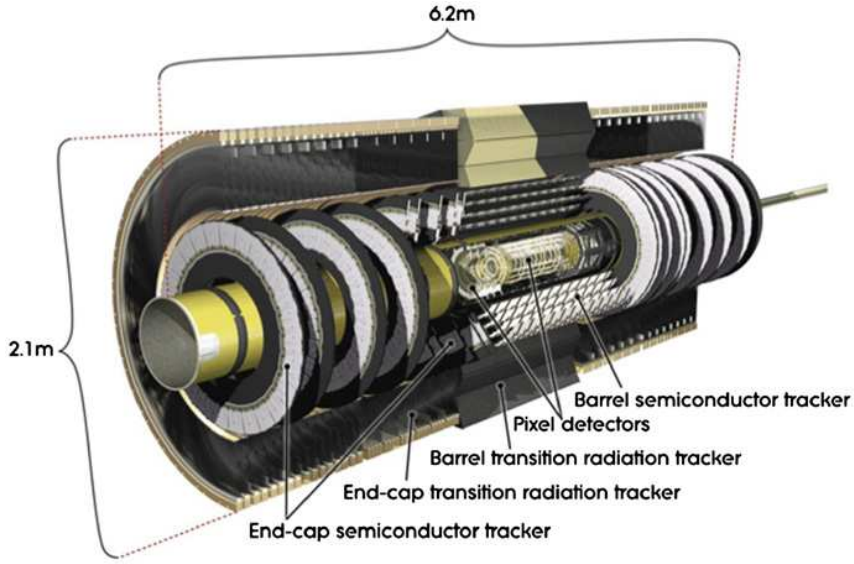

Figure 2.3: *Layout of the ATLAS inner detector. All subdetectors in the Barrel and Endcaps are shown [4].*

Pixel Detector

The Pixel detector is the inner-most subdetector and is made of three layers in the Barrel region, arranged concentrically around the beam pipe. The layer which is closest to the beam line is also referred to as the b-layer. In the Endcaps the detector is made of six flat disks perpendicular to the beam pipe, three on each end of the Barrel. The pixel detector gives an accurate measurement of the impact parameter, and is essential for vertex reconstruction in ATLAS. With a total of 80 million readout channels, most of which have dimensions 50 x 400 μm^2, the pixel detector covers an area of 1.7 m^2.

When a charged particle passes through the silicon it generates electron-hole

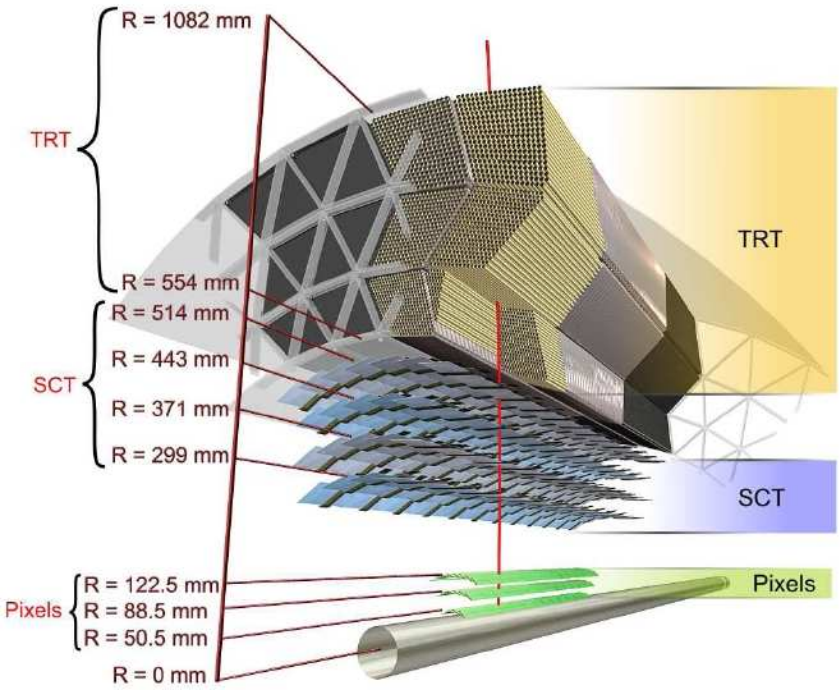

Figure 2.4: *Drawing showing all the different layers of the ID in the Barrel region of ATLAS [4].*

pairs. These then drift to each side of the silicon wafer due to an applied bias voltage. Each pixel is bump-bonded to a front-end chip (of which there are sixteen per module), where the sensor charge is amplified and compared to a programmable threshold. A typical track crosses all three layers of pixel detector giving at least three 3-D space point measurements with 10 μm resolution in r-ϕ (where r is the radial distance) in both Barrel and Endcap.

Due to the proximity to the beam line, the pixel detector is in a high radiation environment. In order to keep the noise level to a minimum, the pixel modules operate at low temperature, between -5 $^{\circ}C$ and -10 $^{\circ}C$.

Semiconductor Tracker

The Semiconductor Tracker (SCT) is the second subdetector from the interaction point preceded only by the pixel system. It consists of 4088 silicon crystal semiconductor modules, each of which is made of two wafers of silicon micro-strip detector glued back-to-back with a stereo angle of 40 mrad. Each wafer is read out by six readout chips, each of which reads out 128 strips, giving a total of 768 strips per wafer. The strips are 6.4 cm in length, with a separation of 80 μm and biased with a nominal voltage of 150 V.

The Barrel region has a pseudo-rapidity coverage in the range $|\eta| < 1.4$. Incident tracks cross all of the four concentric cylindrical layers of the detector. These are placed at radii of 20 cm, 37.3 cm, 44.7 cm and 52 cm, and contain 32, 40, 48 and 56 rows of modules respectively, giving a total of 2112 Barrel modules, on which the strips are designed to run approximately parallel to the beam line. An image of a Barrel module is shown in Figure 2.5.

In each Endcap the SCT is made of nine disks, for a total of 988 modules per Endcap and a pseudo-rapidity coverage that does not extend above about $|\eta| = 2.5$. Each track crosses at least four disks in this region. In the Endcap modules the strips run radially to the beam line.

The 40 mrad stereo angle facilitates measurements of the z-coordinate by allowing a combination of hits on both sides of a module, and similarly, the r-coordinate can be measured in the Endcaps. The resolution of the $r - \phi$ co-ordinate in the Barrel and $z - \phi$ co-ordinate in the Endcaps is around 17 μm, while the r and z are measured in the Barrel and Endcaps respectively with a resolution of about 580 μm. Chapter 3 describes in more detail the SCT modules and the measurement of the Lorentz angle in the Barrel region.

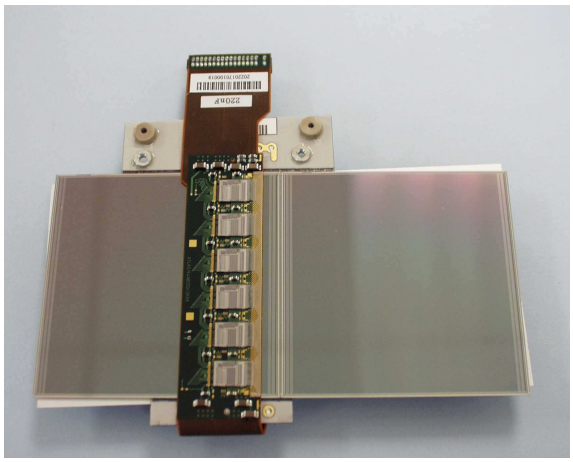

Figure 2.5: *Picture of a SCT Barrel module [5].*

Transition Radiation Tracker

The outermost ID subsystem is a gas tube tracker called the Transition Radiation Tracker (TRT). It operates at room temperature and it extends radially from 554 mm to 1082 mm. This is made of 4 mm diameter straw tubes with a 30 μm W-Re wire passing through the centre. The applied voltage between the wire and the straw wall is about 1.6 kV.

Each tube contains a mixture of Xe (70%), CO_2 (27%) and O_2 (3%). Xenon gas is used in order to facilitate particle identification. This makes the observation of transition radiation photons easier given that there is a direct proportionality between the probability to radiate and the Lorentz factor ($\gamma = E/m$) of the particle and this is extremely useful to identify electrons with their low rest mass compared to other charged particles. Therefore the TRT is capable of identifying electrons over a large range of energies. The other two gaseous components in the straws are used both to increase the drift velocity of the electrons in the gas and to stabilise the mixture in the high electric field.

Overall the TRT system covers the pseudo-rapidity range up to $|\eta| = 2.0$. In the Barrel region there are 50,000 straws. These are 144 cm in length and run parallel to the beam line while in each Endcap there are 160,000 straws, each 37 cm in length. These run radially to the beam line. In the Barrel region the TRT is only capable of measuring in $r - \phi$ with an accuracy of 130 μm per straw. On average it provides, for each track, about 34 space points to the track fitting. In the Barrel the straws are divided at $z = 0$ and read out at each end, while in the Endcaps they are read out only at their outer end.

2.2.2 Calorimetry

The next layers of ATLAS outside the ID are the electromagnetic and hadronic calorimeters. These are used to measure the energies of electrons, photons, and jets with high precision. They also provide a measurement of the missing transverse energy (E_T^{miss}).

The electromagnetically interacting particles such as photons and electrons are absorbed by the electromagnetic calorimeter, while the hadronic calorimeter is responsible for the absorption of essentially all remaining strongly interacting particles. Of all the known Standard Model particles, only muons and neutrinos are expected to pass all the way through the calorimeters.

The ways in which the two subdetectors operate are similar. The interaction of the incident particle with the absorber material (lead, copper and tungsten) produces a shower of particles. These are then detected using two different methods in the active material. The first method of detection is based on the presence of liquid argon in a high electric field, which produces cascades of electrons detected as charge and electrically read out. The second method, the tile calorimeters, use a scintillating plastic. This generates photons detected via photomultiplier tubes. The overall coverage of the calorimetry system is $|\eta| < 4.9$.

Liquid Argon Electromagnetic Calorimeter

The electromagnetic calorimeter (ECAL) measures the energy and position of electrons and photons. The Barrel region coverage extends up to $|\eta| < 1.475$ while the Endcap regions have a coverage in the range $1.375 < |\eta| < 3.2$.

The ECAL is made of alternating layers of liquid argon (the active material) and lead (the absorber) in such a way as to minimise gaps between detector modules. Liquid argon is used as active material because of its intrinsic radiation hardness and also because it has a linear behaviour with respect to the energy of the incident particle. Showers are originated in the lead plates by electrons and photons. The shower particles then ionise the liquid argon. The amount of ionisation is proportional to the energy of the incident particle. Finally the signal is collected by the copper/kapton readout electrodes.

Given the presence of the ID and the solenoid in front of the ECAL, electrons and photons lose some fraction of their energies even before entering the calorimeters. For this reason, in the region of $|\eta| < 1.8$, a presampler allows any corrections to be made for showers originated in the ID volume. The presampler is an active layer of liquid argon, 1.1 cm thick in the Barrel and 0.5 cm in the Endcaps.

The cells of the ECAL are designed to point directly toward the interaction point so that spatial measurements can be translated directly into η and ϕ.

Hadronic Calorimeter

The hadronic calorimeter (HCAL) measures showers created by hadronic jets, usually initiated already in the ECAL, but that deposit the majority of their energy in this second detector system.

In the HCAL liquid argon is used as an active medium, but also a scintillator tile base detector is implemented. For $|\eta| < 1.7$ the hadronic calorimeter is made of an steel absorber with plastic tile scintillator plates used as an active medium. This is called the TileCal and it extends radially from 2.28 m out to 4.25 m.

Given the poor radiation hardness a different technology is used in the Endcap regions ($1.5 < |\eta| < 3.2$) where showers are detected using liquid argon as active medium and copper as passive shower material.

In the forward region ($3.1 < |\eta| < 4.9$), where no other detector is in place, sits the liquid argon forward calorimeter (FCal). It is made of three layers, the first one for electromagnetic measurement uses copper as absorber, whereas the second and third layers are made of tungsten and are used for hadronic measurements. In order to achieve high radiation hardness in this region, holes of 5 mm diameter are

formed in the copper or tungsten and rods of 4.5 mm in diameter are inserted leaving 250 μm gaps that are filled with liquid argon.

2.2.3 Muon Detector System

The Muon Spectrometer (MS) detects and measures the momentum of muons. The muon momentum measurement can be improved by matching tracks reconstructed in the ID with the measurement made in the muon system. However, it is possible to reconstruct "standalone" muons (with p_T ranging from about 4 GeV to about 3 TeV) using the MS information only.

Besides the superconducting toroidal magnets which are part of the muon system, the muon spectrometer is instrumented with high precision and trigger tracking chambers. The chamber system provides complete coverage in the η range $0 < |\eta| < 2.7$ except for $\eta = 0$ where there is a passage of cables and other services.

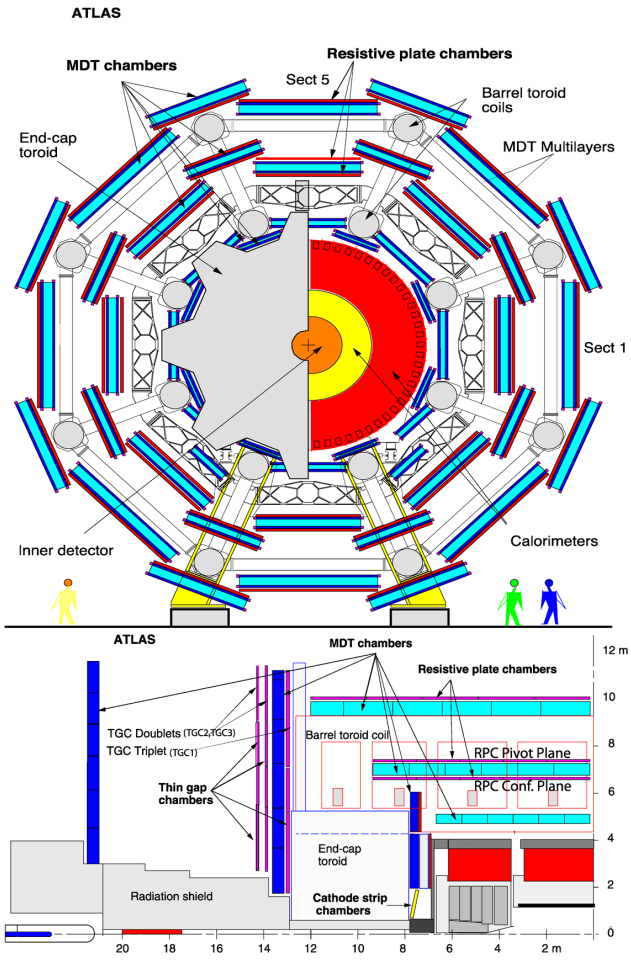

Figure 2.6: *Cross-section of the ATLAS Muon Spectrometer in the Barrel region (top) and overall across the full detector length (bottom) [6].*

In the Barrel, Monitored Drift Tubes (MDTs) and Resistive Plate Chambers (RPCs) are arranged in 16 ϕ sectors as shown in Figure 2.6. Each sector has three stations with increasing radius from the beam line and 12-fold segmentations in z. Each station consists of two MDT chambers for precision measurement and one or two RPC chambers for triggering. The Endcaps also have 16 ϕ sectors each arranged in three discs with increasing $|z|$ on each side of the detector. Each ϕ sector has up to six stations consisting of Thin Gap Chambers (TGCs) for triggering and MDTs for precision measurement. Cathode Strip Chambers (CSCs) are used for precision measurements at large pseudo-rapidities ($2 < |\eta| < 2.7$). Each subsystem introduced here is described in more details in the following sections.

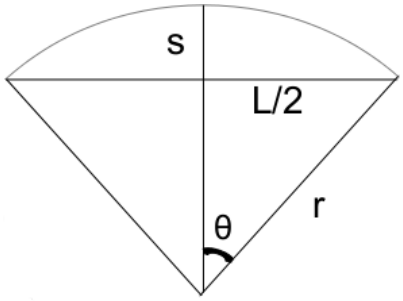

Figure 2.7: *Sagitta definition.*

The basic principle of momentum measurement in the muon spectrometer is the determination of the sagitta of a charged particle bent in the magnetic field. In the ideal case of an homogeneous magnetic field, muons, which are approximately perpendicular to the magnetic field, are bent in circles. Therefore the measurement of the radius of the circle allows a measurement of its momentum. From Figure 2.7 the radius r of a circle and its sagitta s are related to the angle θ by:

$$s = r\,(1 - \cos\theta)\,. \tag{2.3}$$

The sagitta is also related to the transverse momentum p_T of a particle, and the strength of the magnetic field B by:

$$s \simeq \frac{1}{8}\frac{L^2 B}{p_T}, \tag{2.4}$$

where L is the length of the muon trajectory. This relation shows how the measurement of a charged track transverse momentum is equivalent to the measurement of its sagitta. This measurement can be made by measuring three points along the trajectory of a muon.

Toroid magnet system

In the muon spectrometer, superconducting magnets provide magnetic bending of the muon tracks in order to measure their momentum. The magnets create a toroidal field surrounding the detector, so that particles are bent and the angle between the tracks and the beam line changes continuously. As a consequence, in the muon spectrometer the momentum resolution depends on precision measurement of z in the Barrel region and r in the Endcap regions. For $|\eta| < 1.0$ the toroidal field is given by eight Barrel toroids assembled radially and symmetrically around the beam axis. They provide a maximum field of 3.9 T. They are air-cooled superconducting magnets 26 m in length, and have an outer diameter of 20 m. In each Endcap ($1.4 < |\eta| < 2.7$) the tracks are bent by eight toroids, rotated by 22.5 degrees so that they fit at each end of the Barrel toroids. They are 5 m in length, the inner and outer diameters being 1.65 m and 10.7 m respectively. The peak field given by the Endcap toroids is 4.1 T. In the so-called transition region, over the η range $1.0 < |\eta| < 1.4$, the combination of the Barrel and Endcaps magnetic fields provide track deflection. The overall magnetic field is mostly perpendicular to the muon trajectories.

Precision measurement chambers

Monitored Drift Tubes (MDTs): The MDT component of the muon spectrometer is the main technology used for precision measurement. It covers the pseudorapidity range $|\eta| < 1.0$ in the Barrel and $1.0 < |\eta| < 2.7$ in the Endcaps, with exception for the innermost layer in the Endcaps where the coverage is restricted to $1.0 < |\eta| < 2.0$.

As the name also suggests, the chambers are made of six or eight layers of drift tubes arranged in two multi layers separated by 200 mm. Each aluminium drift tube is 3 cm in diameter with a central anode wire of gold-plated tungsten 50 μm in thickness and with an applied potential of 3080 V. The length of the drift tubes can range from 1 m to 6 m. They contain mainly argon (93%), but also CO_2 (7%) and water (added to improve high voltage stability). Figure 2.8 shows the structure of an MDT chamber in the Barrel.

Segments of muon tracks are reconstructed in the MDTs as follows. When a charged particle passes through the gas it generates electron-ion pairs. Due to the high voltage the electrons are accelerated toward the anode while the ions drift toward the wall of the tube. Therefore further electron-ion pairs are created, eventually leading to an avalanche and a detectable signal, a so-called "hit". An estimate of the minimal distance of the muon trajectory to the central wire (called the $drift\ radius$) is given by the time taken for the signal to arrive at the anode. The spatial

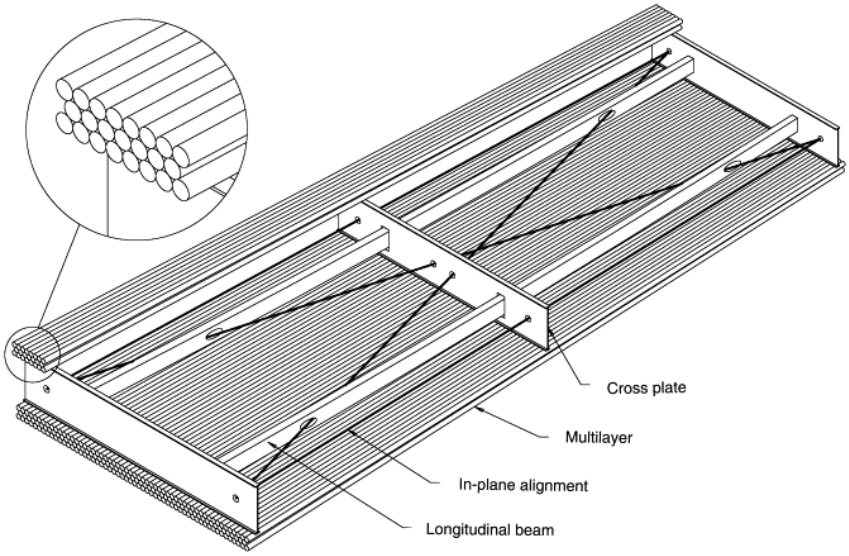

Figure 2.8: *Structure of a MDT chamber [7].*

resolution of one chamber is 35 μm while that of a drift tube is approximately 80 μm in z (Barrel) and r (Endcaps). Once the drift radius has been measured for each tube on which there is a hit, a tangential line to the drift circles is fitted and this gives an approximation of the muon trajectory within one MDT chamber. These fitted lines are called segments of the muon track.

In the Barrel there are three concentric sets of MDT stations around the beam line at radii of 5 m, 7.5 m and 10 m. Each Endcap has three MDT wheels perpendicular to the beam line with distances from the IP of $|z| \approx 7.4$ m, 14 m and 21 m. Altogether there are approximately 1,200 MDT chambers. For a precise sagitta measurement it is required that all muons coming from the IP will intersect at least three MDT chambers.

Cathode Strip Chambers (CSCs): In the forward Endcap regions for $2.0 < \eta < 2.7$ the muon rate is very high and high granularity CSCs are used instead of MDTs for precision measurements on the closest Endcap wheel to the beam line. The operation of these chambers is similar to that of the drift tubes, with muons creating avalanches of electron-ion pairs in the gas.

Each chamber is made of four alternating planes of anode wires and cathode strips where signals from each muon track is collected. The accurate position of each track can therefore be determined by combining information from adjacent cathode strips. The strips of two cathode planes are arranged perpendicular to give a measurement both in the r and azimuthal ϕ coordinates. With a total of 30,700 channels, and an excellent time resolution of 7 ns, the CSC has a resolution in the

radial direction of 40 μm whereas in r-ϕ it is about 5 mm.

Trigger technologies

Muons are identified by the trigger via signals in the RPCs and the TGCs. These have a coverage in pseudo-rapidity $|\eta| < 2.4$ and over the full ϕ range. They provide fast information about the track momentum after just a few tens of nanoseconds after the track passes through the detector. In order to achieve this, the technologies in place must generate fast signals and have a fine readout granularity. Moreover they provide a bunch crossing identification with a time resolution better than the LHC bunch spacing of 25 ns.

Resistive Plate Chambers (RPCs): In the Barrel region, for $|\eta| < 1.05$ RPCs made up the muon trigger system. Each RPC unit is made of two parallel plates of Bakelite, a resistive material, and the 2 mm gap between them is filled with gas (97% $C_2H_2F_4$ and 3% C_4H_{10}). In order for a charged particle to create an avalanche when passing through the gas, a uniform electric field of 4500 V/mm is applied between the two plates. The signal from the charged particle is detected on the metallic strips on the outer sides of the plates. The strips on one plate are orthogonal to those on the other plate, so that the η coordinate can be precisely measured as well as the ϕ coordinate. Due to the ATLAS feet, toroids support structure and other services, the η-ϕ coverage of the RPC system is about 80% . An RPC chamber has a spatial resolution in η and r-ϕ of 10 mm and a time resolution of 1.5 ns. The signal width is 5 ns, and therefore the bunch crossing identification is very accurate.

Just like the MDTs, the RPCs are arranged in three concentric stations around the beam line. Two of the three stations are placed at the top and bottom of the middle Barrel MDT chambers (the *pivot-plane* and the *low-p_T plane* respectively), while the third one is placed on top of the outer Barrel MDT station and is also known as the *high-p_T plane*. Figure 2.9 shows a schematic overview of the muon trigger system in ATLAS.

Thin Gap Chambers (TGCs): The TGCs are the fine granularity trigger technologies used in the Endcap regions of the Muon Spectrometer where the radiation level is much higher than in the Barrel. With their high rate capability and good time resolution (4 ns), the TGC system covers the region $1.05 < |\eta| < 2.7$, although the region beyond $|\eta| = 2.4$ is not used for triggering. There are four wheels of TGCs in each Endcap, one before the Endcap toroids and three after it. The bottom part of Figure 2.6 shows how the TGCs are spatially distributed in the Endcaps. They are made of two cathode plates separated by 1.4 mm gas mixture of C_5H_{10} and CO_2. Anode wires with an applied voltage of 3100 V are placed in between the plates and

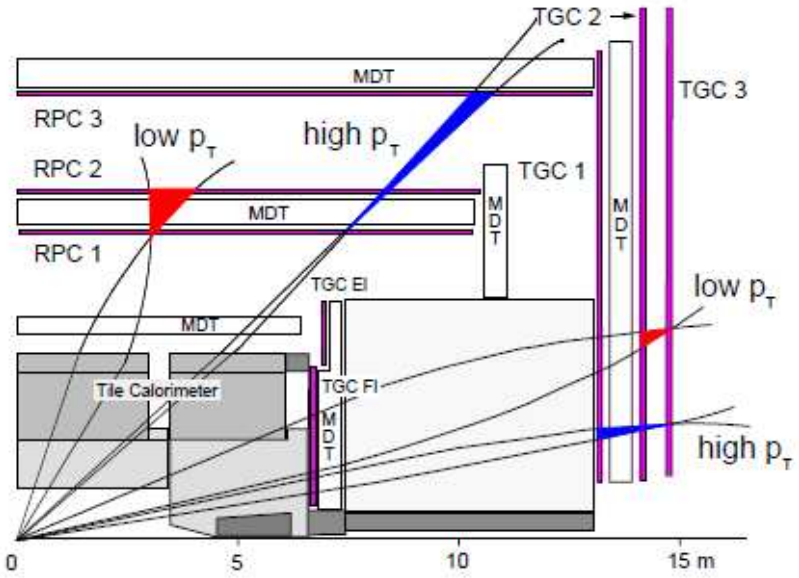

Figure 2.9: *Schematic view of the muon trigger system in ATLAS [8].*

are evenly separated by 1.8 mm. Each wire collects ionisation electrons caused by the intersecting muon. Combining all of these measurements across the wires with hits it is then possible to estimate the trajectory of the particle. The spatial measurement is also possible given that the TGC chambers are combined into two or three layers. Furthermore the TGCs are able to give a measurement both in the radial and in the azimuthal coordinates, given that the anode wires run parallel to the MDT wires whereas the cathode readout strips run in the radial direction.

The spatial resolution of the TGCs is less than 6 mm in r and less than 7 mm in r-ϕ. As in the case of the RPCs, the trigger logic in the TGCs is based in coincidence (in η and ϕ) conditions in two or more stations, depending on the track momentum.

2.2.4 Trigger and Data Acquisition System

At the design luminosity of $10^{34}\,\mathrm{cm}^{-2}\mathrm{s}^{-1}$ the LHC's maximum bunch crossing rate is 40 MHz at each of the four interaction points (ATLAS, CMS, LHCb[1], ALICE). The ATLAS trigger system is designed to reduce this rate, and record events at approximately 200 - 600 Hz. In order to do so, the trigger system is made of three levels, as schematically illustrated in Figure 2.10.

[1]The luminosity delivered at the LHCb interaction point can be lowered by separating the two beams, such that they do not collide head-on. Therefore the LHCb experiment, depending on the filling scheme, has the same number of colliding bunches as the other experiments, but the average number of interactions per bunch crossing can be lower.

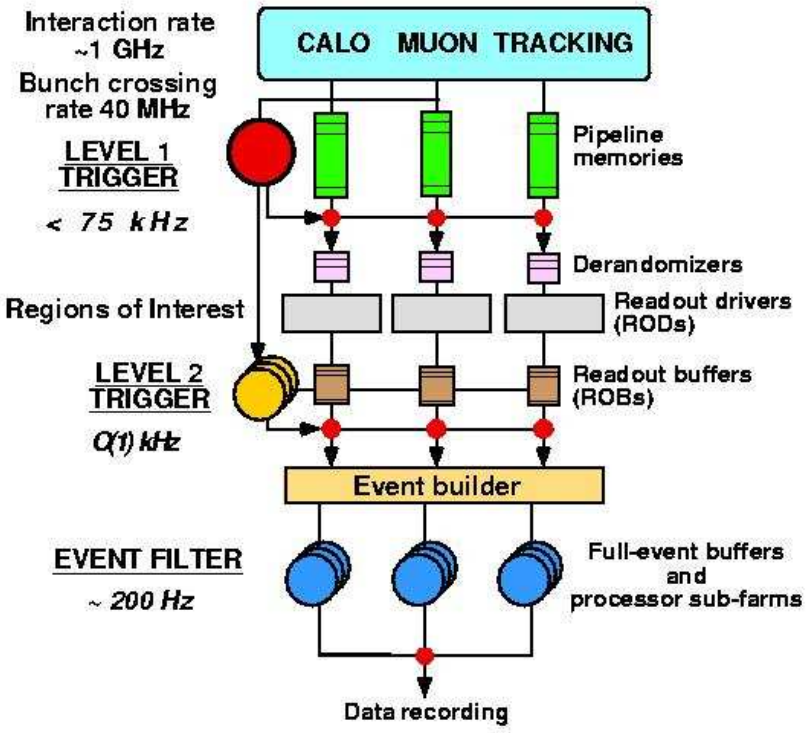

Figure 2.10: *Schematic overview of the ATLAS trigger system [8].*

The Level 1 (L1) is hardware-based and uses information from the calorimeter and the fast muon trigger detectors at reduced granularity. The latency of the L1 trigger is 2 μs and it leads to a reduction of the input rate to a maximum of 75 kHz (30 kHz in 2010). The other important task of the L1 trigger is to identify Regions of Interest (RoIs) in each event. These are regions of the detector where interesting objects such as high energy muons may be present. From the readout buffers, (ROBs) all event information within the RoIs are then passed to and investigated by the other trigger levels.

The Level 2 (L2) trigger is software based and uses the full granularity information of all subdetectors within the RoI. L2 further reduces the rate to about 3 kHz, with a latency of 1 ms to 10 ms, depending on the complexity of the event. This is only possible because of the existence of the RoIs at L1, the maximum required latency would be often exceeded if the L2 trigger had to cope with the full event information. The disadvantage of this approach is that if an event fails to pass the L1 trigger, it cannot be looked at at L2, and in some cases interesting objects are lost.

The information of each event passing the L2 trigger is collected from the ROBs

by the Event Builder and passed to the last trigger level, the Event Filter (EF), where the final decision is taken on whether to store the event for offline analysis or to reject it. With a relatively long decision time of about one second, the EF uses offline reconstruction algorithms, and also alignment and calibration information. With the EF a further rate reduction is achieved to have a final target rate of 200 Hz [37]. Together L2 and EF are known as the High Level Trigger (HLT). All the events that pass the EF are written to tape at the so called Tier-0 centre at CERN and then distributed worldwide via the LHC Computing Grid (LCG) for offline analysis.

2.2.5 Muon reconstruction and trigger

Muon reconstruction

Muons can be reconstructed in ATLAS in two different ways, either using the Muon Spectrometer information only ("standalone" muons) or by combining the MS with the ID and the Calorimeter information ("combined" muons).

The reconstruction of a standalone muon starts locally in a muon chamber, where a straight line track segment in the bending plane is searched for. In order to do this all hit information in the MDTs and CSCs are used and the segment candidates are required to come from the IP. If available, the ϕ coordinate measured by the trigger is associated to the segment. A muon track candidate is then formed by combining at least two track segments in different muon stations. All track parameters, such as p_T, η, ϕ, are obtained from the track by fitting this to the interaction point, and by taking into account multiple scattering and the amount of energy loss in the calorimeters. The typical muon energy loss in the calorimeters is about 3 GeV.

Combined muons are defined by associating the standalone muon track to an inner detector track. In the ID tracks are reconstructed using two pattern recognition algorithms. The first one, also called the "inside-out" tracking, starts with the silicon information and then adds TRT hits. This procedure is capable of reconstructing tracks with a p_T of at least 300 MeV. The second pattern recognition algorithm only takes into account hits not used in the first step, starting from the TRT and working inwards adding as many silicon hits as it finds. This second step is performed in order to recover tracks from secondary decays. In order to define a combined muon, standalone muons and ID tracks are associated using a χ^2 test. This is defined as the difference between the track parameters in the ID and MS, weighted by their covariance matrix. The parameters of the combined track can be derived either from a statistical combination of the two initial tracks (`Staco` algorithm), or from

the refit of the full track (`Muid` algorithm).

A third class of muons can be defined. This are called *tagged* muons. For these the reconstruction in the muon spectrometer fails, either because of too low p_T or because of the acceptance. In this case the approach is to extrapolate the ID track to the inner or middle stations of the MS and look for a track segment in these stations which is not associated to a MS track.

Finally another muon family can be defined as the class of *calo-muons*. This algorithm does not take into account any MS information, but uses ID tracks extrapolated to the calorimeter system. If the energy deposit associated to the track is compatible with the hypothesis of a minimum ionising particle, a calo muon is defined.

Muon trigger

The L1 muon trigger covers the pseudo-rapidity region $|\eta| < 2.4$, with the transition between the Barrel and the Endcaps regions at about $|\eta| = 1.05$. Furthermore, it provides six p_T thresholds at 4 GeV, 6 GeV and 10 GeV (the low-p_T thresholds), and 11 GeV, 20 GeV and 40 GeV (the high-p_T thresholds). Each trigger selects muons with p_T greater than the threshold value. In 2010 the 4 GeV threshold has not been used; in fact no minimum p_T requirement was applied on the muon at L1. This is called the 0 GeV threshold. The overall coverage is about 85 %, due to the feet of ATLAS, passage of services and also the support of the toroid coils that reduce the space coverage.

In the Barrel region, the pivot-plane of RPCs is the first seed of the trigger logic. In case of a hit in the pivot-plane, the trigger logic looks for hits in the low-p_T plane, in the same defined road and within the same time interval of 25 ns. If at least one hit is found, the low-p_T trigger is issued. Fake muon signals are minimised by requiring hits in at least three of the four RPC layers in the two stations, two pivot layers and two low-p_T. Every time the low-p_T trigger is issued, the trigger logic looks for hits in the high-p_T plane in the same road and again in the same bunch crossing. If at least one hit is then found, the high-p_T trigger is fired, otherwise the low-p_T trigger is.

Being defined this way, the high-p_T trigger always requires a low-p_T trigger, and in case of multiple triggers, only the highest p_T trigger threshold will be recorded. This is important for trigger efficiency measurements; the inefficiency of the high-p_T trigger will contain the inefficiency of the low-p_T ones.

In the Endcaps ($1.05 < |\eta| < 2.4$) the muon trigger is based on signals in the TGCs (see Section 2.2.3). The L1 algorithm requires a coincidence of hits in the

three trigger stations within a road which follows the muon trajectory from the IP through the whole detector. The width of the road is related to the p_T threshold that will be applied at L1. In the forward region, at the outer edge of the TGCs, the inefficiency of the system is due to the magnetic field. Here, depending on their charges, muons can bend away from the TGCs acceptance. The overall geometric acceptance of the TGCs is about 98 %.

At L2, as already mentioned, the algorithms can only access information restricted to the RoIs identified at L1, in order to reduce the time taken for the decision to be made. The typical RoI size is $\Delta\eta$ x $\Delta\phi = 0.1 \times 0.1$. At L2, fast algorithms perform the reconstruction of the muon track taking into account also information from precision chambers (MDTs and CSCs) and combining the MS track measurement to the measurement in the ID. Finally the EF uses algorithms to performs a more detailed track reconstruction similar to the ones used for offline event reconstruction.

Even after an event has fired the trigger, it could be still rejected by the prescale. This number, decided by the various physics groups, defines how many events which pass a certain trigger item will be considered at the next level. The rejection happens in an absolutely random way. The prescale is used to keep high cross section processes and to record a fraction of unbiased events for background studies. If a trigger enters the trigger menu with a prescale "N", it means that for every N events which would fire the trigger, N-1 events are discarded, while one, randomly chosen, is recorded.

The convention used in ATLAS to distinguish different triggers is to use the trigger level and the threshold, such that for example `L1_MU6` corresponds to the L1 trigger, where at least one muon with $p_T > 6\,\text{GeV}$ has fired. In case of multiple object triggers the notation is similar, but the number of objects required to have fired is also specified. For example `EF_2mu10` corresponds to a EF trigger with the requirement that at least two muons with $p_T > 10\,\text{GeV}$ have fired the trigger.

2.3 Luminosity collected by trigger chains

In 2010 the LHC delivered $48.1\,\text{pb}^{-1}$ of integrated luminosity, whereas ATLAS recorded $45.0\,\text{pb}^{-1}$. See the ATLAS public result in Figure 2.11 for details. Not all of these events are used for physics analysis. During a run, once stable beam conditions are first reached, there is a period called the 'warm start' during which the inner detector system (except for the TRT) ramps to high voltage (SCT) and the preamplifiers are turned on (Pixels). In 2010 this caused a 2.0% inefficiency.

Other sources of loss in efficiency are reported in Figure 2.12. These give all together about 3.6% loss in efficiency between the online delivered luminosity and the offline recorded one.

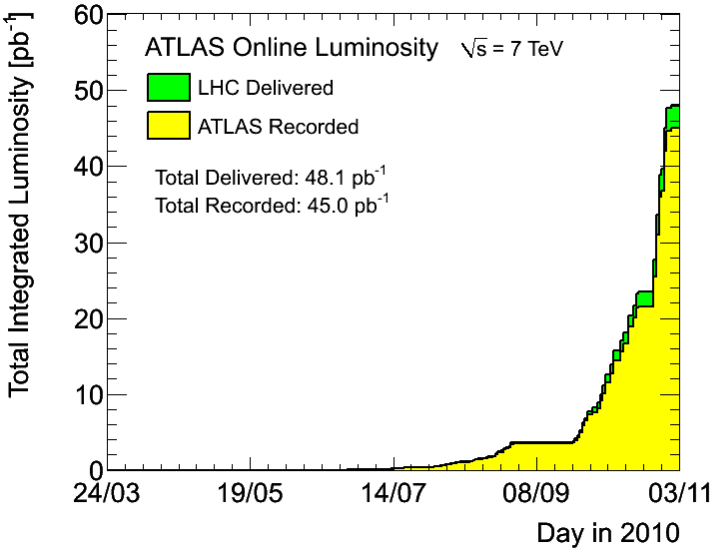

Figure 2.11: *Cumulative integrated luminosity delivered by the LHC (green) and recorded by ATLAS (yellow) during stable beam periods in 2010 [9].*

Inner Tracking Detectors			Calorimeters				Muon Detectors			
Pixel	SCT	TRT	LAr EM	LAr HAD	LAr FWD	Tile	MDT	RPC	CSC	TGC
99.1	99.9	100	90.7	96.6	97.8	100	99.9	99.8	96.2	99.8

Luminosity weighted relative detector uptime and good quality data delivery during 2010 stable beams in pp collisions at √s=7 TeV between March 30th and October 31st (in %). The inefficiencies in the LAr calorimeter will partially be recovered in the future.

Figure 2.12: *The table in the figure shows the efficiency of each subdetector in ATLAS with respect of the online LHC delivered luminosity [10].*

A skim of luminosity blocks is performed in order to keep all of those during which each subdetector recorded data without problems. At the end of this process a so-called Good Runs List (GRL) is agreed and used for physics analysis [38]. Therefore the total integrated luminosity is lower than the one recorded by ATLAS. For the 2010 data taking period, a total integrated luminosity of $\approx 36\,\mathrm{pb}^{-1}$ is available for physics analysis with a total uncertainty on the luminosity of 3.4%. The data collected by ATLAS are organised into runs, approximately one for each LHC fill. All of the runs for which the beam conditions are roughly the same are collected into data periods. In 2010 the ATLAS collaboration grouped the runs into nine data periods, labelled A to I.

Chapter 3

Lorentz angle measurement for the ATLAS SCT

This chapter describes the study performed in order to measure the Lorentz angle in the ATLAS SCT.

The Lorentz angle is measured in the Barrel region of the SCT and it depends on the bias voltage applied to the modules, their temperature and the external magnetic field. The measurement is performed through the study of the cluster width and, under the normal SCT operating conditions, it is estimated to be about four degrees. Previous studies performed on cosmic-ray data collected in 2008 and 2009 show good agreement with the model prediction; results can be found in [39]. A so-called "null test" is also shown in [39] and in [40], where the Lorentz angle is measured in the absence of the magnetic field. In this case the results are consistent with zero degrees, as expected.

In the study presented here both cosmic-ray and collision data at $\sqrt{s}$ =7 TeV are considered. A comparison with the MC simulation is also shown.

3.1 SCT overview

The SCT consists of 4088 silicon crystal semi-conductor modules, each of which is made of two wafers of silicon micro-strip detector glued back-to-back with a stereo angle of 40 mrad. The 40 mrad stereo angle facilitates measurements of the z-coordinate via combining hits on both sides of a module.

The readout electronics are mounted on the module on a hybrid. The hybrid supports 12 readout chips, six on each side of the module. Each chip provides information about whether the charge in each of 128 strips exceeds a certain threshold, nominally set to 1 fC. As a result there are 768 aluminium strips per wafer. The

strips are 6.4 cm in length, with a separation of 80 μm and are biased with a voltage of 150 V (nominal). A complete description of the SCT and its commissioning can be found in [41].

The Barrel region has a pseudo-rapidity coverage in the range $|\eta| < 1.4$ and is made of four concentric cylindrical layers. Conventionally the innermost layer is named Layer 0 and the outermost is named Layer 3. The layers are not identical to each other, instead they are designed with radii of 20 cm, 37.3 cm, 44.7 cm and 52 cm, and contain 32, 40, 48 and 56 rows of modules respectively, giving a total of 2112 Barrel modules, on which the strips are designed to run approximately parallel to the beam line.

Each SCT Endcap is made of nine disks, for a total of 988 modules per Endcap and a pseudo-rapidity coverage that extends to about $|\eta|$ =2.5. Each track crosses at least four disks in this region. In the Endcap modules the strips run radially from the beam line.

3.1.1 SCT readout

When a charged particle passes through a module, it produces electron-hole pairs. The charge from the holes is collected on the strips. The SCT readout is binary and it is registered in three 25 ns time bins around the Level 1 accept signal. During the 2009 cosmic-ray data taking period (and also during 2010 proton-proton collision period), the SCT was configured such that it would record a hit on a strip, if the charge deposited was greater than the nominal threshold of 1 fC, in any of the three time bins.

In each hit pattern (i.e. XYZ where X,Y and Z can be equal to zero or one), the first time bin corresponds to the bunch crossing preceding the Level 1 accept, the second one to the same bunch crossing as the Level 1 accept and the third one to the bunch crossing following the Level 1 accept. The detector must therefore be timed in with the trigger. In order to have such correspondence between modules and trigger, delays are applied to the trigger signal to compensate for the length of the optical fibres that transmit the trigger signal, the trigger latency, and for the time-of-flight of particles from the interaction point (IP) to the module. During the 2009 cosmic-ray data taking period, delays regarding the time-of-flight were not yet applied.

If the SCT modules are correctly timed in, real hits should follow a “01X” hit pattern, with no signal in the first bin, over threshold in the second bin, and no requirement on the last bin. Noise corresponds to hit pattern such as “101”, “100” or “001”, while “111” hit pattern signifies that the module is stuck in a state which

always registers a signal above threshold.

The possible dependence of the Lorentz angle value on the timing is investigated in Section 3.3.2.

3.1.2 Local coordinate frame in the SCT Barrel

The ATLAS global frames (x, y, z) has been already defined in Section 2.2. Here the local coordinate frame ($LocX$, $LocY$, $LocZ$) on the Barrel modules of the SCT is defined. Figure 3.1 shows a diagram of the four SCT Barrel layers in the ATLAS x-y plane, with the z axis orthogonal to the x-y plane with positive direction pointing out of the paper.
The local coordinate frame on the module are defined as [42]:

- The origin of the local frame i.e. (0, 0, 0) is defined at the centre of the module,
- $LocX$, $LocY$ and $LocZ$ are right handed Cartesian coordinates,
- the $LocX$ and $LocY$ coordinates are defined in the plane of the module and run parallel to the symmetry axis of the module,
- the $LocY$ axis corresponds to the ATLAS z direction ($LocY$ runs parallel to the strips),
- the $LocX$ axis on the module plane is perpendicular to the $LocY$ axis,

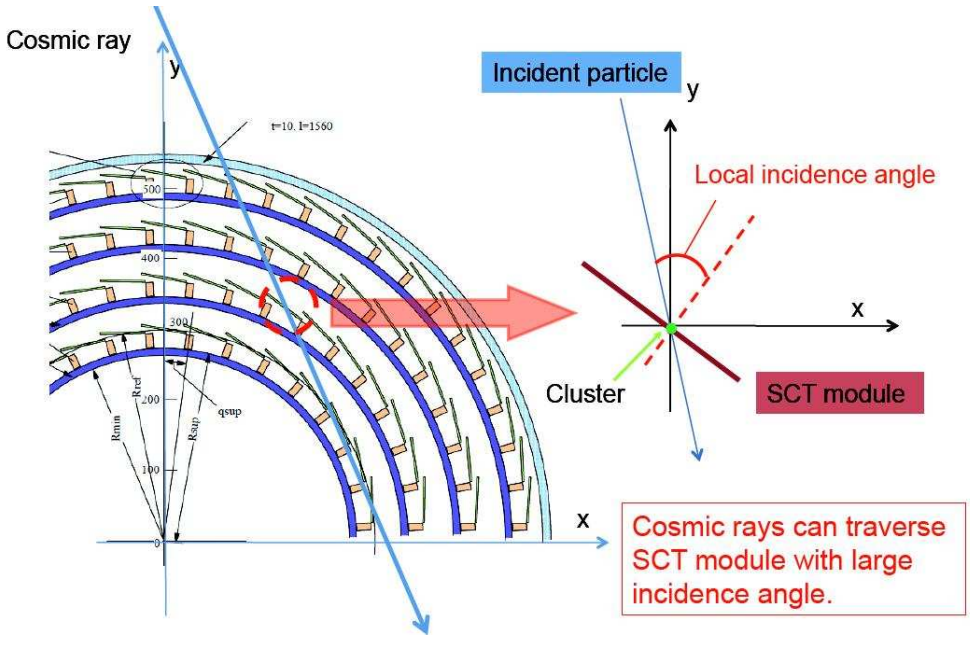

Figure 3.1: *Drawings of the SCT transverse section and the SCT wafer.*

- the *LocZ*axis is normal to the module plane.

The local incidence angle is part of the system of local coordinates and is shown schematically in Figure 3.1. It is calculated in the *LocX*-*LocZ*plane, with positive angle defined anti-clockwise from the *LocZ*axis, when looking from the negative z axis of ATLAS.

3.2 Lorentz angle model in the ATLAS SCT

The SCT operates in the ATLAS 2 T solenoidal magnetic field. The presence of the magnetic and electric fields affects the drift of the charge carriers (electrons and holes) in the silicon due to the Lorentz force. The angle by which the charge carriers are deflected is called the Lorentz angle. This is particularly relevant for the modules in the Barrel region; here the direction of the charge carrier drift is perpendicular to the magnetic field. In the Endcaps the direction of the charge carrier drift is almost parallel to the magnetic field and therefore no effect of the magnetic field is expected to be observed.

When a minimum-ionising particle passes through the SCT silicon modules, it loses part of its energy according to dE/dx where E is the energy of the particle and x the distance travelled through the material. The energy loss corresponds to about 72 electron-hole pair creations per micron. In the SCT, holes are collected at the p-type electrode, while electrons drift towards the n-bulk. In order for a particle to leave a signal, a minimum charge of 1 fC has to be deposited. A detailed description of how the collected charge is transformed into a digital signal can be found in [43].

According to the model prediction the Lorentz angle in the SCT Barrel is estimated to have a magnitude of about four degrees. This corresponds to a maximum 20 μm shift over the 285 μm sensor thickness, and it is comparable to the 80 μm distance between strips. Therefore the measurement of the Lorentz angle is necessary for detector alignment, cluster width determination, and position resolution.

The most relevant information used in this study is the SCT cluster width, defined as a set of contiguous strips above threshold. More specifically, a cluster is a collection of hits in adjacent strips, with the cluster width being the number of strips within it. The Lorentz angle corresponds to the incidence angle for which the average cluster width has its minimum.

Parameter	Value for holes
v_s	$1.68 \times 10^8 \times T^{-0.52}$ cm sec^{-1}
E_c	$1.24 \times T^{1.68}$ V cm^{-1}
β	$0.46 \times T^{0.17}$
γ	0.72-0.0005(T-273)

Table 3.1: *Parameterisation values (valid for holes) used for the drift mobility calculation [13].*

3.2.1 Lorentz angle definition and prediction

The Lorentz angle ϕ_L depends on the mobility of charge carriers as well as the external magnetic field. For silicon in a magnetic field B, the relation between the above factors is [44]:

$$\tan \phi_L = \mu_H B = \gamma \mu_d B \,, \tag{3.1}$$

where μ_H is the Hall mobility, μ_d is the drift mobility and their ratio γ is a pure number approximately equal to unity called the Hall factor. The mobility is defined as the ratio between the drift velocity and the electric field.

At large values of the electric field the drift velocity for both electrons and holes saturates leading to a decrease of the mobility. Therefore the Lorentz angle at high electric field values becomes smaller.

The drift mobility μ_d is given by [13]:

$$\mu_d = \frac{v_s/E_c}{[1 + (E/E_c)^\beta]^{1/\beta}} \,, \tag{3.2}$$

where E is the electric field, v_s is the saturation velocity, E_c is the electric field scale at which the transition from the linear regime to the saturation occurs, and β describes the transition between the two regimes. Equation 3.2 is valid for SCT sensors with temperatures above 250 K. The values of these parameters are shown in Table 3.1. The mobility for electrons is about a factor of two larger than the one for holes, therefore the Lorentz angle measured for electrons (Pixel detector for example) is accordingly larger [45].

For SCT sensors with about 70 V depletion voltage[1] in a 2 T magnetic field the dependence of the Lorentz angle on the bias voltage is given by:

$$\left.\frac{\partial \phi_L(V,T)}{\partial V}\right|_{150V,273K} \simeq -0.005 \text{ (degrees}/V) \,, \tag{3.3}$$

[1]The depletion voltage is the minimum applied voltage to have fully depleted sensors.

while the dependence on the temperature is given by:

$$\left.\frac{\partial \phi_L(V,T)}{\partial T}\right|_{150V,273K} \simeq -0.027 \text{ (degrees}/K). \tag{3.4}$$

The SCT digitisation model and the study shown in what follows assume a uniform electric field inside the modules. The electric field along the z direction of the sensor is given by [43]:

$$E_z = \frac{V_B + V_D}{d} - 2\frac{V_D}{d^2} z\,, \tag{3.5}$$

where V_B is the bias voltage (nominal value of 150 V), V_D is the depletion voltage (nominal value of 70 V) and d is the sensor thickness (285μm). The Lorentz angle is determined in the centre of the sensor at $z = d/2$.

The model prediction for the Lorentz angle value (using the above equations), for a temperature of $T = -2°$C (layers 0, 1, 2) and $T = 4.5°$C (Layer 3) and a magnetic field B of 2 T is:

$$\begin{aligned} \phi_L(T = -2°\text{C}) &= 3.88° \pm 0.28°\,, \\ \phi_L(T = 4.5°\text{C}) &= 3.71° \pm 0.27°. \end{aligned} \tag{3.6}$$

The drift velocity v_d uncertainty dominates the systematic errors, along with the electric field non-uniformity. Both these uncertainties are currently set to 5%; The uncertainties of 0.03°C on the temperature, and 0.75% on the magnetic field, also provide small contributions to the systematic uncertainty on the Lorentz angle measurement. The contribution to the systematic uncertainty from the bias voltage is negligible.

The model predictions shown in Equation 3.6 are used to compare the measured Lorentz angle in data.

3.2.2 Lorentz angle extraction

In the absence of a magnetic field, the minimum cluster width occurs at a local incidence angle (defined in Section 3.1.2) of zero degrees. The presence of electric and magnetic fields generates a Lorentz force in the silicon strips, so with a B field, the minimum cluster width no longer occurs at zero incidence angle, but at the Lorentz angle value.

To extract the value of the incidence angle corresponding to the minimum cluster

width, profile distributions of the average cluster width versus the local incidence angle are considered where each cluster contributes one entry to the profile plot. A fit is performed to extract the incidence angle for which the average cluster width has its minimum, i.e. the Lorentz angle.

The fitting function is an empirical function and it is the same as that already used in [39]:

$$\begin{aligned} f(\phi) &= (a|\tan\phi - \tan\phi_L| + b) \otimes \text{Gaussian}(\phi) \\ &= \int_{-\infty}^{+\infty} (a|\tan\phi' - \tan\phi_L| + b) \frac{1}{\sqrt{2\pi}\sigma} \exp\left(-\frac{(\phi-\phi')^2}{2\sigma^2}\right) d\phi' \,. \end{aligned} \tag{3.7}$$

The function has four free parameters: the Lorentz angle (ϕ_L), the slope of the distribution (a), the minimum cluster width (b) and the smearing effect (σ). The fit is initially performed in the same incidence angle range as in the previous analysis [39], i.e. $\pm 12.5^\circ$ around the minimum. This has been optimised based on cosmic-ray data. The optimisation of the fitting range on collision data has been performed and is presented for collision data in Section 3.4.2.

3.3 Analysis on cosmic-rays

The analysis using cosmic-ray data has been performed within the `ATHENA` framework using release 15. The type of data used is the `physics_IDCosmic` stream.

3.3.1 Track selection

When analysing cosmic-ray data, a very loose track selection is applied in order to retain the maximum number of good quality tracks. The selection is the same as presented in [39] and is applied to all cosmic-ray data analyses used for Lorentz angle measurement. The selection requires:

- at least eight silicon hits or at least 30 TRT hits,
- transverse impact parameter $|d_0|$[2] $\leq 500\,\text{mm}$,
- transverse momentum $p_T \geq 1\,\text{GeV}$,
- -10 ns$\leq$ TRT event phase [3] $\leq 40\,\text{ns}$ (not zero).

[2]The impact parameter d_0 is defined as the distance of closest approach of the muon track in the transverse plane.

[3]The TRT event phase is a measure of the time of an interaction. In collision data this is

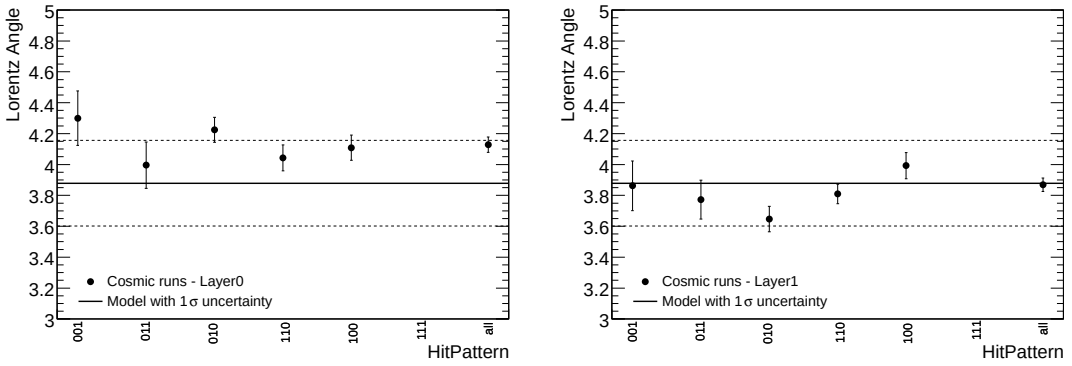

(a) (b)

Figure 3.2: *Lorentz angle measured as a function of the various hit patterns for the cosmic-ray data runs listed on Table 3.2. Results for Layer 0 (a) and Layer 1 (b) are shown. The fit for hit pattern "111" did not converge, so it does not show in the plot. The horizontal lines represent the model prediction: the continuous line is the central value, while the dashed lines represent the model uncertainty.*

3.3.2 Hit patterns

This study is performed to check whether or not the Lorentz angle depends on the hit pattern (see Section 3.1.1). Each cluster entering the distribution of average cluster width as a function of incidence angle is selected with a hit pattern consistency requirement, i.e. only clusters where all strips have the same hit pattern contribute to the same distribution. For each of the runs listed in Table 3.2, layers 0, 1 and 3 are set to the nominal voltage of 150 V while the voltage setting on Layer 2 varies from run to run. Moreover the temperature of the layers is not uniform: layers 0, 1 and 2 are set to about -2°C while the temperature of Layer 3 is about $+4.5$°C. Adding together all runs, only results for layers 0 and 1 can be compared.

For each layer, the profile distributions of average cluster width as a function of local incidence angle are fitted to determine the Lorentz angle as the minimum of the distribution. Figure 3.2 shows the Lorentz angle value for each hit pattern in layers 0 and 1. The hit pattern named "all" is the combination of all the hit patterns from "001" to "111". Hit patterns "000" and "101" are omitted.

The fits for both layers for the "111" hit pattern do not converge, due to the limited number of clusters contributing: this also indicates that the number of Barrel

defined as the time when a track passes through the Barrel of the TRT detector with respect to the 25 ns bunch crossing. For cosmic-ray muons however this time is measured with respect to the readout window as measured by the TRT, since cosmic-rays can pass through the detector at any time. The event phase information includes readout window offset and time of flight effects. The selection adopted here is the common loose selection used in cosmic-ray analysis on ATLAS. For more information about the TRT event phase refer to [46].

Layer 2 HV	Run number	Date
30 V	136455, 136459, 136460, 136599	October 2009
40 V	136379, 136409	October 2009
50 V	135863, 135855, 136183, 136176, 135926	October 2009
60 V	135664, 135736, 135813, 135816	October 2009
100 V	139016	October 2009
150 V	134967, 135106	October 2009
	147931	February 2010
200 V	135140, 135146, 135195	October 2009
250 V	135304, 135351, 135356	October 2009
300 V	135388, 135441	October 2009
	148072	February 2010
350 V	148209	February 2010

Table 3.2: *List of cosmic-ray runs in which the voltage applied on Layer 2 changes. Three runs at nominal 150 V are also included.*

modules in this state is very small. All the other fits converge, but the resulting statistical errors are often large.

Overall a hit-pattern dependence is not observed from the results of this investigation, as the measured differences are within the statistical uncertainty. Moreover, the Lorentz angle measured for each hit pattern is in good agreement with the model prediction.

3.3.3 HV dependence

As already discussed, the Lorentz angle depends on the magnetic field, the sensor temperature and the voltage applied. Here the dependence of the Lorentz angle on the applied voltage is investigated. Between October 2009 and February 2010, a different voltage was applied to Layer 2 of the SCT Barrel for several cosmic-ray runs. Table 3.2 summaries these special runs with the corresponding applied voltage on Layer 2.

Figure 3.3 shows the dependence of the average cluster width on the local incidence angle for the different voltage configurations. The distribution for the 30 V run is very flat around the minimum, so the fit does not converge and the Lorentz angle cannot be extracted using the function given in Equation 3.7.

Figure 3.3 also shows that, for the runs for which the sensors are not fully depleted (30 V, 40 V, 50 V, 60 V), the average cluster width increases as the voltage increases for any given incidence angle. This is expected, since as the applied voltage is raised, the deposited charge increases, giving a larger cluster width. The effec-

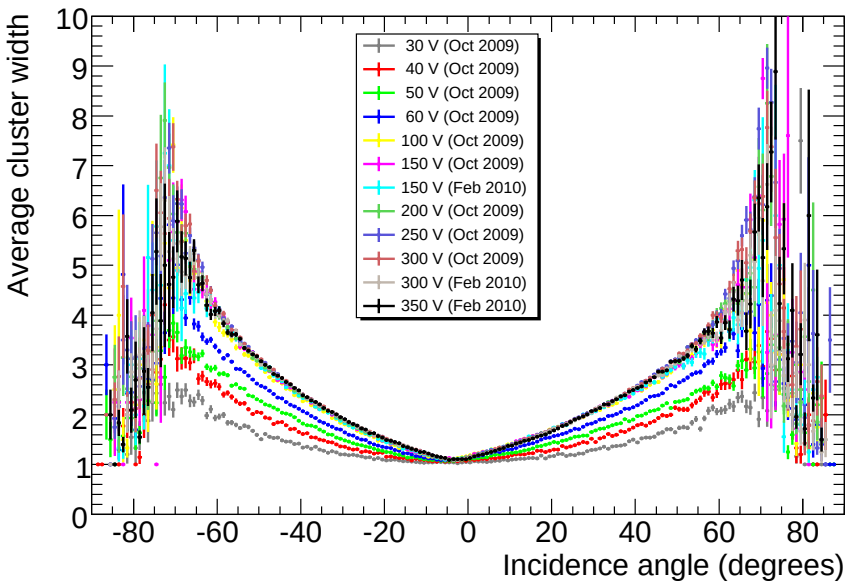

Figure 3.3: *Distribution of the average cluster width as a function of the local incidence angle for various cosmic-ray runs corresponding to different voltage applied to Layer 2 of the SCT Barrel. The voltage value for this layer changed between 30 V and 350 V.*

tive fitting function used is not optimised for describing such distributions, and, in addition, it is possible that the model does not describe these configurations adequately. Moreover, these effects are hard to disentangle in this study, since there was not enough cosmic-ray data collected in order to have a large sample of tracks contributing to the distributions.

The predicted value of the Lorentz angle as a function of the applied voltage is shown in Figure 3.4 for six different sensor temperatures. For all of the runs listed in Table 3.2, Layer 2 has a temperature of $-2°C$, therefore the comparison with the model prediction has to be done with respect to the green line in Figure 3.4. The plot also shows the resulting values of the Lorentz angle for each voltage in the above listed cosmic-ray runs: these values are obtained fitting the distribution of the average cluster width as a function of the local incidence angle ϕ using a fitting range of $\pm 12.5°$ from the minimum. The black markers refer to the October 2009 runs and the red ones to the February 2010 runs. The errors shown are statistical only. The runs in which Layer 2 has the same voltage applied are merged together. The applied voltage was changed only for Layer 2, therefore this study has not been repeated for the other layers.

The Lorentz angle measured for voltages below depletion voltage is above the model prediction for applied voltages of 40 V, 50 V and 60 V. A Lorentz angle value

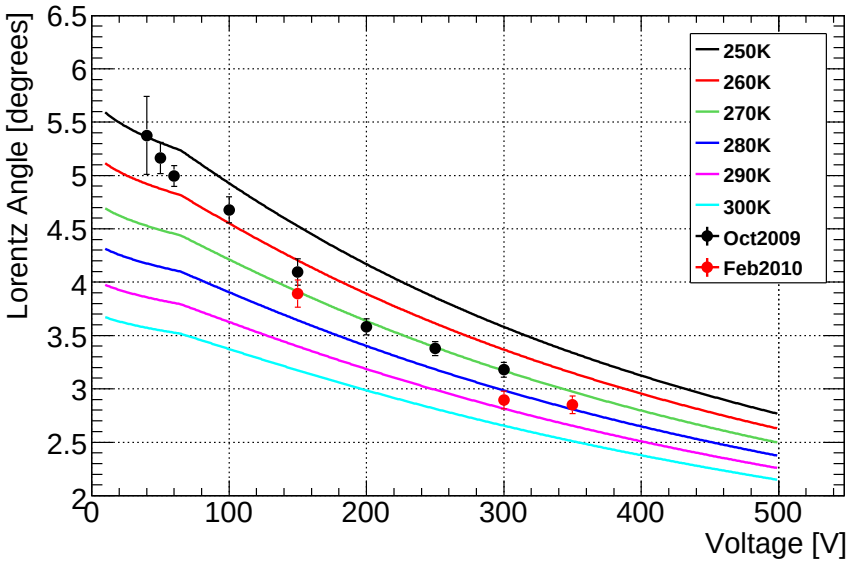

Figure 3.4: *Lorentz angle value as a function of the applied voltage. Continuous lines show the temperature dependence of the Lorentz angle value from the model. Points correspond to fit results for Layer 2 of the SCT Barrel as this is the only one on which the applied voltage changed in each run. Black points represent the October 2009 runs, while the red ones are from the February 2010.*

above the model prediction is also measured for the 100 V run, while for higher applied voltages most of the fit results give a good agreement between the measured value and the model prediction. A difference can be seen for the 150 V and 300 V results. Here two values are extracted, from October 2009 and for February 2010 cosmic-ray data runs, respectively. The 150 V most recent result marked in red is in very good agreement with the model prediction, whereas the October 2009 value is significantly higher. The opposite is seen for the 300 V runs, where the latest result from February gives a Lorentz angle value significantly lower than the model prediction. Unfortunately no other runs were taken with applied voltage different from the nominal 150 V, so this effect could not be investigated further.

3.4 Analysis on collision data

Within each run of collision data, only luminosity blocks for which the SCT Barrel is set to the nominal voltage of 150 V are considered. Also in this case the analysis is performed within the `ATHENA` framework using release 15. The main release used for collision data analysis is 15.6.4.

3.4.1 Track selection

A detailed study on the tracks feeding into the input sample used for the Lorentz angle determination has been performed, see [40]. Following the the Minimum Bias analysis on first collision data, the following preliminary track selection has been adopted:

- $|d_0| < 10\,\text{mm}$,
- $p_T > 400\,\text{MeV}$,
- at least seven SCT Barrel hits,
- at least two Pixel hits.

This has then been optimised in the following way. First, a detailed study on the tracks that most contribute to the minimum as well as to the slopes of the profile distributions is performed. The contributions of negative and positive charges are separated as shown in Figure 3.5 for all four Barrel layers. The contribution of negative tracks is shown in red and that of positive tracks in black.

As Figure 3.5 shows, the positive incidence angles are dominated by negative tracks, while the negative angles are dominated by positive tracks. The intersection of the two types of tracks happens at an incidence angle of about -10 degrees, so the minimum of the cluster width (that is the Lorentz angle by definition and it is around -4 degrees) receives contributions only from negative tracks. Moreover the positive tracks contributing to incidence angles smaller than -10 degrees have slightly larger cluster widths with respect to the negative ones. The fit to the cluster width distribution is slightly worsened by the presence of these positive tracks around the minimum, even if they are statistically less significant. In conclusion, negative-only tracks provide a clear minimum in the cluster width, with better defined slopes, giving the best sample for a reliable fit using the function in Equation 3.7.

To further optimise the selection, the transverse impact parameter (d_0) is studied, see [40]. The optimal selection is found to be $|d_0| < 1\,\text{mm}$, this allows the selection of a sample of tracks generated very close to the IP.

As for the impact parameter, a p_T scan has also been performed by plotting the cluster width vs the incidence angle for various p_T bins, applying no other cuts, see [40]. The result of this study shows that tracks with a $p_T < 500\,\text{MeV}$ never have an incidence angle in the minimum region. This motivates the choice of requiring a minimum track p_T of 500 MeV.

To summarise, the track selection has been finalised as follows:

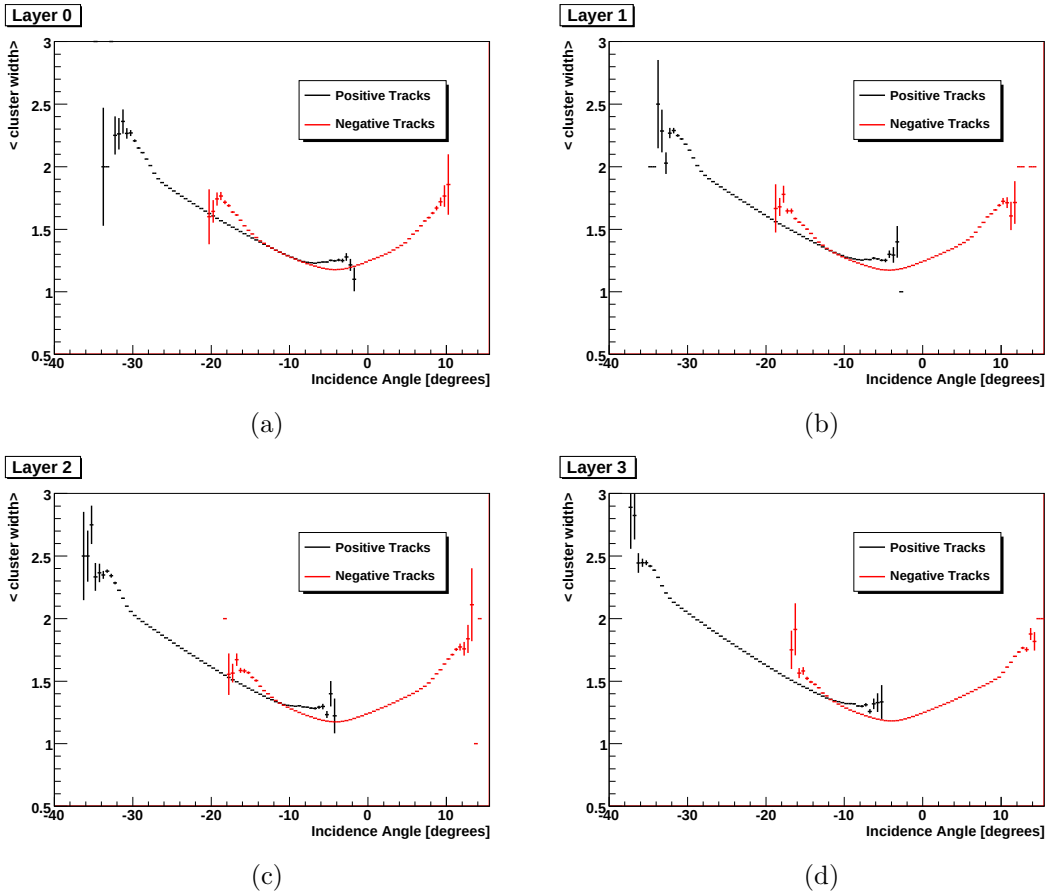

Figure 3.5: *Positive and negative tracks study. Cluster width as function of the local incidence angle in the four SCT layers. Layer 0 shown in (a), Layer 1 in (b), Layer 2 in (c) and Layer 3 in (d). Red points represent the contribution from negative tracks, while black points show the contribution of positive tracks.*

- charge $Q < 0$,
- $|d_0| < 1\,\text{mm}$,
- $p_T > 500\,\text{MeV}$,
- at least seven hits in the SCT Barrel,
- at least two Pixel hits.

This selection is applied in all collision studies presented, and the fit is performed only on negatively charged tracks.

Figure 3.6 shows the Lorentz angle extracted for all layers of the SCT Barrel and for two different collision runs (datasets 162882 and 165591). A comparison is also shown to the MC sample (Minimum Bias dataset number 105001). The magenta band represents the model prediction discussed in Section 3.2.1. The Lorentz angle

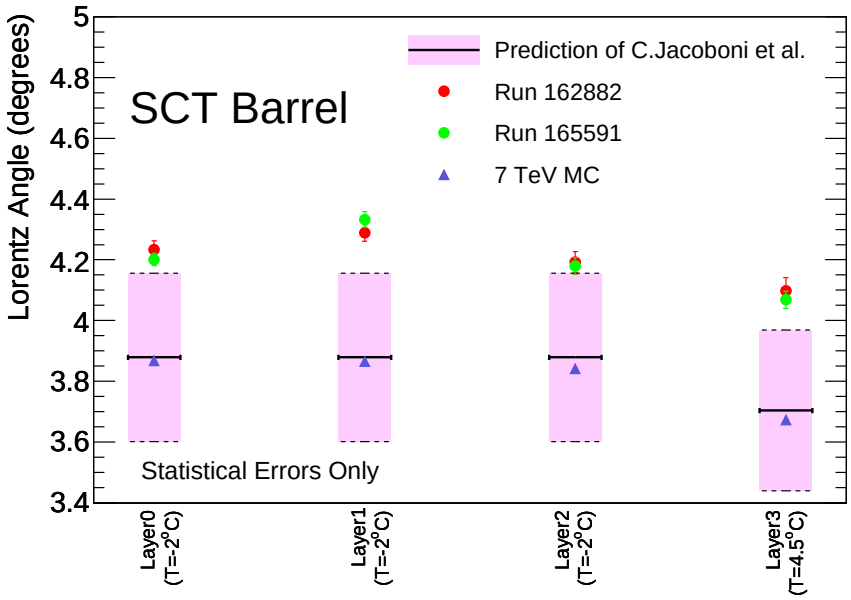

Figure 3.6: *Lorentz angle measured for two different collision runs. Comparison with MC simulation is also shown.*

value measured for each layer is significantly above the model prediction. Note that in this figure as well as in others that are shown below, the Lorentz angle is shown to be positive. This is a convention adopted throughout. However, as can be seen from the profile distributions (i.e. Figure 3.5), the incidence angle corresponding to the minimum is negative.

3.4.2 Fitting range optimisation

A fit range study using cosmic-ray data has been performed during the 2009 data taking and documented in [39]. The optimal range to be used when fitting the distribution of average cluster width as function of incidence angle was found to be $\pm 12.5°$ around the angle at which the distribution has its minimum.

For the 7 TeV collision data analysis, a specific track selection is applied, as detailed in Section 3.4.1. The main novelty is the use of only negatively charged tracks and this implies a different range of incidence angle values allowed to tracks passing this new selection. Based on the geometry and the position of the modules of the SCT in the Barrel, all selected tracks can pass through the module wafer with angles varying from about -20 to about $+10$ degrees. Therefore a new fit range optimisation study is needed and the ranges considered for this new study must be asymmetric around the minimum, unlike the case of cosmic-ray data.

The lower bound of the fitting range is allowed to vary from $-10°$ to $-6°$ in

steps of 1° and the upper bound is chosen to vary from −2° up to +8° in steps of 2°. This gives a total of 30 different fit ranges to scan. The optimisation has been performed repeating the fit for the Lorentz angle extraction in these 30 different ranges, for each of the four SCT Barrel layers, using run 159224 taken on July 18th, 2010. The results for Layer 0 are presented here; all the other layers give consistent results as can be seen in [40].

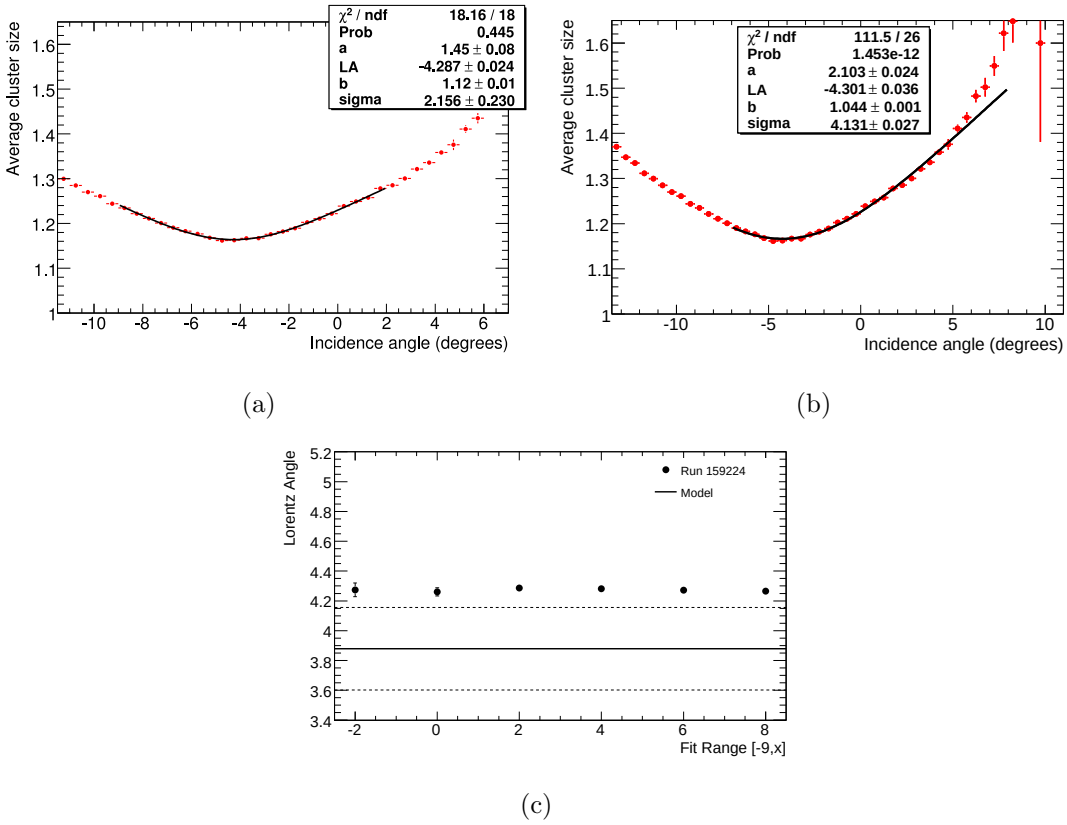

Figure 3.7: *Plots from the fitting range optimisation for Layer 0 on collision data. (a) Example of the distribution of average cluster width as a function of incidence angle. The fitting function is shown for a fitting range of [-9°, +2°]. This is the chosen fit range to be used in the study of the Lorentz angle in 7 TeV collision data. (b) Another example of the distribution to be fitted in order to extract the Lorentz angle. The fit is shown with the fitting range [-7°, +8°]. (c) Lorentz angle value as a function of the tested fit ranges with a lower bound of −9° and variable upper bound x.*

Figure 3.7 (c) shows the Lorentz angle values extracted from fitting in the range $[-9°, x]$, where $x = -2°, 0°, +2°, +4°, +6°, +8°$, All of the scans show very consistent values of the Lorentz angle at about −4.28°, with only up to 2% variation for ranges with a large upper bound. The robustness of the fit in the region around the minimum is due to the large number of tracks entering each of the distributions to be fitted and therefore the small statistical uncertainty. Some examples of fits

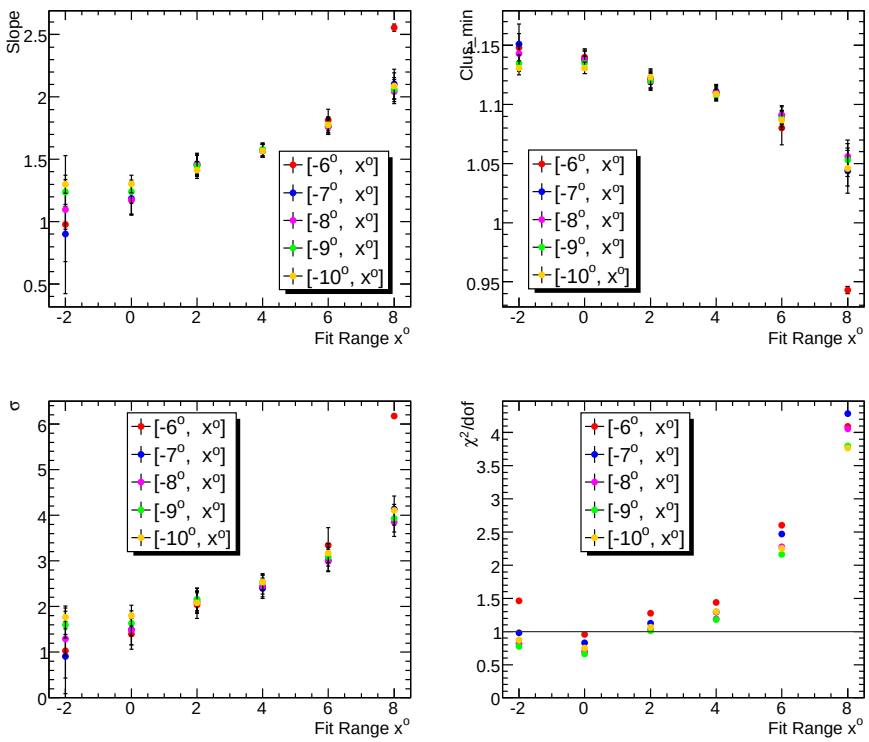

Figure 3.8: *The three parameters of the fit function (not including the Lorentz angle) and the fit χ^2/DoF as a function of the fit ranges tested.*

to distributions of average cluster width as function of incidence angle for some of the fit ranges used in this study are shown in Figures 3.7 (a) and (b). In Figure 3.7 (a) the fit gives good description of the distribution, whereas in Figure 3.7 (b) the upper bound of the range is too large for the fit to give reliable results.

In order to choose the optimal fit range to be used to monitor the Lorentz angle in different collision runs and study the robustness of the fit, the other three parameters and the χ^2/DoF of the fit were also studied in the optimisation. Figure 3.8 shows the variation of these parameters as function of the incidence angle range used to perform the fit. All these parameters (i.e. the fitting function parameters except the Lorentz angle) seem to be very sensitive to the fit range used: this indicates that the function in Equation 3.7 used is not the optimal one to describe these distributions away from the minimum.

In any case, since the study shows a very stable Lorentz angle value extracted from fitting with this non-optimal function, the choice of an optimal fit range is made by looking at the χ^2/DoF distribution. The fit ranges with upper bounds $-2°$ and $0°$ show a χ^2/DoF very close to one, but these are excluded because the upper limits are very close to the minimum of the distribution to be fitted. This could

result in the fit being less robust as one of the two slopes has fewer points to take into account. Therefore the optimal fit range is chosen to be the one which gives the χ^2/DoF closest to one, but does not have either edges close to the minimum. This results in a chosen range of $[-9°, +2°]$. This fit range has been used in all Lorentz angle measurements in 7 TeV collision studies.

The same study was performed on a Minimum Bias simulated event sample (dataset 105001), in order to optimise the fit range to be used for extracting the Lorentz angle value on MC data. A different fitting range is necessary in simulated event samples, since the Lorentz angle value is lower in simulation than in data as shown in Figure 3.6. As for collision data, the same set of fit ranges has been tested and the function parameters together with the fit χ^2/DoF have been checked for all the ranges. The details of the simulated event sample fitting range optimisation can be found in [40]. The optimal fit range to use in simulated event sample studies for the Lorentz angle determination is chosen to be $[-8°, 0°]$.

The conclusion from this study is that, both on collision and MC simulation, the fitting function is stable and robust to determine the value of the Lorentz angle. In fact, the latter value remains unchanged when changing fit range. Being an effective modelling, the function fails to accurately describe the slopes of the distribution of the average cluster width for values of the incidence angle away from the minimum. This implies an enhanced dependence of the fit parameters from the chosen fitting range. One of the effects is that large fit ranges are disfavoured as the linear model of the slopes is particularly weak. Therefore, the minimum χ^2/DoF (in both collision data and MC simulation) is given by ranges with bounds quite close to the minimum of the distribution, in order to minimise the contribution from the slopes. Nevertheless, the function in Equation 3.7 is a very effective and powerful tool to reliably extract the Lorentz angle, as this study proves when looking at the stability of the results in the Lorentz angle values.

To summarise, the fit range used for the Lorentz angle analysis is $[-9°, +2°]$ for 7 TeV collision data and $[-8°, 0°]$ for simulated event samples.

3.4.3 Lorentz angle measurement in different regions of the module

Given the large number of tracks hitting the SCT modules in 7 TeV collisions, a more detailed study of the distribution of the average cluster width as a function of the incidence angle is possible.

A study has been performed by dividing each module of the SCT Barrel into 12 equal rectangular regions and determining the Lorentz angle in each region sep-

arately. Figure 3.9 shows how the modules are divided into regions with respect to their local coordinates *LocX* and *LocY*. A picture of a Barrel module of the SCT is shown in Figure 2.5. A space of 0.5 mm around each region is left to avoid possible overlaps.

Several 2010 collision runs are considered. The results from run 153656 taken on April 23rd, 2010 are reported here. The default track selection (described in Section 3.4.1) is applied. However, the distribution of average cluster width as a function of local incidence angle is studied for all tracks, negative and positive. To extract the Lorentz angle, the fit is performed considering negative tracks only.

Figure 3.10 shows a comparison of the distributions in the twelve regions of Layer 1 (similar plots for the other layers show the same results). Each plot groups together four regions of same *LocX*. The distributions are very similar in each case, proving that there is no difference in the kinematics of track selected when scanning across the module along the longitudinal direction. A similar comparison is done by grouping three *LocX* regions at constant *LocY*. This is shown in Figure 3.11 for collision data.

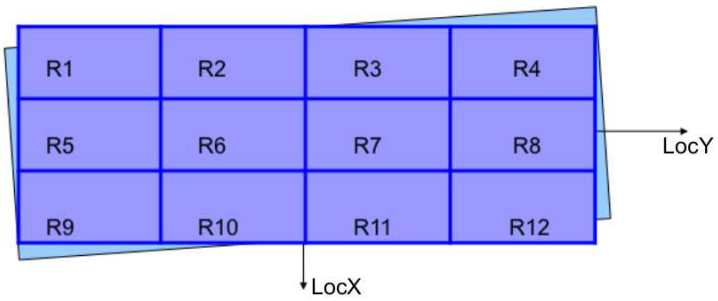

Figure 3.9: *Diagram of the region division along the LocX and LocY coordinates.*

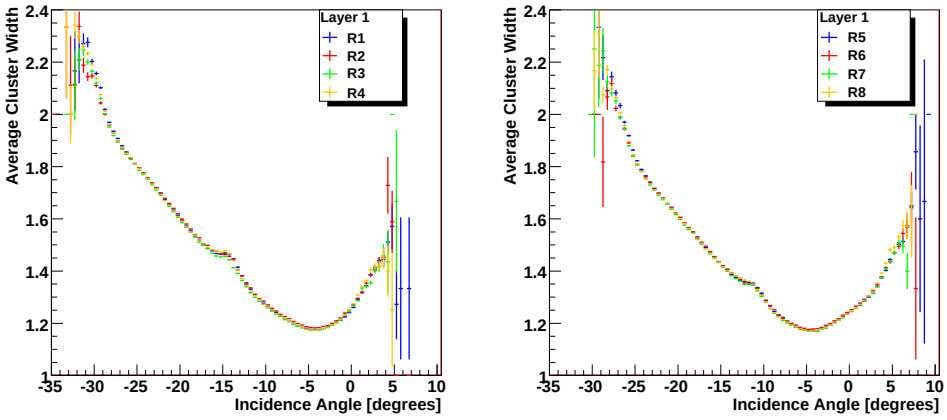

(a)

(b)

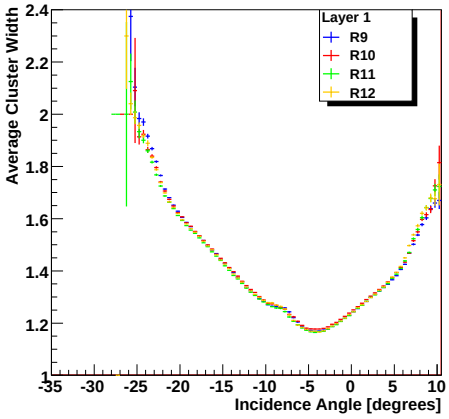

(c)

Figure 3.10: *Layer 1: comparison between the twelve regions of the module. Each plot refers to a different region in LocX. Within the same plot, the contribution of four regions in LocY are plotted. (a) Regions 1, 2, 3 and 4. (b) Regions 5, 6, 7 and 8. (c) Regions 9, 10, 11 and 12.*

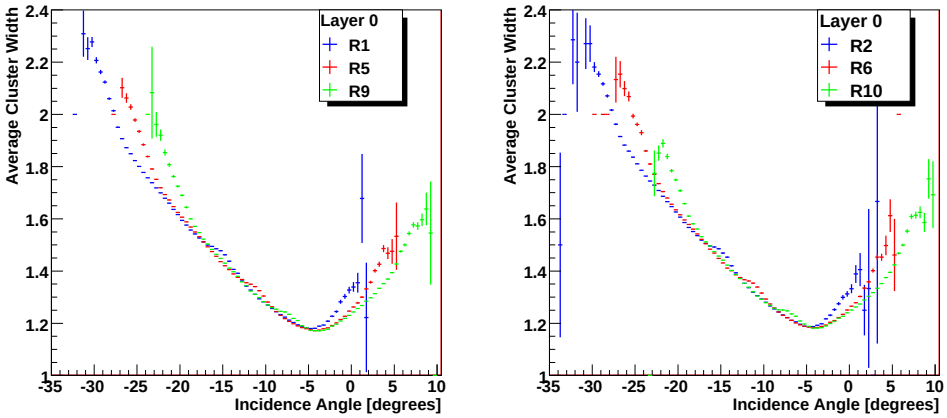

(a)

(b)

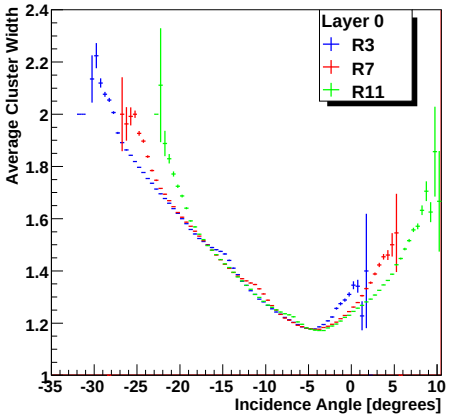

(c)

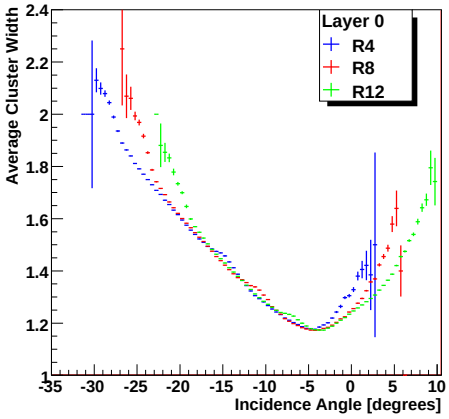

(d)

Figure 3.11: *Layer 0: the twelve regions of the modules are compared. In each plot, the same region in LocY is considered. Within the same plot three different LocX regions are plotted together for comparison. (a) Regions 1, 5 and 9. (b) Regions 2, 6 and 10. (c) Regions 3, 7 and 11. (d) Regions 4, 8 and 12.*

When studying tracks hitting different regions of the module, the following features are observed:

- a small local peak is present in each of the distributions,
- the peaks are at different incidence angles when scanning across the *LocX* coordinate,
- the slope and range of the distributions change when scanning across the *LocX* coordinate.

The above features do not appear when plotting the distribution of the average cluster width as a function of the local incidence angle for the whole module, as this corresponds to taking an average of the different kinematic contributions.

The features described above are also present in MC simulation. See [40] for the study performed on MC samples.

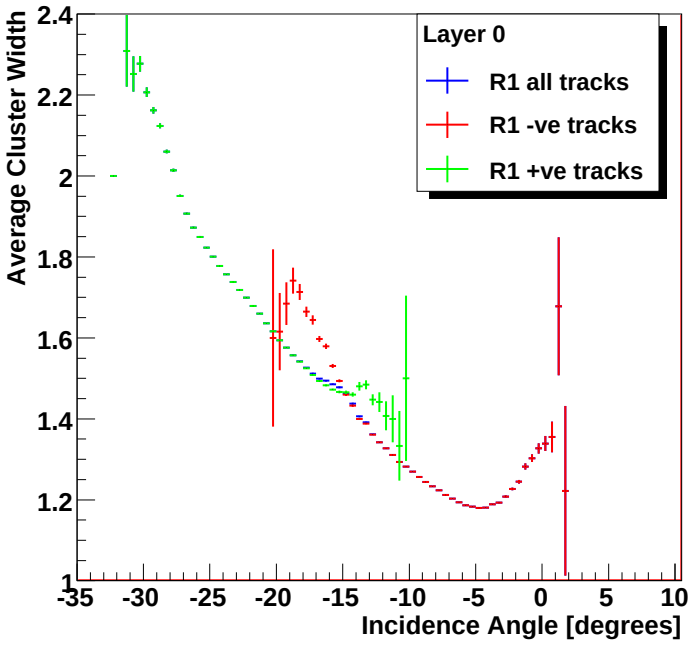

Figure 3.12: *Example of how negative and positive tracks contribute to the distribution generating the peak. Region 1 of modules of Layer 0 is shown.*

Figure 3.12 shows the origin of the peak. It is generated at the incidence angle at which the average cluster width from positive tracks intersects the contribution from negative tracks. This particular region is populated by high momentum tracks. They cause an increase in dE/dx, and consequently an increase of deposited charge on the module. As a result, an increase in the average cluster width is observed.

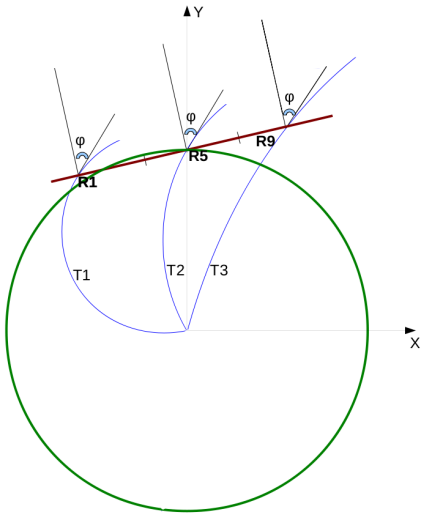

(a)

Figure 3.13: *Diagram (not in scale) showing a module in the SCT Barrel and three positive tracks traversing it.*

The peaks occur at three different incidence angles in the three *LocX* regions. This is due to the kinematics of the tracks traversing the SCT Barrel module as well as to the geometry and tilt angle of the module itself. A derivation of the correlation between the momentum of the tracks, their local incidence angle and the *LocX* coordinate is shown in Section 3.4.4.

Furthermore the origin of the different slopes and the different ranges of the cluster width distributions is explained. Considering tracks coming from the IP, the three regions in *LocX* are correlated to different ranges of track momentum. By considering all tracks passing through the module with the same local incidence angle, but in increasing values of *LocX*, the tracks must have increasing p_T, if they are positive tracks, as shown in Figure 3.13 or decreasing p_T, in case of negative tracks. For positive tracks and a given incidence angle ϕ, the p_T increases going from region R1 to region R5 and finally to region R9. Therefore an increase of deposited charge on the module is observed, causing a larger cluster width. In case of negative tracks the reverse is true. This effect is the reason why the slopes of the distributions on Figure 3.15 are different in the different *LocX* regions. There is of course an overlap in p_T, and therefore, for some ranges of incidence angle, the difference between the *LocX* regions does not show. This can be seen, for example, in Figure 3.11 (c) at around $-17°$ comparing regions R7 and R11. As a consequence of the different kinematic regions in which the tracks are selected, also the range of allowed incidence angle varies in the three *LocX* regions (any *LocY*).

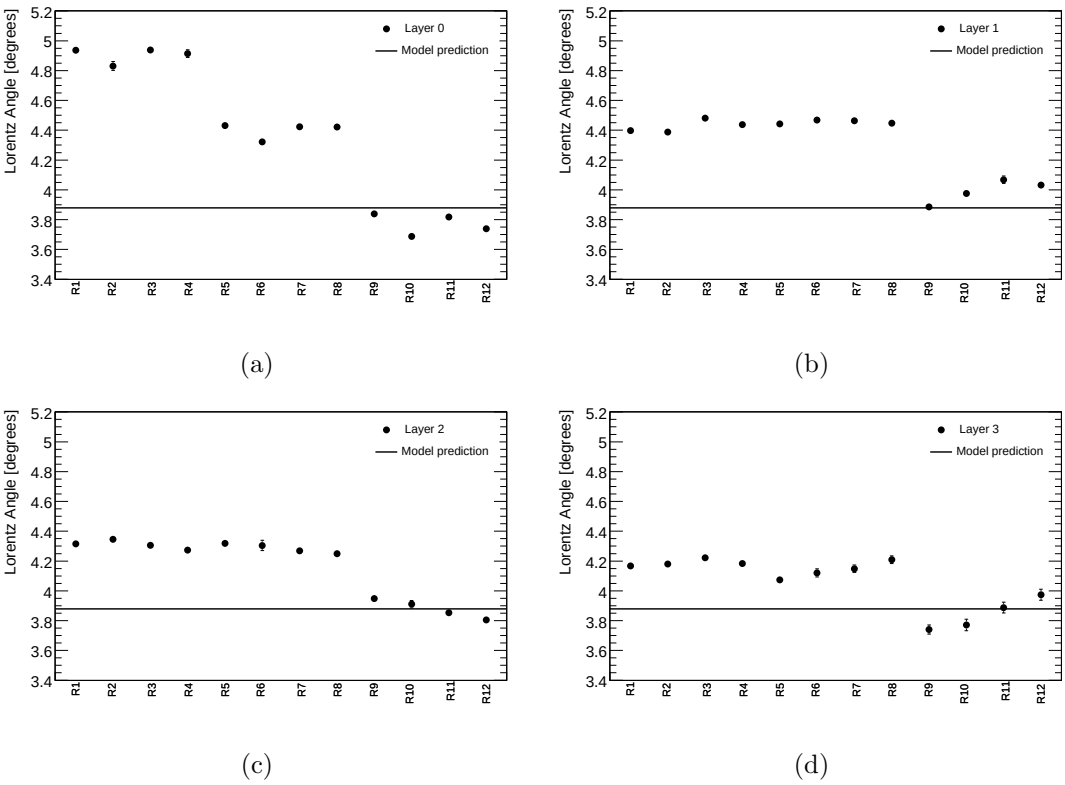

Figure 3.14: *Lorentz angle measured in collision data for each of the twelve regions of the module. Each plot refers to a different layer of the Barrel of the SCT.*

The last part of the study involved determining the Lorentz angle value in each of the twelve regions. Figure 3.14 shows the results of the fits, for collision data (only negative tracks were considered) in all four layers of the Barrel. See [40] for the comparison with simulated event samples.

As already seen in Figure 3.10, the minimum of the distribution does not change considerably when scanning along the module in *LocY*. A zoom of the distributions for Layer 0 comparing two regions of same *LocX*is shown in Figure 3.15 (a). Therefore also the fit gives comparable values for the Lorentz angle in these regions. Conversely, the results for different *LocX*regions show a discrepancy: this is shown in the zoomed-in distributions in Figure 3.15 (b) where it can be seen that the minimum occurs indeed at different incidence angles.

The Lorentz angle value is found to be larger for regions of smaller *LocX*: the values extracted from the fit to the cluster width distribution in the various regions are shown in Figure 3.14 for collision data. The value of the Lorentz angle changes with the layer number, decreasing when going from the inner to the outer part of the Barrel. Although the values are different and closer to the model prediction, a similar trend can be also seen in MC samples [40].

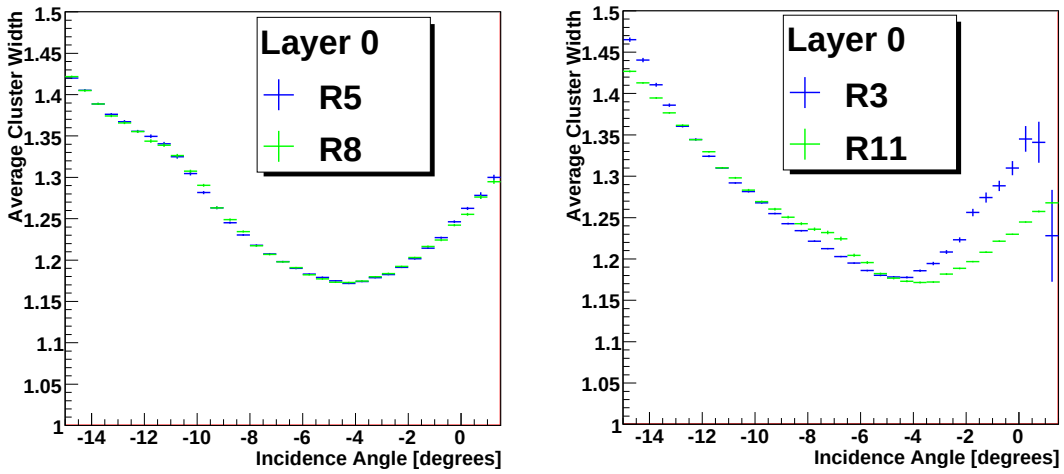

(a) (b)

Figure 3.15: *Distributions of average cluster width as function of incidence angle: (a) Comparison between region 5 and region 8 which scan the same LocY region, but different LocX regions. (b) Comparison between region 3 and region 11 which scan the the same LocX region, but different LocY regions.*

To summarise, it is found that considering tracks coming from the IP builds a correlation between their momentum, the *LocX* coordinate and the range of incidence angles at which the tracks enter the module. An explanation of the features found in the region dependent distributions is given. The minima of the distributions also change in some cases significantly. As a result, the Lorentz angle extracted from the fit has different values in each region. This aspect has not been fully explained. Collision and simulation data show similar results in this aspect of the study.

3.4.4 Kinematic correlation of tracks coming from the IP

A simple correlation is obtained between the local incidence angle of a track, its momentum and the local coordinates on the module of the SCT Barrel.

In what follows it is assumed that the following quantities are known and constant:

- $R = 299\,\text{mm}$: radius of Layer 0,
- $\delta = 11°$: tilt angle of the module with respect to the tangent to the Barrel,
- $B = 2\,\text{T}$: magnetic field.

For each given track originated from the IP, at the centre of the Barrel, the following variables are considered:

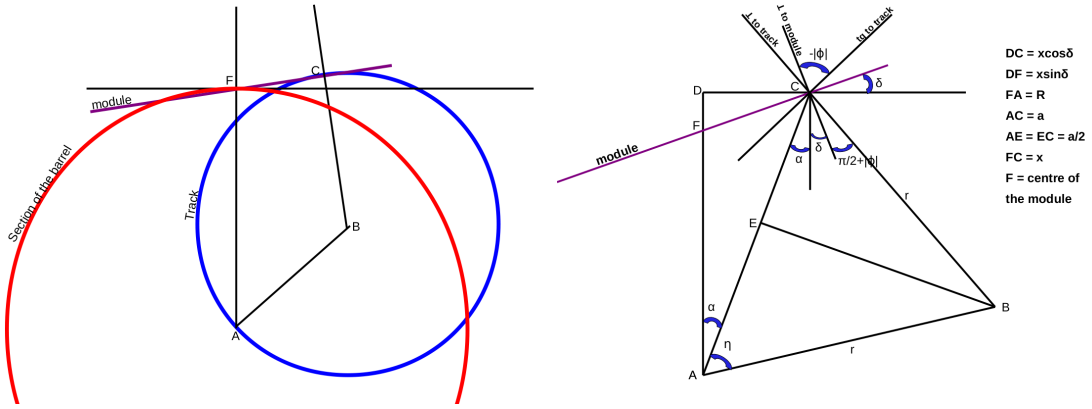

(a) (b)

Figure 3.16: *(a) Track generated in the centre of the Barrel and traversing one of the modules of the SCT Barrel. (b) Better view of the angles and geometry between the module and the track hitting on it.*

- $x = LocX$: local x coordinate on the module,
- Φ: local incidence angle of the track on the module,
- p_T: momentum of the track,
- r: radius of the circular trajectory of the track.

Figure 3.16 (a) shows an approximate and not to scale representation of one of the layers of the Barrel with a track (positive in this example) going through the tilted module. In Figure 3.16 (b) triangle ABC is isosceles, because the two sides labelled r are equal to the radius of the circular trajectory of the track. The relation between the two equal angles of the triangle is given by:

$$\eta = \alpha + \delta + \frac{\pi}{2} + |\Phi|. \tag{3.8}$$

Also, considering the right-angled triangle BCE, η and r are related by the relation:

$$\frac{a}{2} = r\cos\eta. \tag{3.9}$$

Considering now the right-angled triangle ACD, the following two relations can be written:

$$a = \sqrt{DA^2 + DC^2} = \sqrt{(R + x\sin\delta)^2 + x^2(\cos\delta)^2} \tag{3.10}$$

and

$$\frac{DC}{DA} = \tan\alpha = \frac{x\cos\delta}{x\sin\delta + R}. \tag{3.11}$$

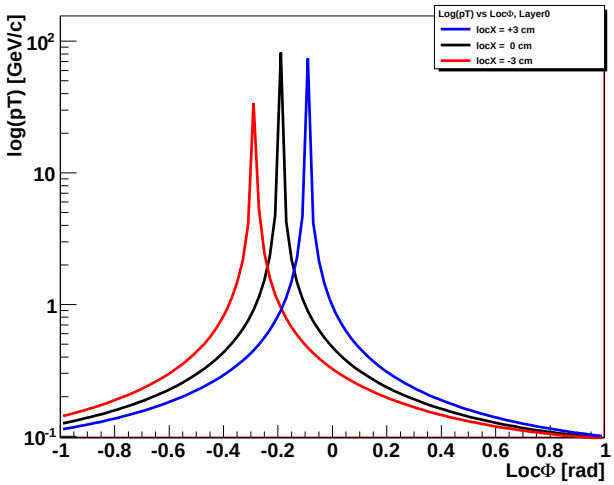

Figure 3.17: *Distribution of p_T as a function of incidence angle for three different LocX coordinates for Layer 0.*

Starting from Equation 3.9 and using Equations 3.8, 3.10 and 3.11, the following equation in three unknowns (x, δ and r) can be derived:

$$\sqrt{R^2 + x^2 + 2Rx\sin\delta} = 2r\cos\left(\arctan\left(\frac{x\cos\delta}{x\sin\delta + R}\right) + \delta + \frac{\pi}{2} + |\Phi|\right). \quad (3.12)$$

Finally, considering that the transverse momentum p_T of the track and the radius r of its circular trajectory are related by:

$$p_T = 0.3rB, \quad (3.13)$$

with p_T given in GeV, r in metres and B in Tesla. Equation 3.12 can also be written as:

$$\sqrt{R^2 + x^2 + 2Rx\sin\delta} = \frac{2p_T}{0.3B}\cos\left(\arctan\left(\frac{x\cos\delta}{x\sin\delta + R}\right) + \delta + \frac{\pi}{2} + |\Phi|\right). \quad (3.14)$$

This equation relates the p_T, *LocX* and incidence angle Φ of the incident track. Figure 3.17 shows the distributions of p_T (in logarithmic scale) as a function of the local incidence angle Φ for three chosen *LocX* on the module. In all three distributions a peak can be seen. In degrees, the peaks occur at about -17 degrees ($LocX = -3\,\text{cm}$), -11 degrees ($LocX = 0\,\text{cm}$) and -6 degrees ($LocX = +3\,\text{cm}$). Considering that this is only an approximated model of the geometry of the SCT Barrel, the three values estimated above are in good agreement with the position of

the peaks seen in data distributions of Figure 3.11 (a).

3.4.5 Results and conclusion

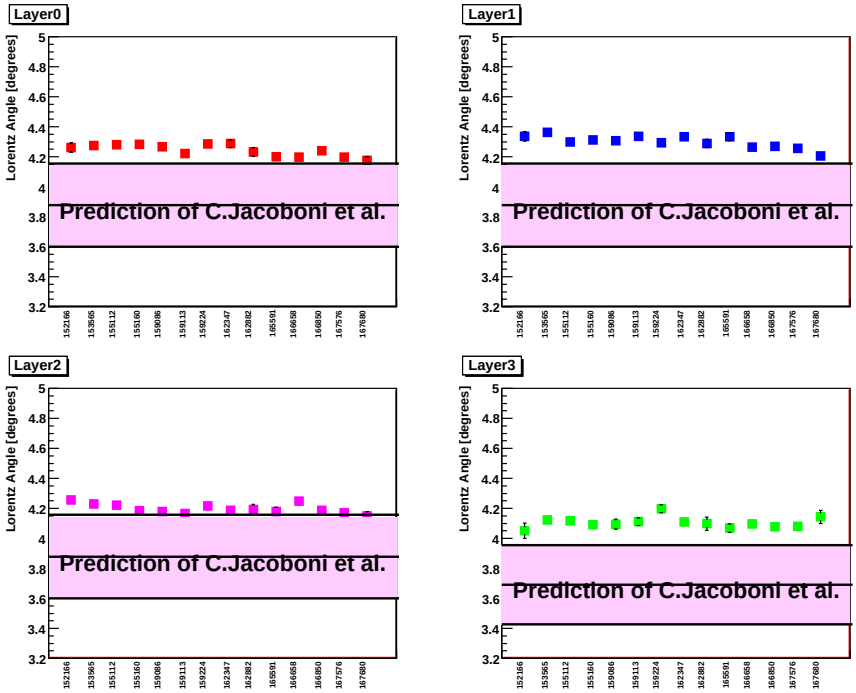

Figure 3.18: *Lorentz angle measured in each of the 2010 collision data runs considered. From left to right and from top to bottom: Lorentz angle value as function of the run number in layer 0 to 4. The band represents the model prediction with its uncertainty as discussed in Section 3.2.1. The error on the measured angles is only statistical.*

In Figure 3.18, the extracted Lorentz angle values are shown for all the collision runs analysed during the 2010 data taking period, and for each of the SCT layers. The measured values are compared with the model prediction discussed in

Run 167576	Lorentz angle value (degrees)
Layer 0	4.197 ± 0.018
Layer 1	4.256 ± 0.018
Layer 2	4.172 ± 0.021
Layer 3	4.079 ± 0.024

Table 3.3: *The Lorentz angle values for all the layers in the collision run 167576, with statistical errors only. These values correspond to the points in Figure 3.19 (b).*

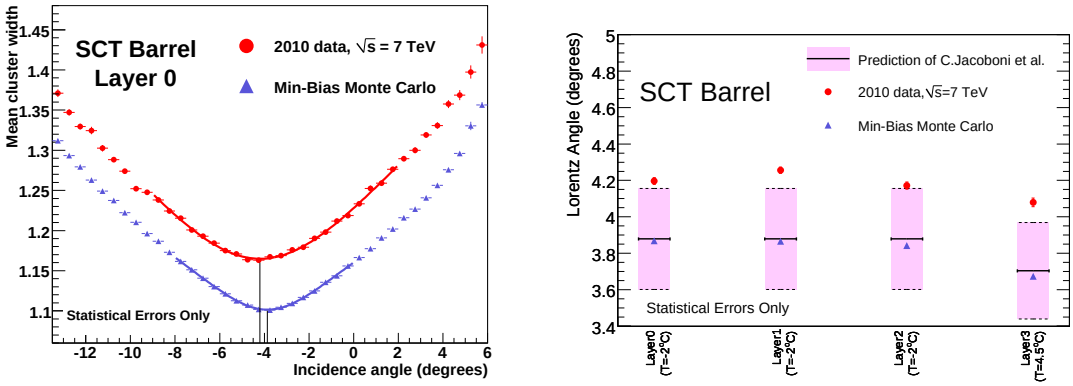

(a) (b)

Figure 3.19: *(a) Example of a fitted profile of the average cluster width vs the incidence angle on both collision and simulation data. (b) The Lorentz angle values for all the layers and both collision and simulation data (statistical errors only).*

Section 3.2.1. The value of the Lorentz angle shows a discrepancy with respect to the model expected value.

The extraction procedure has been checked on simulated event samples [40], using the same track selection and same fitting function and a good agreement with the model has been found. This is anticipated as the simulation implements the same model. It is however a test of the fitting method that proves to be unbiased.

Figure 3.19 shows the comparisons between one collision run and the MC samples. In Figure 3.19 (a) a fitted profile on both collision and simulation is shown for Layer 0. It is clearly visible that the minima of the two distributions do not occur at the same local incidence angle[4]. This difference is best seen in plot (b) where the Lorentz angle values for all the layers and for both collision data and MC simulation are shown. Table 3.3 shows the values corresponding to collision data.

The analysis on the 2010 collision data shows a discrepancy with respect to the model expected value (and to the simulation). No conclusive explanation of this difference has been found so far. More studies are ongoing within the ATLAS SCT group.

[4]It is also clear that the minimum cluster width is different in data and MC simulation. This study has not been investigated further but it is reported in [39]

Chapter 4

Trigger Efficiency

In this chapter the EF_2mu4_DiMu trigger efficiency is determined using 2010 data. This di-muon trigger requires two opposite sign muons of 4 GeV minimum p_T, minimum invariant mass of 0.5 GeV and maximum vertex chi^2 match of 20. The efficiency is applied to the di-muon Drell-Yan analysis presented in the following chapters.

A variety of low threshold single muon triggers were available unprescaled for early periods of data taking in 2010. Towards the end of September 2010 these started to be heavily prescaled and were turned off when the luminosity increased considerably (about one month later). Only the topological DiMuon triggers, i.e. EF_2mu4_DiMu designed for the B-physics group were left to be used for physics analysis. These ran unprescaled in 2010. Some of them were left unprescaled also in part of the 2011 data taking period.

The efficiency of low threshold single muon trigger EF_mu4 could be estimated from data using the standard Tag and Probe method using a sample of J/ψ events only for the early periods in 2010. However not enough events were collected to have robust results. An alternative method to measure the efficiency has been developed and the results compared to the Tag and Probe method.

The reconstructed muons considered throughout the chapter are the ones selected by the Muid algorithm. The efficiency is measured on data and comparison with MC samples is not possible in most cases. This is because of a technical problem with the setup of the trigger algorithm in the MC simulations in 2010.

4.1 Triggers used for efficiency study

An extensive description of the ATLAS trigger system and muon triggers has been given in Sections 2.2.3 - 2.2.5. In this section a variety of triggers are discussed and studied. These can be divided into two different categories i.e. *TrigDiMuon* and *Topological* triggers, depending on the algorithm used to define them. The *TrigDiMuon* triggers are seeded by a single L1 muon RoI. Two muons are then looked for by extrapolating Inner Detector (ID) tracks at the HLT. The extrapolation can be done inside an enlarged RoI around the L1 muon RoI or in the whole detector (Full Scan). The second case is not dealt with here. The *Topological* triggers are seeded by two L1 muon RoIs. Each muon is then confirmed at the HLT. Both of the above categories apply some constraints in order to reduce the rate and at the same time keep interesting events (J/ψ, Υ, Drell-Yan). The requirements imposed on the triggers used in this study may concern :

- the invariant mass of the di-muon pair, $M_{\mu\mu}$,
- the opposite sign requirement of the two muons (OS), in di-muon triggers,
- the χ^2 constraint on the di-muon vertex fit,
- the spatial separation between the trigger objects i.e. $\Delta\eta$(`mu4`,`Trk`), $\Delta\phi$(`mu4`,`Trk`),

where `mu4` is a muon trigger object with minimum p_T of 4 GeV and `Trk` is a track trigger object with minimum p_T of 4 GeV.

Table 4.1 shows a list of the EF triggers used for the efficiency determination. It also lists the L1 items which seed them and a summary of HLT requirements applied to each one. The `L1_MU0` trigger is a two station RPC coincidence and therefore has no momentum measurement. This trigger is therefore sensitive to muons over a large range of momenta. The `L1_2MU0` requires two muons instead of one.

During 2010 the trigger menu evolved with the increasing instantaneous luminosity. Due to the rapidly changing conditions in periods A to D and the low luminosity collected these periods are neglected in this study. The luminosity per period is calculated using the Luminosity Calculator [47] available with the most updated GRL given in Section 4.2.

Table 4.2 lists the detail of some of the low threshold single and di-muon triggers during periods E to I in 2010. For each trigger and each period the prescale applied is given as well as the total integrated luminosity. As already mentioned in the introduction, single muon triggers ran unprescaled only for the first periods of data taking, after period F they were heavily prescaled or turned off. Also the di-muon

Trigger item	Seed	HLT Requirements
EF_2mu4_DiMu	L1_2MU0	two muon trigger objects with $p_T > 4\,\text{GeV}$, $M_{\mu\mu} > 0.5\,\text{GeV}$, OS, vertex χ^2 match < 20
EF_2mu4_DiMu_noVtx_noOS	L1_2MU0	two muon trigger objects with $p_T > 4\,\text{GeV}$, $M_{\mu\mu} > 0.5\,\text{GeV}$
EF_mu4_Trk_Jpsi	L1_MU0	one muon trigger object with $p_T > 4\,\text{GeV}$, one track trigger object with $p_T > 4\,\text{GeV}$, $2.85\,\text{GeV} < M_{\mu\mu} < 3.35\,\text{GeV}$, $\Delta\eta$(mu4,Trk) < 0.75, $\Delta\phi$(mu4,Trk) < 0.75, OS
EF_mu4_IDTrkNoCut	L1_MU0	one muon trigger object with no minimum p_T requirement, Muon Spectrometer (MS) only muons required for event to be triggered. No requirements on the Inner Detector track

Table 4.1: *Table of muon triggers used in the efficiency determination, with information on the L1 items which seed them and the HLT requirements applied on each trigger.*

EF_2mu4 was prescaled and therefore did not collect the full luminosity available. The lowest threshold di-muon trigger which ran unprescaled for the whole 2010 data taking period was the topological trigger EF_2mu4_DiMu. This succeeded in keeping a low rate because of the topological requirements set on the muons. The monitoring triggers are also listed in Table 4.2. These were prescaled but collected enough luminosity for the EF_2mu4_DiMu trigger efficiency to be determined using the method presented here.

		EF_mu4	EF_2mu4	EF_2mu4_DiMu	EF_2mu4_DiMu_noVtx_noOS	EF_mu4_Trk_Jpsi	EF_mu4_IDTrkNoCut
period E	<prescale>	1.004	1.00	1.00	1.00	1.00	2.581
	$\int \mathcal{L}\ /pb^{-1}$	0.968	0.972	0.972	0.972	0.972	0.376
period F	<prescale>	21.79	1.00	1.00	1.00	1.00	157.811
	$\int \mathcal{L}\ /pb^{-1}$	0.080	1.736	1.736	1.736	1.736	0.011
period G	<prescale>	61.49	2.76	1.00	1.017	1.00	549.241
	$\int \mathcal{L}\ /pb^{-1}$	0.900	2.001	5.522	5.429	5.522	0.010
period H	<prescale>	1134.88	45.09	1.002	1.872	1.002	4527.31
	$\int \mathcal{L}\ /pb^{-1}$	0.006	0.155	6.984	3.737	6.984	0.002
period I	<prescale>	trigger OFF	71.82	1.00	4.363	1.236	8998.467
	$\int \mathcal{L}\ /pb^{-1}$	0.0	0.28	20.721	4.749	16.769	0.002

Table 4.2: *Prescale applied and luminosity collected by single muon and di-muon triggers with a 4 GeV threshold. Information is given by period, from period E to period I in 2010.*

4.2 Software and datasets

The study is performed on Analysis Orientated Data (AOD) within the `ATHENA` framework using software release 16.6.7.3. The sample of events studied in collision data is the one available in the GRL `data10_7TeV.periodAllYear_DetStatus-v21-pro05_CoolRunQuery-00-04-00_WZjets_allchannels.xml` in order to discard luminosity blocks with detector problems. The MC samples used for this study are listed in Table 4.3.

Generator	Process	M [GeV]	Filters	Dataset	σ_{eff} [nb]	GenEvt	$\mathcal{L}$ [fb^{-1}]
Pythia	$J/\psi \rightarrow \mu\mu$		$2 \times p_T > 4\,\text{GeV}$ $\lvert\eta\rvert < 2.5$	108536	23.66	5M	0.21
Pythia	$Z/\gamma* \rightarrow \mu\mu$	8-15	$2 \times p_T > 3\,\text{GeV}$ $2 \times \lvert\eta\rvert < 2.7$	113700	1.044	1M	0.96
Pythia	$Z/\gamma* \rightarrow \mu\mu$	15-60	$2 \times p_T > 3\,\text{GeV}$ $2 \times \lvert\eta\rvert < 2.7$	113701	0.512	1M	1.95
Pythia	$Z/\gamma* \rightarrow \mu\mu$	> 60	-	106047	0.99	5M	5.05
PythiaB	$c\bar{c} \rightarrow \mu\mu$		$2 \times p_T > 4\,\text{GeV}$ $\lvert\eta\rvert < 2.5$	108487	16.0	1M	0.06
PythiaB	$b\bar{b} \rightarrow \mu\mu$		$2 \times p_T > 4\,\text{GeV}$ $\lvert\eta\rvert < 2.5$	108488	89.0	2M	0.02

Table 4.3: *Table of MC samples used in the trigger efficiency study. For each sample the generator is specified, together with the corresponding mass range, the effective cross section σ_{eff}, the details of the lepton filters applied, the number of events generated, and the total effective luminosity of the sample.*

4.3 Tag and Probe Method

The Tag and Probe method is a data driven technique used to measure trigger and offline reconstruction efficiency. This method is particularly useful in the analysis of two-objects final states. For low p_T threshold trigger efficiency study the basic idea of the method is to identify a sample of J/ψ events which contain at least one muon trigger object reconstructed in both the inner detector and the muon spectrometer. This is known as the tag. Within this sample a probe is defined as a reconstructed combined muon (or just an inner detector track) with looser requirements and it is not required to have triggered the event. Tag and probe are then required to come from the decay of a well know resonance by restricting their invariant mass to be in a narrow range around the resonance mass. The efficiency is defined as the ratio between the number of probes which are matched to a trigger object relative to the

item for which the efficiency has to be determined, and the number of probes in the sample of events selected.

This method can be used to determine the trigger efficiency for the three different levels of the trigger, L1, L2 and EF, only if the single muon trigger collects enough events for the study to be carried out. This is not the case with the trigger menu setup in 2010 for the `EF_mu4` trigger, as it was prescaled after period E and then turned off. The `EF_mu4` trigger efficiency study using the Tag and Probe method was therefore not possible. In what follows an alternative method (called the mu4Trk method) to determine the `EF_mu4` efficiency is presented.

4.4 Method to determine the `EF_mu4` trigger efficiency

The `EF_mu4` trigger efficiency is determined by studying the efficiency of the various components and by combining the contribution from the inner detector and muon spectrometer. An event is triggered by `EF_mu4` if the trigger recognises a muon with $p_T > 4\,\text{GeV}$ as a muon spectrometer track matched to an inner detector track. Only if the inner detector track and the MS track are combined to be the same object, `EF_mu4` is able to trigger the event. The `EF_mu4` efficiency can be therefore expressed as a convolution of three pieces:

- the MS efficiency ϵ(MS): the efficiency of the Muon Spectrometer standalone,
- the ID efficiency ϵ(ID): the tracking efficiency,
- the efficiency of the combination algorithm ϵ(comb) ,

and defined as:

$$\epsilon(\texttt{EF\_mu4}) = \epsilon(\text{MS}) \otimes \epsilon(\text{comb}) \otimes \epsilon(\text{ID}). \tag{4.1}$$

In order to study each contribution separately two monitor triggers are used: the `EF_mu4_Trk_Jpsi` trigger for the $\epsilon(\text{MS}) \otimes \epsilon(\text{comb})$ part, and the `EF_mu4_IDTrkNoCut` trigger for the ϵ(ID) part. The `L1_MU0` efficiency is also determined using the trigger `EF_mu4_Trk_Jpsi`.

The trigger efficiency measured is the relative efficiency with respect to the offline reconstruction as it depends on the presence of an offline combined muon reconstructed using the `Muid` algorithm.

4.4.1 LVL1, MS and combination efficiencies

EF_mu4_Trk_Jpsi is a di-muon trigger seeded by L1_MU0. At the HLT a mu4 object corresponding to the LVL1 muon RoI is confirmed. At this stage the algorithm searches for a track object Trk in the vicinity of the mu4 object, such that the two objects are less than 0.75 apart in both $\Delta\eta$ and $\Delta\phi$. Both the mu4 and the Trk objects are restricted to have a minimum transverse momentum of 4 GeV. Moreover the system of mu4 and Trk objects is required to be oppositely charged and the invariant mass to be in the range from 2.85 GeV to 3.35 GeV. A summary of the requirements of the trigger is given in Table 4.1.

This trigger ran almost always unprescaled in 2010 and collected a total of about $32\,\mathrm{pb}^{-1}$ of integrated luminosity (see Table 4.2 for details).

An ideal and schematic decay of a J/ψ to two muons is shown in Figure 4.1. The two reconstructed muons are labelled 1 and 2. The trigger EF_mu4_Trk_Jpsi in the diagram has triggered the event with objects A (the tag mu4) and B (the probe Trk). In this ideal case a second combination of trigger objects is also found. This corresponds to the pair C (mu4) and D (Trk), also associated to the two offline muons. The probe B tests the L1_MU0 efficiency and also the ϵ(MS) and ϵ(comb).

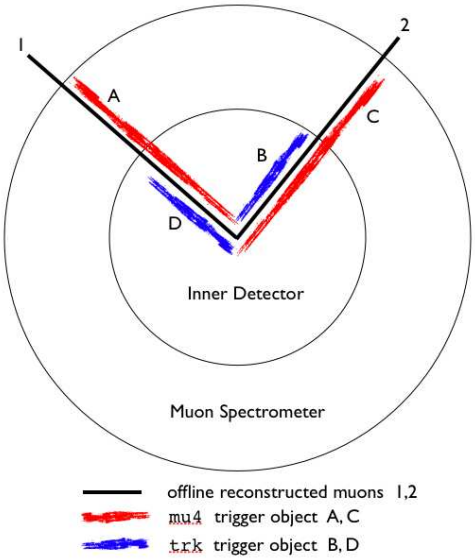

Figure 4.1: *Diagram representing a J/ψ decay to two muons reconstructed offline and labelled 1 and 2. The trigger objects of the* EF_mu4_Trk_Jpsi *trigger are also shown. In the ideal case of a fully efficient trigger, the event would be triggered twice. The two pairs of trigger objects are labelled A, B and C, D.*

This first investigation does not give the full EF_mu4 trigger efficiency as it relies on the existence of the Trk object. The trigger object mu4 is a combined object, consisting of a Muon Standalone (MS) object and an Inner Detector (ID) object. In

addition the MS and ID track segments must be fitted to a common track, using the `muComb` algorithm. As already mentioned the efficiency of `EF_mu4` is the convolution of all of the above contributions. By trying to match the `Trk` object to the `mu4` object the MS piece and the combination of MS and ID piece can be determined. To determine the ID piece of the efficiency the `EF_mu4_IDTrkNoCut` trigger is used, as the `EF_mu4_Trk_Jpsi` relies on the existence of a `Trk` object.

Offline selection, matching and results

Only events triggered by `EF_mu4_Trk_Jpsi` are selected. Each of these is required to contain at least two combined `Muid` muons with transverse momentum greater than 3 GeV and $|\eta| < 2.4$. Each of the ID tracks associated to the muons is required to pass the Muon Combined Performance recommendations for release 16 [48] summarised as follows:

- Requirement that there is at least one pixel b-layer hit associated to the muon, except for the case in which the muon track passes an uninstrumented or dead area of the b-layer,
- Number of pixel hits + number of crossed dead pixel sensors > 1,
- Number of SCT hits + number of crossed dead SCT sensors ≥ 6,
- Number of pixel holes[1] + number of SCT holes < 2,
- Let $N_{TRT,hits}$ denote the number of TRT hits on the muon track, $N_{TRT,outliers}$ the number of TRT outliers on the muon track, and $N \equiv N_{TRT,hits} + N_{TRT,outliers}$,
  - If $|\eta| < 1.9$ require: $N > 5$ and $N_{TRT,outliers} < 0.9 \times N$,
  - If $|\eta| > 1.9$. If $N > 5$, then require $N_{TRT,outliers} < 0.9 \times N$,

All muons passing the above criteria are henceforth referred to as "Good quality muons".

[1] In track reconstruction, a hit refers to a measurement that has been associated to a track whereas a hole is an expected measurement given the track trajectory that has not been assigned to the track [49].

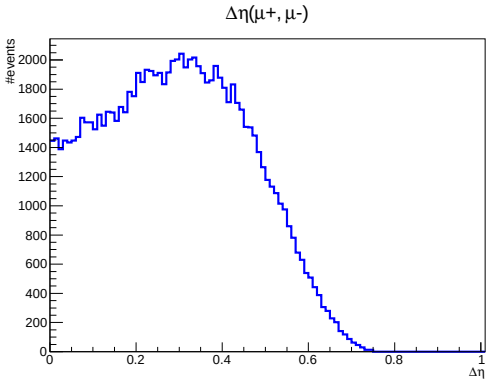

(a) $\Delta\eta_{\mu\mu}$.

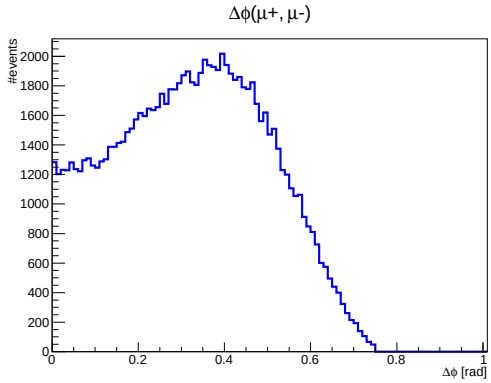

(b) $\Delta\phi_{\mu\mu}$.

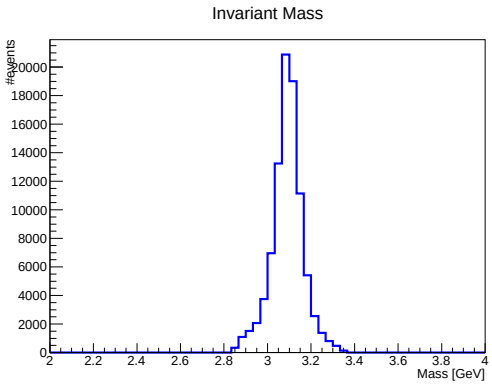

(c) $M_{\mu\mu}$.

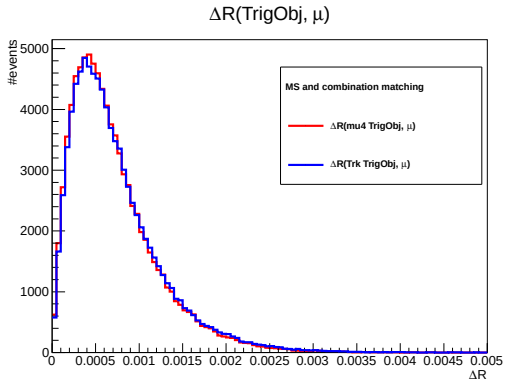

(d) $\Delta R_{\mu,\texttt{trig}}$.

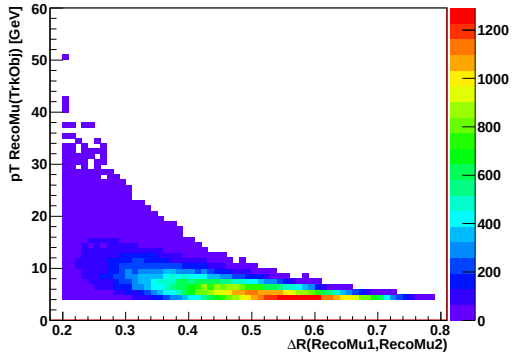

(e) $\Delta R_{\mu\mu}$ as a function of $p_{T,\mu}$.

Figure 4.2: *Distribution of $\Delta\eta$, $\Delta\phi$ and invariant mass for selected reconstructed di-muon pairs in data (a-c). In (d) the ΔR separation of offline muons to trigger objects after matching is shown. Finally in (e) the correlation between the spatial distribution and the transverse momentum of reconstructed muons from J/ψ events is shown.*

Out of all possible pairs of opposite-sign muons only the ones which satisfy the same selection as at the trigger level are retained. Therefore all pairs of offline muons are required to have $\Delta\eta_{\mu\mu} < 0.75$ and $\Delta\phi_{\mu\mu} < 0.75$ and have an invariant mass in the range [2.85 GeV, 3.35 GeV]. Also, a minimum separation ($\Delta R_{\mu\mu} > 0.2$) between the two offline muons is required in order to avoid any possible RoI overlap. Each pair of muons that passes the above selection is retained as a possible J/ψ candidate to be used in the trigger efficiency determination. Figure 4.2 shows the $\Delta\eta_{\mu\mu}$ (a), $\Delta\phi_{\mu\mu}$ (b), and invariant mass $M_{\mu\mu}$ (c) distributions for all selected pairs of reconstructed muons. They confirm that the requirements are applied correctly. Figure 4.2(e) shows the correlation of the p_T of the offline muons matched to the `Trk` trigger and the $\Delta R_{\mu\mu}$ separation between the two offline muons. As can be seen the majority of muons with low p_T lie at larger $\Delta R_{\mu\mu}$.

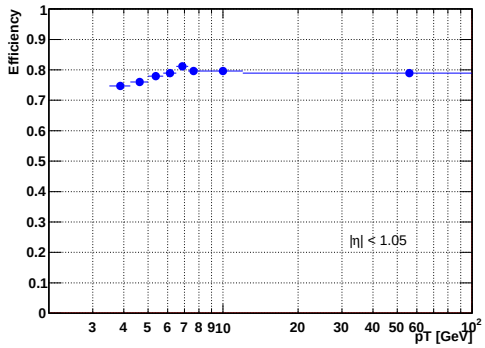

(a) `L1_MU0` efficiency as a function of p_T of the muon in the Barrel region.

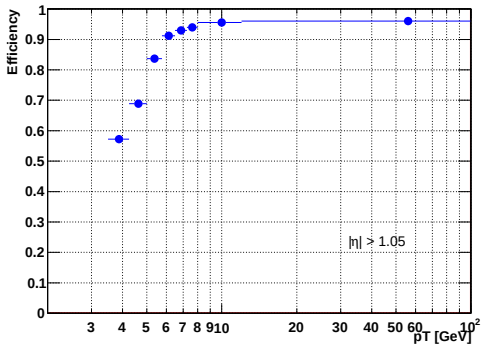

(b) `L1_MU0` efficiency as a function of p_T of the muon in the Endcap region.

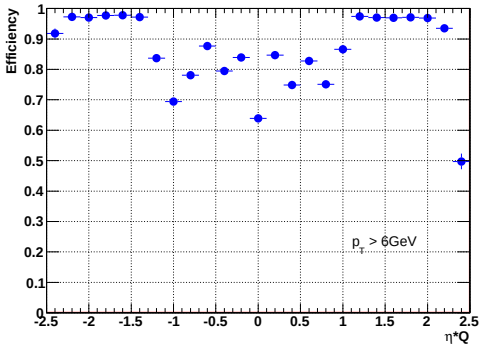

(c) `L1_MU0` efficiency as a function of $\eta \times Q$ of the muon for muons of $p_T > 6$ GeV.

Figure 4.3: `L1_MU0` *trigger efficiency with respect to the offline Muid muon. The efficiency as a function of the offline muon with* $|\eta| < 1.05$ *is shown in (a) and with* $|\eta| > 1.05$ *is shown in (b). The efficiency as a function of* $\eta \times Q$ *is shown in (c).*

The next step is to uniquely match the trigger objects `mu4` and `Trk` to the two reconstructed muons. The match must be unique and the discrimination is done by choosing the closest match in ΔR between the trigger object and the offline muon, and then excluding the muon to be a possible candidate to be matched to the other object. The event is rejected from the study if the ΔR match is larger than 0.005. Figure 4.2(d) shows the ΔR distribution of the match between the `mu4` trigger object and the reconstructed muon (in red) and the match between the `Trk` object and the reconstructed muon (in blue). Once the unique match is found the muon associated to the `Trk` trigger object is tested for trigger efficiency determination while the other muon acts as the equivalent of the tag muon in the Tag and Probe method.

The sample of reconstructed muons matched to the trigger `Trk` objects defines the denominator of the efficiency. The subset of events in which the muon is matched to a LVL1 muon RoI is the numerator of the `L1_MU0` efficiency. Instead, the subset of events for which the muon is matched to a `mu4` trigger object is the numerator of the trigger efficiency that tests the MS only and the combination efficiencies. In summary the efficiencies considered in this study are defined as:

$$\epsilon(\texttt{L1\_MU0}) = \frac{\text{N. reco. muons matched to a } \texttt{Trk} \text{ obj and to a } \texttt{L1\_MU0} \text{ RoI}}{\text{N. reco. muons matched to a } \texttt{Trk} \text{ obj}}, \quad (4.2)$$

and

$$\epsilon(\text{MS}) \otimes \epsilon(\text{comb}) = \frac{\text{N. reco. muons matched to a } \texttt{Trk} \text{ obj and to a } \texttt{mu4} \text{ obj}}{\text{N. reco. muons matched to a } \texttt{Trk} \text{ obj}}. \quad (4.3)$$

Figure 4.3 (a) and (b) show the `L1_MU0` efficiency as a function of the p_T of the offline `Muid` muon in the Barrel ($|\eta| < 1.05$) and Endcap regions ($|\eta| > 1.05$) respectively. The efficiency is lower in the Barrel than in the Endcaps. This is due to the reduced geometrical acceptance of the trigger systems in the Barrel where the supporting structures of the ATLAS detector cause the inefficiency. Also the efficiency as a function of the product of η and the charge (Q) of the offline muon is shown in Figure 4.3 (c). The choice of plotting the product $\eta \times Q$ is motivated by the fact that there is a charge dependence of the muon trigger and reconstruction efficiencies particularly relevant at large $|\eta|$ and in the low p_T region. This is due to the toroidal magnetic field of the Muon Spectrometer of ATLAS. Muons with positive charge will be bent towards larger η and the ones with negative charge towards smaller η. Therefore at very large $|\eta|$ the muons may be bent into a region which is outside the detector acceptance and consequently they may fail to

be reconstructed and/or triggered.

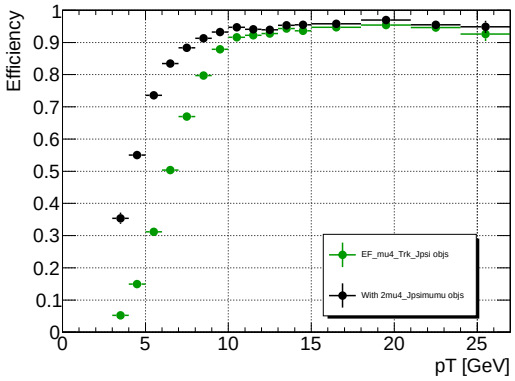

(a)

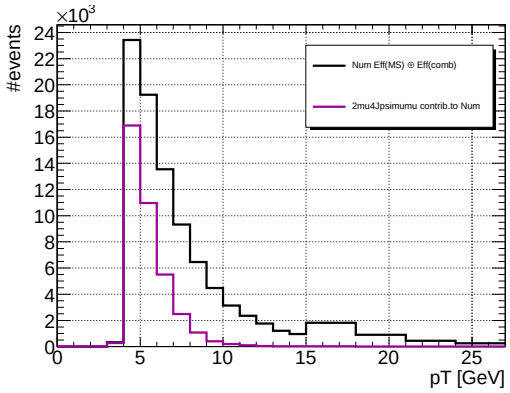

(b)

Figure 4.4: *(a): MS and combination trigger efficiency before (green) and after (black) the efficiency is improved by looking for a* `mu4` *match using a different chain. In (b) the missing matches (purple histogram) are shown to arise mostly in the low p_T region. This is why the efficiencies shown in (a) have a larger discrepancy in the low p_T region.*

At the time when the mu4Trk method was being developed the p_T turn-on-curves of the efficiency exhibited some unexpected behaviour. What was noted was that the efficiency would increase very slowly as a function of the p_T of the muon, if compared to previous analyses performed using the Tag and Probe method and based on simulated events and on first collision data from periods A to E[2]. An example of this is given by the efficiency shown in green in Figure 4.4(a). After some investigation it was found that (using the notation in Figure 4.1) sometimes the algorithm would trigger the event with objects A and B and not with objects

[2]The number of events collected during these data periods was not enough to estimate the `EF_mu4` trigger efficiency from data.

C and D, although the muon object C was tagged as a `mu4` object by a different trigger. The efficiency was improved by looking for `mu4` objects in events which were triggered by a different muon trigger, i.e. the `EF_2mu4_Jpsimumu`[3] trigger was used. In many cases the `Trk` object was successfully matched to a `mu4` object of the `EF_2mu4_Jpsimumu` trigger. A large improvement was achieved in the efficiency as can be seen in Figure 4.4(a) where the black dots represent the improved efficiency. The purple histogram in Figure 4.4(b) shows the total number of events in which the `Trk` objects, after failing to be matched to a `mu4` object within the `EF_mu4_Trk_Jpsi` trigger, is successfully matched to a `mu4` object of the `EF_2mu4_Jpsimumu` trigger. The overall number of events for which the `Trk` object is successfully matched (within the `EF_mu4_Trk_Jpsi` trigger or the `EF_2mu4_Jpsimumu` trigger) is shown in black. Note how the majority of muons not identified by `EF_mu4_Trk_Jpsi` lie in the low p_T region.

All the problematic events were found to have common characteristics: in order for a track to be confirmed as a `mu4` trigger object, it is required that both $\Delta\eta$ and $\Delta\phi$ between the track and the LVL1 muon RoI are less than 0.1. All the problematic events had the $\Delta\phi$ just above 0.1 and therefore the algorithm failed. A more robust solution was found by trigger experts [50, 51] to retrieve all of the event filter `mu4` objects which seeded `EF_mu4_Trk_Jpsi`, and not just the ones entering the Level-1 algorithm. These objects were added to the TrigEffJpsiTool under the name of `mu4_All` objects. The trigger efficiency results at the event filter i.e $\epsilon(\text{MS})\otimes\epsilon(\text{comb})$, shown in this section are obtained with the inclusion of the `mu4_All` objects and whether or not the `Trk` object used to test the efficiency is matched to one of them.

The MS only and combination efficiencies are shown in Figure 4.5. Here the contribution of positively and negatively charged muons is shown separately: positive charges are shown on the left column and negative charges on the right column. As for the `L1_MU0` efficiency, here the p_T dependence in the Barrel region (a),(b) and in the Endcap regions (c),(d) is shown. The efficiency as a function of η is shown in (e) and (f). Here the charge dependence motivated above can be seen explicitly. In fact positive muons show a loss in efficiency for $\eta \gtrsim 2.3$ while negative muons show a loss in efficiency for $\eta \lesssim$ -2.3.

[3] `EF_2mu4_Jpsimumu` requires two `mu4` oppositely charged objects, a vertex χ^2 match and the invariant mass of the two objects to be between 2.5 and 4.3 GeV.

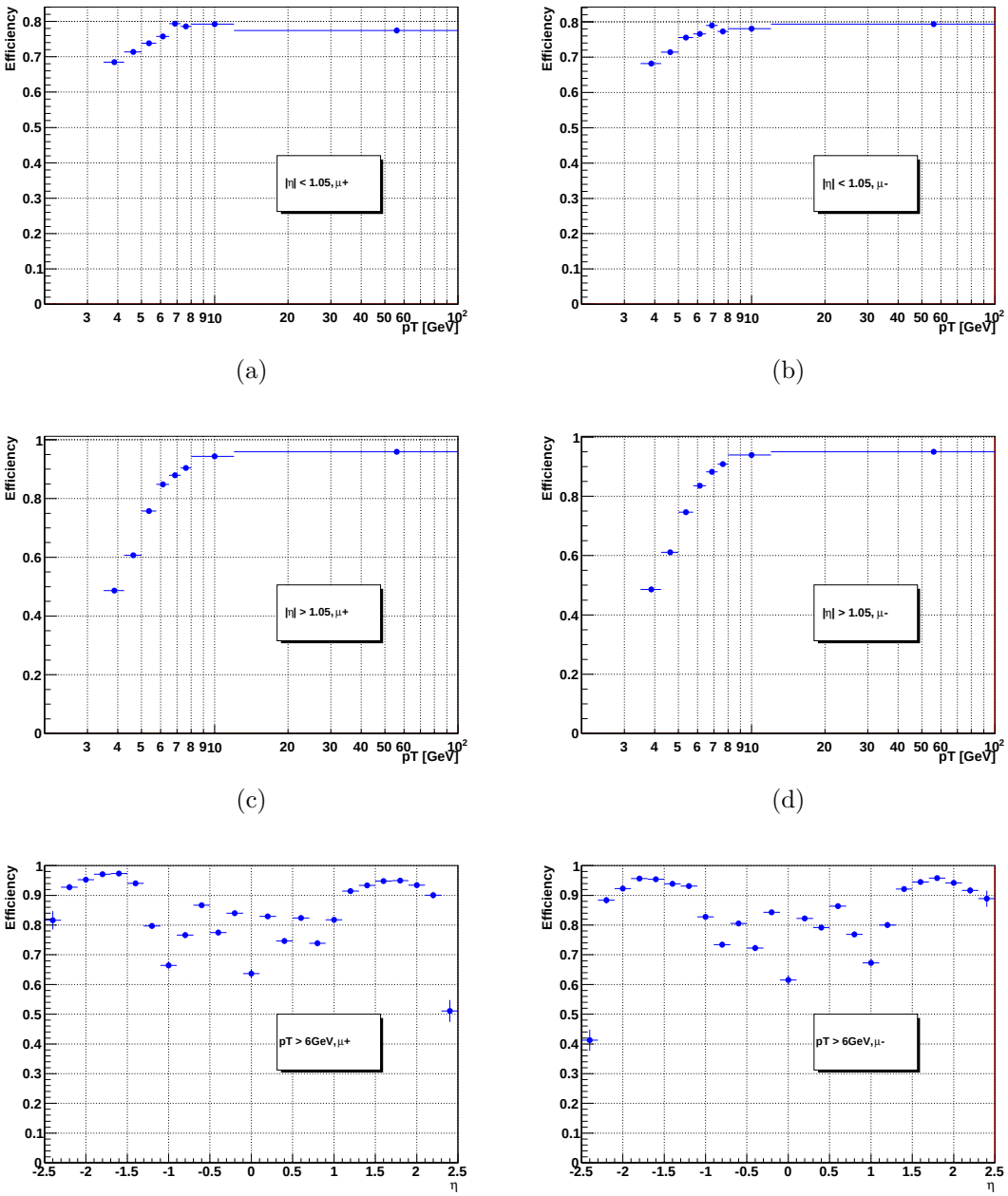

Figure 4.5: *MS only and combination trigger efficiency ($\epsilon(MS) \otimes \epsilon(comb)$) with respect of the offline muon. The left column is with respect to positive muons and the right column is with respect to negative muons. (a) and (b) show the efficiency as a function of the offline muon p_T, for $|\eta| < 1.05$; (c) and (d) show the efficiency as a function of the offline muon p_T, for $|\eta| > 1.05$. The efficiency as a function of η is shown in (e) and (f).*

4.4.2 Tracking efficiency

The missing part of the efficiency is the tracking efficiency. To determine its contribution, the monitor trigger `EF_mu4_IDTrkNoCut` is used.

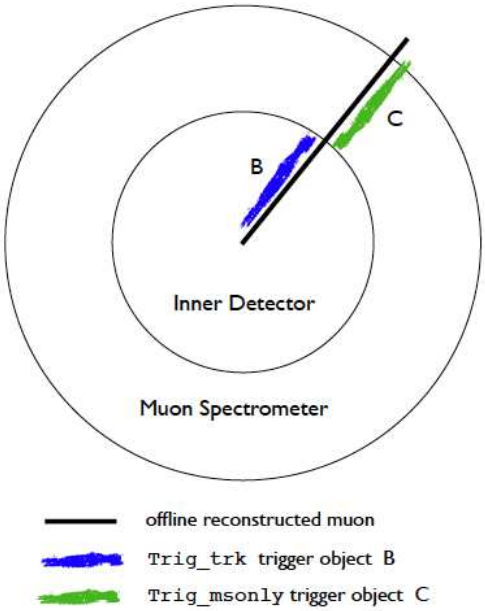

Figure 4.6: *Diagram representing an offline muon (solid black line). Also shown are the trigger objects of the* `EF_mu4_IDTrkNoCut` *chain. The object labelled B is the ID track and the one labelled C is the MS-only trigger track.*

`EF_mu4_IDTrkNoCut` is a single muon trigger seeded by `L1_MU0`. As suggested by the name of the chain, no requirements are imposed on the ID track. Therefore the objects of the chain are MS standalone muon objects with no minimum p_T requirement. The chain is configured such that all the ID track objects are also recorded, but the decision does not take them into account. Figure 4.6 shows a schematic diagram of a reconstructed combined muon (solid black line) and the two contributions from the trigger: MS object (A) and ID object (B). For a fully efficient trigger both contributions must exist for every offline muon. Being a single muon trigger with no stringent requirements it was always heavily prescaled in 2010, to keep the rate low to about 0.5 Hz. Nevertheless in 2010 `EF_mu4_IDTrkNoCut` collected $\approx 6.4 \times 10^6$ events. Therefore there was sufficient statistics for the tracking trigger efficiency to be studied.

Offline selection, matching and results

A good sample of J/ψ events would be ideal for this study as already done with the other pieces of the efficiency. The restriction arises from data since the events

collected by `EF_mu4_IDTrkNoCut` contain only about 5000 J/ψ candidates, not sufficient for an accurate trigger efficiency study. Therefore all events triggered by `EF_mu4_IDTrkNoCut` and with a least one combined `Muid` muon are considered (with no requirement on the p_T or η).

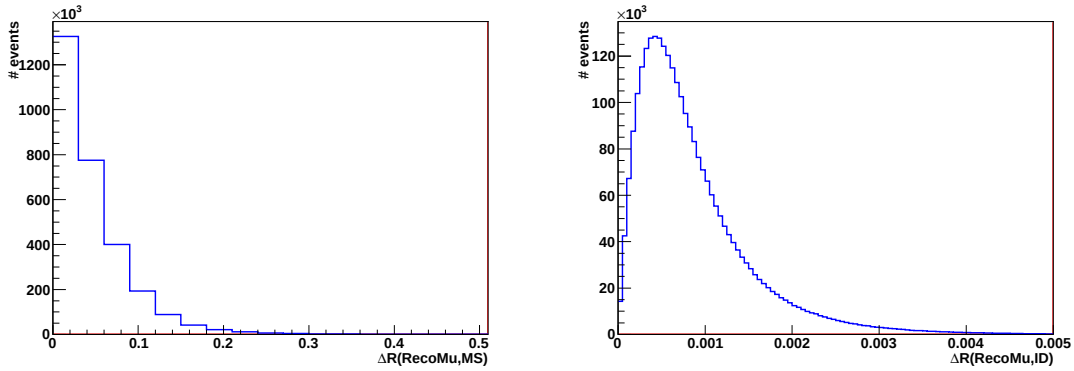

(a) (b)

Figure 4.7: *Distribution of ΔR between the offline muon and the MS objects (a) and between the offline muon and the ID track object (b).*

A sample of events is selected by matching the offline muon (its MS part) to the MS object responsible for triggering the event. Due to poor resolution of the MS only tracking, the ΔR is required to be less than 0.3. This sample defines the denominator of the ID efficiency. Each selected muon is then matched uniquely to an ID trigger object by requiring $\Delta R < 0.005$. The events in which this match can be performed successfully define the numerator of the efficiency. The ID efficiency is defined as:

$$\epsilon(\text{ID}) = \frac{\text{N. reco. muons matched to an MS obj. and to an ID obj.}}{\text{N. reco. muons matched to an MS obj.}}. \qquad (4.4)$$

Figure 4.7 shows the ΔR matching between the offline muon and the MS object (a), and between the offline muon and the ID object (b). As can be seen the matching requirements detailed above are not stringent in the rejection of events.

Efficiency results are shown in figures 4.8 and 4.9. As can be seen, the trigger efficiency of the tracking is very high everywhere in η. The source of inefficiency arises mainly from muons of p_T below 4 GeV. An unexpected loss in efficiency is observed for negative muons (see Figure 4.9 (b)) at $\eta \sim 1.4$. This problem has never been fully understood, the trigger expert have been informed about it, but a solution has not been suggested. Overall the efficiency is very high, on average about 98% for muons above 6 GeV in p_T.

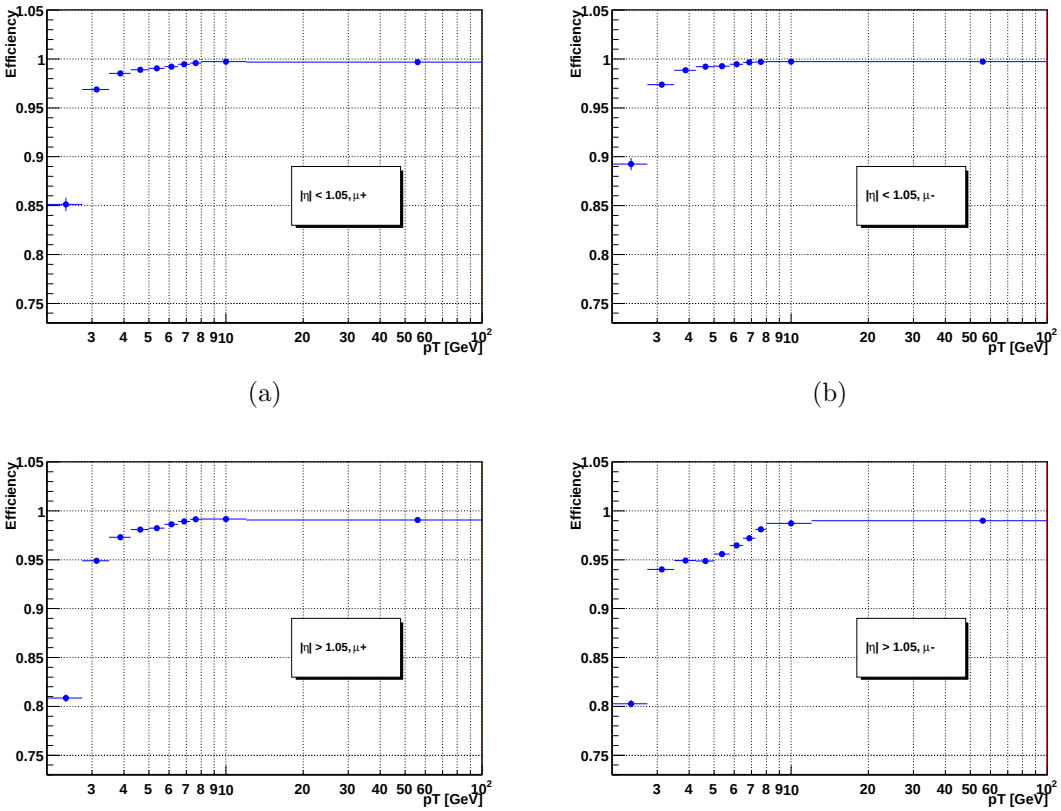

(a) (b)

(c) (d)

Figure 4.8: *ID trigger efficiency with respect to offline combined muons. Positive (negative) muons are shown on the left (right) hand-side column. (a) and (b) show the efficiency as a function of the offline muon with $|\eta| < 1.05$; (c) and (d) show the efficiency as a function of the offline muon with $|\eta| > 1.05$.*

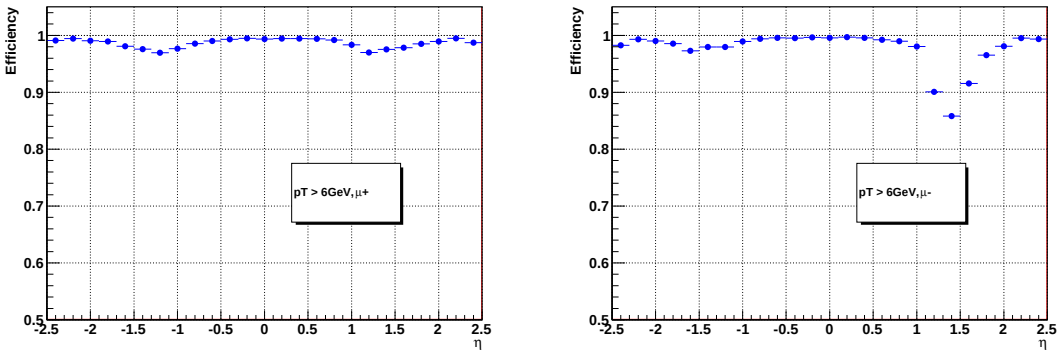

(a) (b)

Figure 4.9: *ID trigger efficiency with respect to the offline muon pseudo-rapidity; for positive (a) and negative (b) muons.*

4.5 EF_mu4 trigger efficiency

The total EF_mu4 efficiency is the convolution of the various pieces of efficiency studied above, as detailed in Equation 4.1. Figure 4.10 shows the complete EF_mu4 efficiency as a function of p_T and η of the offline muon. The figure shows the charge-separated contributions in the Barrel and Endcap regions. The shaded band represents the systematic uncertainty discussed below. As for the L1_MU0 case, the efficiency in the Barrel region is lower than in the Endcap regions. The event filter efficiency at plateau ($p_T \gtrsim 8\,\text{GeV}$) is $\sim 80\%$ in the Barrel and $\sim 95\%$ in the Endcaps.

The trigger efficiency measured is applied to the Drell-Yan analysis in a two-dimensional map as a function of p_T and $\eta \times Q$ of the offline Muid muon. For a better visualisation the results are shown here as a series of one-dimensional histograms.

4.5.1 Systematic Uncertainty on the EF_mu4 trigger efficiency

The systematic uncertainty on the trigger efficiency study performed using the mu4Trk method is assessed using two independent approaches. One is the difference between the method presented and the Tag and Probe method. The comparison is done using MC simulations where possible. The agreement of the two meaning that the mu4Trk method is robust and the results applicable to physics analyses. However, since the two methods are independent any difference between them can be regarded as a systematic uncertainty. The second source of uncertainty is determined by investigating the difference in efficiency between the central region of the J/ψ invariant mass and the side-band regions, using the mu4Trk method on data.

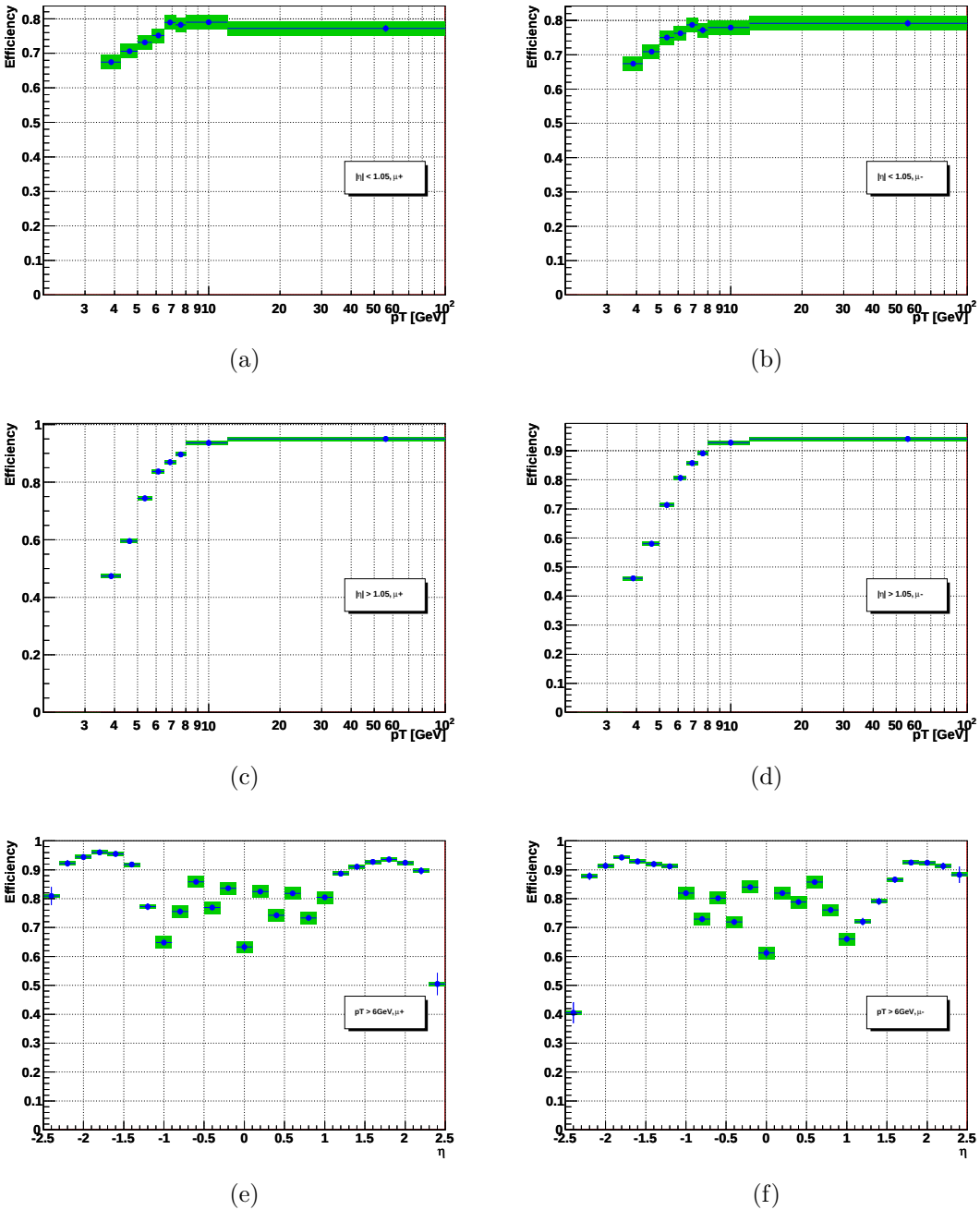

(a) (b)

(c) (d)

(e) (f)

Figure 4.10: `EF_mu4` *trigger efficiency with respect of the offline muon. Left column is with respect with positive muons, right column is with respect to negative muons. (a) and (b) show the efficiency as a function of the offline muon with* $|\eta| < 1.05$*; (c) and (d) show the efficiency as a function of the offline muon with* $|\eta| > 1.05$*. Also the efficiency as a function of* η *is shown in (e) and (f).*

Comparison between the mu4Trk and the Tag and Probe method

The `EF_mu4` trigger efficiency using a standard J/ψ Tag and Probe analysis is only possible on MC samples as motivated in Section 4.3. As also mentioned previously the 2010 simulations (MC10) have an error in the configuration of the `EF_mu4` algorithm and cannot be used for trigger efficiency studies. Therefore the comparison between the two methods is done using 2011 simulation (MC11). Unfortunately the ID piece of the efficiency cannot be measured on MC11, as the MC11 trigger menu does not include the `EF_mu4_IDTrkNoCut` trigger.

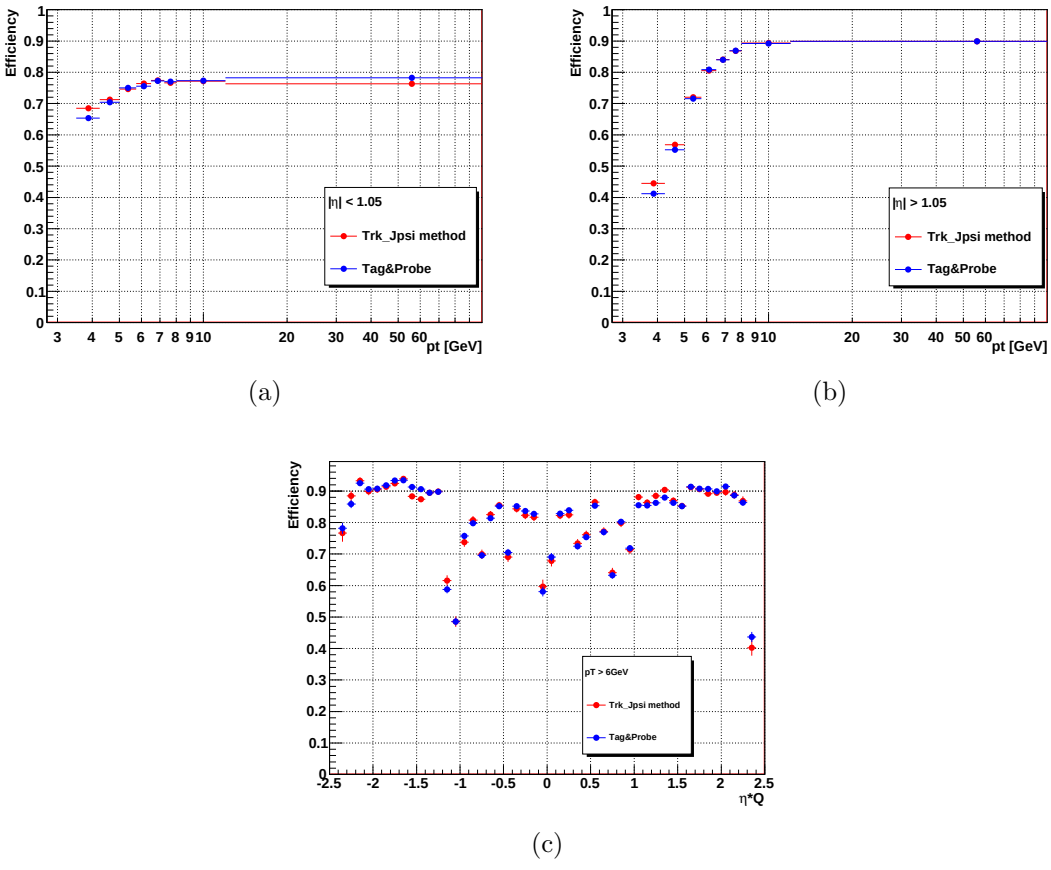

Figure 4.11: *Comparison between the Tag and Probe method and the mu4Trk method presented to measure the* `EF_mu4` *trigger efficiency. The difference between the two is one of the sources of systematic uncertainty.*

Therefore the ID piece of the efficiency cannot be estimated from the MC10 or MC11 simulations. Only for the ID piece of the trigger efficiency ϵ(ID) the results obtained from data (see Section 4.4.2) are used in this comparison. In summary, the comparison between the mu4Trk method and the Tag and Probe method is performed considering:

- MC11 for the Tag and Probe method,
- MC11 for the mu4Trk method to measure $\epsilon(\text{MS}) \otimes \epsilon(\text{comb})$,
- 2010 data for the mu4Trk method to measure the $\epsilon(\text{ID})$.

The offline selection applied for this study (for both the mu4Trk and standard Tag and Probe method) is the same as described in Sections 4.4.1 and 4.4.2. Figure 4.11 shows the comparison of the two methods. The `EF_mu4` efficiency in blue has been estimated using the Tag and Probe method, the one in red is the result of the mu4Trk method. The two methods are in good agreement within the statistical uncertainty, except for the low p_T region where the mu4Trk method gives a larger efficiency. Moreover, for p_T below 4 GeV the two methods are not comparable, as the ID efficiency estimated from data using `EF_mu4_IDTrkNoCut` has no lower p_T requirement, while the `EF_mu4` trigger has a 4 GeV minimum requirement on the trigger object.

The uncertainty associated with the difference of the two methods is shown in Figure 4.12 separately for the Barrel (a) and Endcap (b) regions. A linear fit is performed in the region $5.75 < p_T < 100.0$ GeV (although the plots in the figure show only the p_T region less than 12 GeV) in order to estimate the average difference. In the Barrel region the average difference (fit parameter) is 0.003% while in the Endcap region it is -0.004%. Since in the Drell-Yan analysis offline `Muid` muons are selected with $p_T > 6$ GeV, the systematic uncertainty associated with the method used is negligible. The fact that the two methods agree so well is an important robustness check on the measurement and it increases the confidence on the result.

The systematic uncertainty associated with the `EF_mu4` efficiency is estimated using the second approach detailed below.

J/ψ peak and side-bands

A second check of the systematic uncertainty is performed on data by comparing the efficiency $\epsilon(\text{MS}) \otimes \epsilon(\text{comb})$ obtained using the mu4Trk method, from the central peak and side-bands of the selected J/ψ sample. The J/ψ sample is not pure and contains some fraction of combinatoric QCD background. This background may have a lower efficiency for `EF_mu4` than true prompt muons.

To estimate the influence of this effect the analysis is performed separately in the central peak and the sidebands of the J/ψ sample using 2010 data. Due to the tight mass window employed[4] in the trigger requirement (see Table 4.1) the two regions

[4] A wider mass window is used for 2011 and 2012 data taking for this reason.

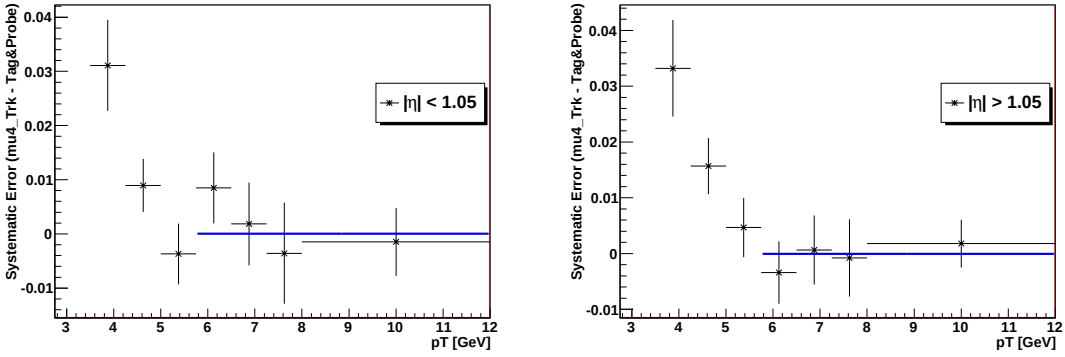

(a) (b)

Figure 4.12: *Systematic uncertainty on the* `EF_mu4` *efficiency estimated from the difference between the Tag and Probe method and the mu4Trk method. For muons above 6 GeV in* p_T *the systematic difference is negligible.*

are defined as: $3.0 < M < 3.2\,\text{GeV}$ and $2.85 < M < 3.0$ or $3.2 < M < 3.35\,\text{GeV}$ as shown in Figure 4.13 (d). In the figure the efficiency as a function of p_T in the Barrel and Endcaps and $\eta \times Q$ of the offline muon is also shown. The efficiency evaluated from the central region (in purple) and the side-bands is shown in green. Although the comparison gives very similar results, some differences can be seen and must be taken into account. The difference is shown in Figure. 4.14, separately for the Barrel and Endcap regions. For $p_T > 5.75\,\text{GeV}$ a linear fit is carried out. This is shown by the solid red line. Due to the low number of events contributing in the side-band regions, the differences show large statistical error. A conservative approach is therefore adopted: the efficiency is evaluated in two mass bins, one below p_T of 6 GeV and one from 6 to 100 GeV. The systematic error is defined as the sum in quadrature of the efficiency difference and the associated statistical error. In the region of $p_T > 6\,\text{GeV}$ this is shown by the solid blue line. In the Barrel region the systematic uncertainty is estimated to be 2.1% whereas in the Endcap region is 0.65%. This is used to define the total systematic uncertainty of the `EF_mu4` efficiency.

To conclude, the systematic uncertainty associated to the `EF_mu4` efficiency for muons of $p_T > 6\,\text{GeV}$ is estimated to be:

- 2.1% for $|\eta| < 1.05$,
- 0.65% for $|\eta| > 1.05$,

as shown in Figure 4.14 (solid blue line).

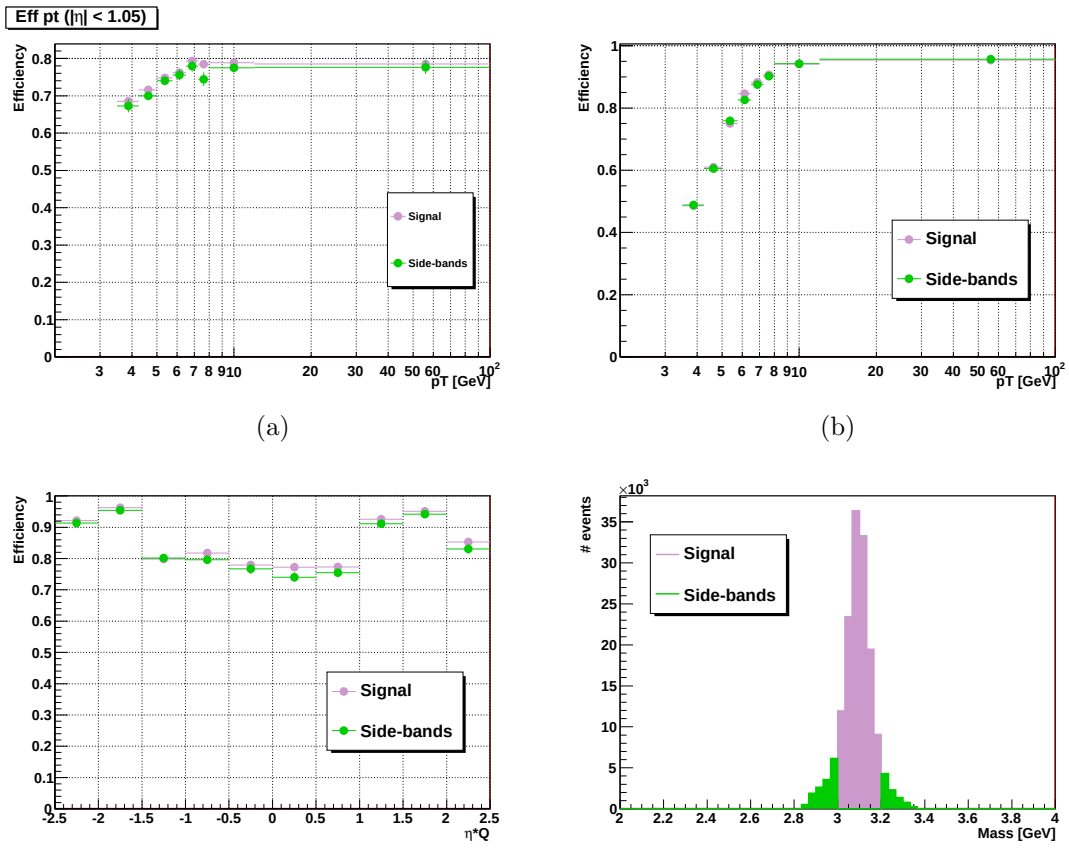

Figure 4.13: *Comparison between the efficiency measured in the signal and side-band regions. The efficiency as a function of p_T in the Barrel and Endcap regions is shown in (a) and (b) respectively. (c) shows the difference as a function of $\eta \times Q$. The mass spectrum selected in the two regions is shown in (d).*

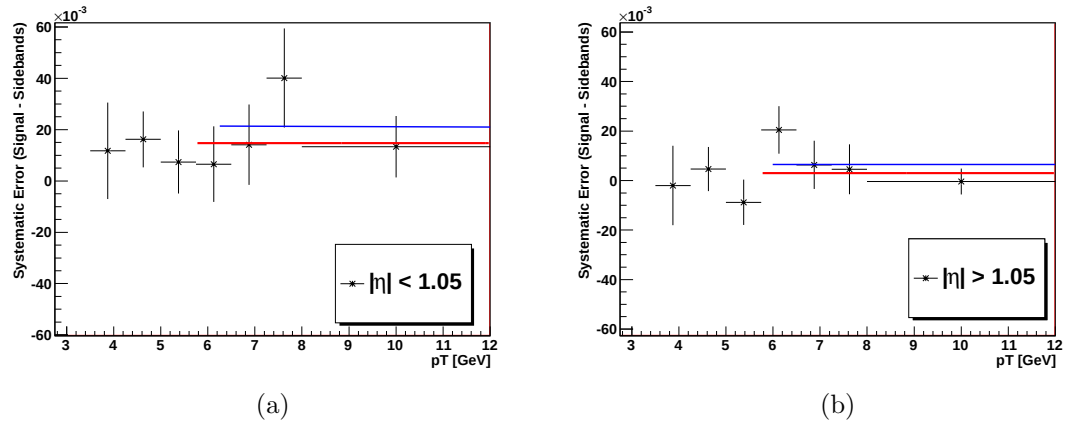

Figure 4.14: *Differences between the efficiency measured in the signal and side-band regions. For muons of $p_T > 6.0\,GeV$ a systematic shift is considered.*

4.6 Method to determine the Vtx and OS trigger efficiency

Having obtained the efficiency maps of `EF_mu4` the remaining vertex and opposite sign conditions (Vtx+OS) of the physics trigger `EF_2mu4_DiMu` is estimated. This is done by using the `EF_2mu4_DiMu_noVtx_noOS` support trigger. As listed in Table 4.1 the requirements on this trigger are the same as for `EF_2mu4_DiMu` except for the requirements on the opposite charge and on the χ^2 of the vertex fit which are dropped. The important difference between this study and the previous one is the sample of events studied. he J/ψ events are mostly used for the `EF_mu4` trigger efficiency measurement, whereas a Drell-Yan signal sample of events is considered here, together with the QCD background contribution. This is because the Vtx+OS efficiency is evaluated as a function of the kinematic variables of the vector boson and therefore the Drell-Yan event sample is the adequate one to use in this study.

The efficiency is determined as the ratio of selected events triggered by both the support and physics trigger, to the number of selected events triggered by the support trigger, such that:

$$\epsilon(Vtx{+}OS) = \frac{\text{N. events triggered by } \texttt{EF\_2mu4\_DiMu} \text{ and } \texttt{EF\_2mu4\_DiMu\_noVtx\_noOS}}{\text{N. events triggered by } \texttt{EF\_2mu4\_DiMu\_noVtx\_noOS}}. \tag{4.5}$$

This study has been performed in data as well as using MC simulation. Although the simulation results are not used in the Drell-Yan analysis[5] they are shown with the data results for completeness. The "MC10" simulated event samples listed in Table 4.3 were used. These include the Drell-Yan simulated signal event samples as well as the simulated heavy flavour QCD event samples. The QCD background contribution to the Drell-Yan spectrum is large and cannot be neglected in the efficiency study; it is therefore added[6] to the signal sample so that comparison with data is more appropriate. The offline selection (similar to the Drell-Yan selection) chosen to perform the study is:

- At least two `Muid` combined muons,
- Good quality muons (see Section 4.4.1),

[5]Instead the efficiency determined in data is applied to the simulated event samples in the Drell-Yan analysis.

[6]The simulated heavy flavour QCD background sample is normalised to data in a control region defined by inverting the isolation requirements on both muons. This region is dominated by QCD background events.

- $p_T > 3\,\text{GeV}$, $|\eta| < 2.4$ (both muons),
- χ^2 (muon to the vertex fit) < 20 and opposite charge requirement on the muons (to reproduce trigger requirement),
- $12\,\text{GeV} < M < 66\,\text{GeV}$,
- isolation requirements on both muons: `ptCone40` $< 1\,\text{GeV}$ and `etCone40` $< 1.5\,\text{GeV}$,

where `ptCone40` is defined as the sum of transverse momentum of all tracks found in a cone of $\Delta R = 0.4$ around the muon (the muon p_T is subtracted from the sum), and `etCone40` is the sum of transverse energy of energy deposits found in the calorimeter in a cone of $\Delta R = 0.4$ around the muon (the muon energy is subtracted from the sum). The signal efficiency achieved using these isolation requirements is about 72% and it is associated with a background rejection of about 96%. The isolation variables are discussed in detail in Section 5.4.1.

The efficiency is studied as a function of di-muon kinematic quantities such as the invariant mass $M(Z/\gamma^*)$, transverse momentum $p_T(Z/\gamma^*)$ and rapidity $Y(Z/\gamma^*)$, and the results are shown both for data and simulation in Figure 4.15. The agreement between data and simulation is reasonable within the statistical uncertainty. Furthermore, the greatest variation is in the rapidity dependence. Therefore the choice of applying this contribution to the trigger efficiency as a function of the Z/γ^* rapidity (the absolute value). Note that initially the study has been performed taking into account the sign of the rapidity. The $|Y|$ distribution is chosen since there is no sign dependence.

4.6.1 Systematic uncertainty

The systematic uncertainty is estimated on data only by changing the mass range used to the regions $12 < M < 25\,\text{GeV}$ and $25 < M < 66\,\text{GeV}$. The different mass regions change the purity of the sample since, for example, the background contribution from non-prompt di-muon pairs for $M > 25\,\text{GeV}$ is small. In order to change the amount of background included in the sample, a study varying the isolation requirement has also been performed, but the mass variation gives a bigger uncertainty.

In Figure 4.16 (a) the efficiency is shown as a function of $|Y|$ in the three mass ranges, the default range in black, the $12 < M < 25\,\text{GeV}$ region in red and the $25 < M < 66\,\text{GeV}$ region in blue. The difference in efficiency between the three

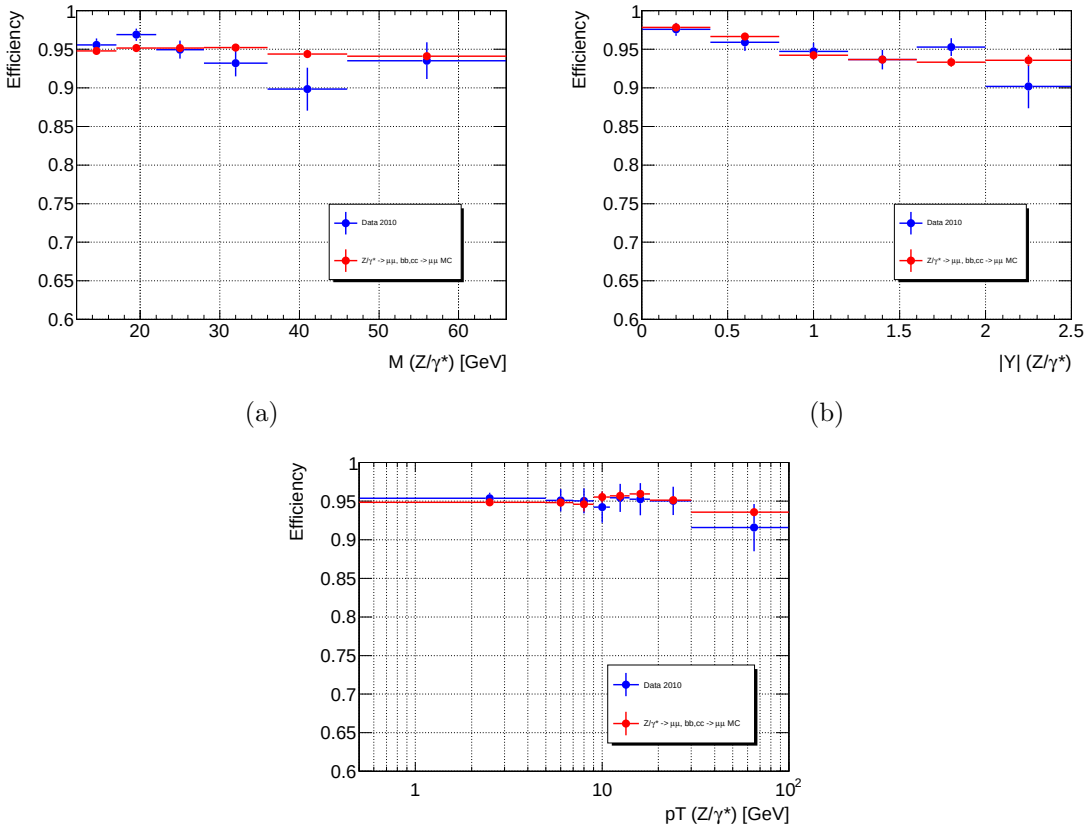

Figure 4.15: *Efficiency of the vertex and opposite sign requirements on the* `EF_2mu4_DiMu` *trigger. The efficiency is measured both in data (blue) and in simulations (red) and is studied as a function of the invariant mass $M(Z/\gamma^*)$, rapidity $Y(Z/\gamma^*)$ and transverse momentum $p_T(Z/\gamma^*)$ of the di-muon pair.*

ranges is not large. There is no strong evidence for any systematic effect, but nevertheless a small systematic uncertainty is conservatively assigned.

The uncertainty is calculated as the average variation from considering the upper mass range $25 < M < 66\,\text{GeV}$ (UP) and lower mass range $12 < M < 25\,\text{GeV}$ (DOWN) and the efficiencies determined in these restricted regions in mass, $\epsilon(\text{UP})$ and $\epsilon(\text{DOWN})$ respectively. It is defined as:

$$\delta(\text{Vtx+OS}) = 0.5\left(\frac{|\epsilon(\text{Default}) - \epsilon(\text{DOWN})|}{\epsilon(\text{Default})} + \frac{|\epsilon(\text{UP}) - \epsilon(\text{Default})|}{\epsilon(\text{Default})}\right), \qquad (4.6)$$

where $\epsilon(\text{Default})$ denotes the efficiency calculated in the region $12 < M < 66\,\text{GeV}$.

The systematic uncertainty is shown in Figure 4.16 (b). In the Drell-Yan analysis the uncertainty is taken to be:

- 0.3% for $|Y| < 1.2$,
- 1.0% for $1.2 < |Y| < 2.0$,
- 2.0% for $|Y| > 2.0$.

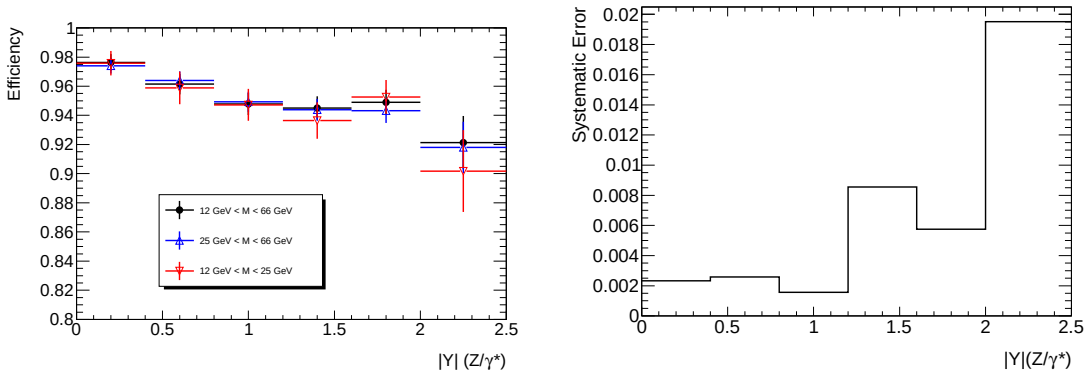

(a) (b)

Figure 4.16: *Efficiency of the vertex and OS conditions of the* `EF_2mu4_DiMu` *trigger in different regions of the di-muon invariant mass as a function of the absolute value of the di-muon rapidity* $|Y|$ *(a), and the resulting systematic difference (b).*

4.7 `EF_2mu4_DiMu` efficiency

The efficiency of the `EF_2mu4_DiMu` trigger has been studied in all its components. The results from data are applied to the simulation used in the Drell-Yan analysis presented in later sections.

The `EF_mu4` trigger efficiency is used to estimate the efficiency of `EF_2mu4` by considering the di-muon trigger efficiency to be the independent combined efficiency of two `EF_mu4` triggers. The `EF_mu4` efficiency is applied to each muon as a function of the muon p_T and $\eta \times Q$. The Vtx+OS efficiency is applied on an event-by-event basis as a function of the rapidity of the Z/γ^*. The total efficiency of the `EF_2mu4_DiMu` trigger is defined as:

$$\epsilon(\texttt{EF\_2mu4\_DiMu}) = \epsilon(\texttt{EF\_mu4})_{\text{Mu1}} \times \epsilon(\texttt{EF\_mu4})_{\text{Mu2}} \times \epsilon(\text{Vtx+OS})_{Z/\gamma^*}, \qquad (4.7)$$

where Mu1 and Mu2 are the two offline muons selected in the event.

Figure 4.17 shows the two-dimensional `EF_mu4` map as a function of p_T of the offline muon and the $\eta \times Q$. This map is applied to the Drell-Yan analysis. The Vtx+OS efficiency is applied as in Figure 4.15 (b) considering the data (blue) results.

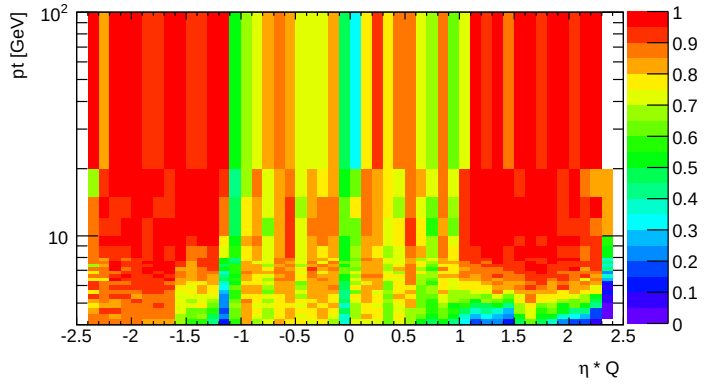

Figure 4.17: *Map of* `EF_mu4` *efficiency as a function of* p_T *and* $\eta \times Q$ *of the offline Muid muon. The map is used in the di-muon Drell-Yan analysis.*

Chapter 5

Drell-Yan di-muon event selection and associated corrections

In this chapter the Drell-Yan (DY) di-muon analysis using ATLAS data collected during 2010 is presented in all its aspects. The data sample and simulated event samples used as signal and background samples are described. The event selection is detailed and final comparison between data and simulations shown. Furthermore, all the weights applied to the MC samples are motivated, described and in many cases derived directly. The QCD processes are the most significant source of background to the Drell-Yan process especially in the low di-muon invariant mass region considered. Their contribution is studied and presented in what follows. In order to optimise the rejection of this source of background the isolation variables are introduced and extensively studied. The use of a light-flavour QCD background sample derived from data is motivated, and the overall contribution of the QCD processes are normalised appropriately using data-driven techniques. The data-to-MC ratio of events that pass the full selection is close to one, with good agreement in all distributions studied, both for the muons in the final state and for the Z/γ^* vector boson.

5.1 Data and simulated event samples

In this section a description of the Data and MC samples used in the analysis of the 2010 data is given. The data is skimmed using the most updated Good Runs List (GRL; see Section 4.2) available which, in relation to the trigger used, yields a total luminosity of $36\,\mathrm{pb}^{-1}$. In addition both data and MC samples are required to satisfy the recommended global track quality requirements in ATLAS [48]. The analysis is performed on Analysis Orientated Data (AOD) samples within the `ATHENA` framework using release 16.6.7.3.

5.1.1 Data

As already discussed in Section 2.3, data in ATLAS is organised into runs. Only 2010 data periods from E to I are used in the analysis. Details of the reprocessed data used is given in Table 4.3.

5.1.2 Signal simulated event samples

The MC samples used for comparison to data and for the cross section measurement are produced with Pythia (version 6.4) [52]. MC@NLO (version 3.42) [53] samples are also used to compare the measured cross section with theoretical predictions.

Pythia is a Monte Carlo program which uses LO matrix elements together with a parton shower scheme in order to simulate higher order emissions. MC@NLO is a more complex and accurate program which uses full NLO matrix elements, with a sophisticated matching to its parton shower scheme. This is used to avoid double counting of higher order emissions and as a result a negative event weight is assigned to approximately 10% of the events.

A summary of the signal MC samples used is given in Table 5.1. The filters applied to each sample are the generator level criteria which are imposed to one or both leptons. These usually refer to the p_T and η requirements applied. Moreover, the filter efficiency ϵ_{filter} is defined as the ratio between the number of events generated that are selected by the filters applied, over the total number of events generated. Finally the luminosity of a MC sample is defined as:

$$\mathcal{L} = \frac{N_{filter}}{\sigma_{eff}} = \frac{N_{filter}}{\sigma_{tot} \times \epsilon_{filter}} \tag{5.1}$$

where σ_{eff} is the effective cross section and N_{filter} is the number of generated events that passed the filter criteria.

Generator	M [GeV]	PDF	σ_{tot} [nb]	filters	dataset	ϵ_{filter}	GenEvt	$\mathcal{L}$ [fb^{-1}]
Pythia	8-15	MRSTLO*	4.425	$2 \times p_T > 3\,\text{GeV}$ $2 \times \lvert\eta\rvert < 2.7$	113700	0.236	1M	0.96
Pythia	15-60	MRSTLO*	1.295	$2 \times p_T > 3\,\text{GeV}$ $2 \times \lvert\eta\rvert < 2.7$	113701	0.395	1M	1.95
Pythia	> 60	MRSTLO*	0.856	-	106047	1	5M	5.05
MC@NLO	10-15	CTEQ6.6[54]	2.627	$2 \times p_T > 3\,\text{GeV}$ $2 \times \lvert\eta\rvert < 2.7$	113711	0.298	1M	1.28
MC@NLO	15-60	CTEQ6.6	1.499	$2 \times p_T > 3\,\text{GeV}$ $2 \times \lvert\eta\rvert < 2.7$	113712	0.402	1M	1.66

Table 5.1: *Table of MC10 di-muon Monte Carlo signal samples used in the analysis, their corresponding mass range, generated cross section σ_{tot}, details of the lepton filters applied, including the filter efficiencies ϵ_{filter}, the number of events generated, and the total effective luminosity of the sample. The cross section used in the analysis for dataset number 106047 is 0.99 nb. This number takes into account a single NNLO k-factor estimated using FEWZ [14].*

Higher Order Corrections

As already discussed in Section 1.4.1, the leading order cross section for the Drell-Yan process must be corrected for the higher order QCD contribution due to interaction with gluons. Particularly at low values of the di-lepton invariant mass, the Pythia LO cross section is underestimated. The MC@NLO samples listed in Table 5.1 are used at the generator level only and for theoretical predictions; this is because the simulation setup used to produce these samples is compatible only with analyses on 2011 data.

Correction factors (k-factors) to be applied both to LO and NLO simulated event samples have been calculated analytically and give the prediction for higher order cross sections.

By setting the running coupling $\alpha_s = \alpha_s(M_Z) = 0.118$, and by choosing a set of PDFs as inputs to the perturbative matrix element calculation, the k-factors used are defined as:

$$k_{NLO}(\text{MRSTLO}^*) = \frac{\sigma_{NLO}(\text{PDF} = \text{MSTWNLO})}{\sigma_{LO}(\text{PDF} = \text{MRSTLO}^*)}, \tag{5.2}$$

$$k_{NNLO}(\text{MRSTLO}^*) = \frac{\sigma_{NNLO}(\text{PDF} = \text{MSTWNNLO})}{\sigma_{LO}(\text{PDF} = \text{MRSTLO}^*)}, \tag{5.3}$$

$$k_{NNLO}(\text{CTEQ6.6}) = \frac{\sigma_{NNLO}(\text{PDF} = \text{MSTWNNLO})}{\sigma_{NLO}(\text{PDF} = \text{CTEQ6.6})}, \tag{5.4}$$

where σ_{NLO} is the NLO matrix element calculation for a differential or integrated cross section; MSTWNLO refers to the MSTWNLO PDF set [55], and MRSTLO* refers to the LO MSTW PDF set which uses LO Monte Carlo generators but additionally mimics the NLO effects by modifying the LO PDFs. This is done by using α_S at NLO and violating the momentum sum-rule [56]. The MRSTLO** PDF set is also a modification of the LO PDFs in which the p_T^2 is used rather than Q^2 as scale in α_S evolution [56].

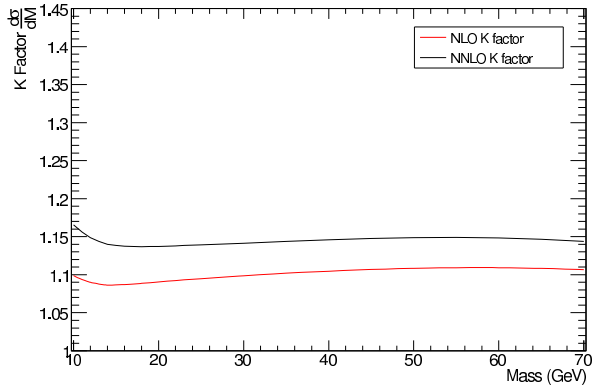

(a) k_{NLO}(MRSTLO*) and k_{NNLO}(MRSTLO*) for $d\sigma/dM$

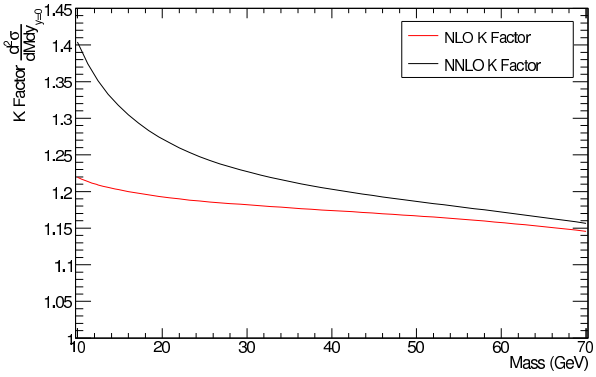

(b) k_{NLO}(MRSTLO*) and k_{NNLO}(MRSTLO*) for $d^2\sigma/dMdY|_{Y=0}$

Figure 5.1: *The NLO and NNLO k-factors determined [11] using the* VRAP *program.*

In this analysis the VRAP program is used to provide k-factors in order to correct the signal LO MC samples to have an adequate NNLO description of the cross section. Note that VRAP is only able to perform calculations at the Born level (a Born lepton is defined in simulated event samples as a generator level lepton before

QED radiation effects are taken into account), and in the whole phase space i.e. using VRAP it is not possible to restrict the calculation within some defined fiducial volume. VRAP computes the cross section as a function of mass and rapidity of the di-lepton pair in a fine 2D grid. The parameterised k-factor predictions are then applied to the signal MC samples, event by event depending on the mass and rapidity of the generator Born level vector boson Z/γ^*. The weighting functions are tested to be accurate to 0.06% [11] (See also [57]) in the region of phase space with $M > 10\,\text{GeV}$ and $|Y| < 3.5$ which is within the phase space of the analysis.

The NLO and NNLO k-factors computed in VRAP for $d\sigma/dM$ and $d^2\sigma/dMdY$ (at fixed rapidity of the vector boson $Y = 0$) are shown in Figure 5.1. As already predicted the biggest effect to the cross section is in the low di-lepton invariant mass region where the NNLO correction can be as large as 18% and 40% in $d\sigma/dM$ and $d^2\sigma/dMdY$ respectively. The final k-factor corrections applied in the analysis have been calculated elsewhere [11]. Details of the k-factors extrapolations can be found in [58].

For the Z sample listed in Table 5.1 (dataset 106047) and generated for masses of the di-muon pair above 60 GeV, the k-factor (independent of the vector boson mass) is obtained from the program FEWZ [14] at NNLO using MSTW2008NLO PDFs. Therefore one single scale factor equal to 1.157 is used for this sample for all values of mass and rapidity of the generated vector boson [59].

Figure 5.2 shows the invariant mass spectrum, between 12 and 66 GeV, of the di-muon system, after the full selection described in Section 5.2 is applied. Here only the two Pythia Drell-Yan signal MC samples (datasets 113700 and 113701 generated between 8 and 15 GeV and 15 and 60 GeV respectively) are used, since these are the only samples which are corrected using the k-factors. The violet region shows the effect of the k-factors applied to the LO samples (the contribution of the latter is shown in red). A ratio of NNLO to LO predictions is also shown. At low masses the effect reaches about 30%.

5.1.3 Background contributions to the DY process

There are a number of physics processes likely to occur in pp collisions that will produce two (or more) muons in the final state and therefore fake a DY-like process in the detector and also in the selection. All such events passing the signal selection criteria are considered as background and contribute to the cross section determination.

Heavy flavour QCD background. The largest contribution to the Drell-Yan analysis in the di-muon channel, particularly in the low-mass region, are the QCD

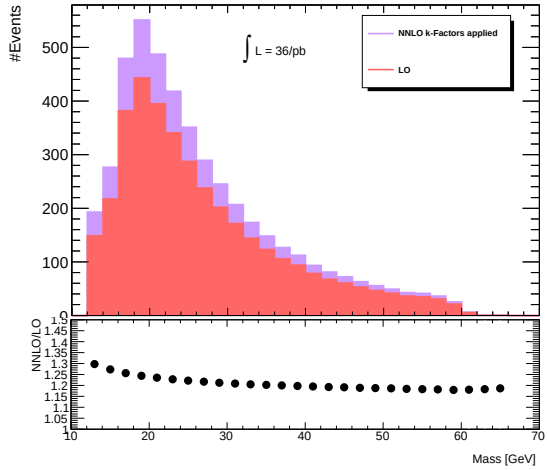

Figure 5.2: *The LO mass spectrum of the di-muon system is shown in red. The effect of the k-factor corrections is shown in violet or more quantitatively in the ratio in the lower part of the figure.*

heavy flavour $c\bar{c}$ and $b\bar{b}$ channels, where muons are produced in the leptonic decays of the c and b hadrons. Although the probability of heavy flavour hadron decays within jets giving at least two (most of the time real) muons in the final state is low, the cross section of their production at the LHC is at least 100 times larger than the DY cross section. A hadron from a heavy quark decays leptonically about 10% of the time, producing a lepton and an additional hadron or even two leptons. Therefore these events are the dominant background source to the low mass DY analyses.

There are ways of identifying and therefore rejecting muons coming from heavy flavour type events. Muons originated in the hard interaction will be isolated in the detector, typically with very little additional energy around their trajectory. A muon from a heavy flavour type event will not be isolated as it will have a close by jet due to the hadron coming from the decay of the heavy flavour quark and the hadrons from the remainder of the jet. These non-isolated background events can be distinguished from DY events and therefore rejected.

Light flavour QCD background. In the low mass region, in addition to jets originating from heavy flavour QCD processes, light flavour parton (u, d, s quarks and gluons) contributions must also be considered as a background. These are QCD processes resulting in π and K meson decays and the contribution to the Drell-Yan background is mostly due to non-prompt muons. The details about the optimisation of the analysis in order to reduce the QCD heavy flavour and light flavour backgrounds are discussed in Section 5.4.

Electroweak background. Minor contributions to the background are also given by Electroweak (EWK) decays with μ and τ leptons in the final state. The production of a $\tau^+\tau^-$ pair from the Z/γ^* decay is another DY process with the same probability as $\mu^+\mu^-$. Both taus can decay leptonically to muons, $\tau^+\tau^- \rightarrow \mu^+\nu_\mu\bar{\nu}_\tau\mu^-\bar{\nu}_\mu\nu_\tau$. This is the second most dominant source of background to the low mass Drell-Yan analysis in the di-muon channel. The $W \rightarrow \mu\nu$ process is also considered in the analysis although its contribution is almost negligible in the low di-muon pair mass region.

Upsilon background. Another potential source of background events is the high-mass tail of the upsilon resonance, as the lower mass range of the analysis is 12 GeV, while the upsilon masses are between 9 and 11 GeV.

The MC samples describing the backgrounds considered in the analysis are listed in Table 5.2. The light flavour QCD contribution is extracted directly from data and no MC sample has been used to simulate these processes.

Generator	Process	Filters	Dataset	N Events	σ_{eff}[nb]	$\mathcal{L}$[fb^{-1}]
PythiaB	$c\bar{c}$	2 $\times$ $p_T > 4$ GeV $\lvert\eta\rvert < 2.5$	108487	1M	16.0	0.06
PythiaB	$b\bar{b}$	2 $\times$ $p_T > 4$ GeV $\lvert\eta\rvert < 2.5$	108488	2M	89.0	0.02
Pythia	$Z \rightarrow \tau\tau$ $M > 60$	–	106052	2M	0.99	2.02
Pythia	$Z/\gamma^* \rightarrow \tau\tau$ $10 < M < 60$	–	107055	2M	3.45	0.58
Pythia	$W \rightarrow \mu\nu$	–	106044	7M	8.94	0.78
Pythia	$\Upsilon(1S) \rightarrow \mu\mu$	–	108491	0.5M	69.1	0.007
Pythia	$\Upsilon(2S) \rightarrow \mu\mu$	–	108492	0.5M	23.9	0.02
Pythia	$\Upsilon(3S) \rightarrow \mu\mu$	–	108493	0.5M	25.8	0.02

Table 5.2: *MC background samples used in the analysis.*

5.2 Event Selection

The selection criteria adopted in the low mass Drell-Yan analysis of the 2010 ATLAS data, in order to study the physics process in the di-muon channel has been optimised in order to maximise the signal efficiency, and at the same time discarding the maximum number of background events. In this section a full description and motivation of the selection criteria is described.

5.2.1 Muon Selection and cut flow

The first selection on data is done by rejecting events excluded by the GRL, such that good quality events are left for physics analysis. The GRL selection is not applied on simulated events. In all events in which at least one primary vertex is reconstructed with a minimum of three tracks fitted to it, a minimum number of two combined muons reconstructed by the `Muid` algorithm is required. A trigger requirement is applied on data (see Section 5.5.2 where a motivation for not requiring the trigger on simulated event samples is detailed). Selected events are then required to fulfil the Muon Combined Performance track quality requirements optimised for `ATHENA` release 16 analyses [48]. These criteria are associated to the inner detector tracks and ensure that only muons with good ID tracks are selected. Furthermore, the selected events must contain two oppositely charge muons (if more than one pair exists the first two muons with opposite charge and higher p_T are selected). The muon with higher p_T, also called "leading muon" (LM) is required to have a minimum p_T of 9 GeV, the other muon, or second muon (OM) to have a minimum p_T of 6 GeV. Both muons are required to be in the acceptance region of the muon trigger system and therefore to be reconstructed with $|\eta| < 2.4$, and to satisfy the very tight isolation requirement `PtRatio60`[1] < 0.08. In addition the muon pair is required to have an invariant mass between 12 GeV and 66 GeV. In summary the selection is as follows:

- Preselection:
  - GRL (data only, details can be found in Section 4.2),
  - at least one primary vertex with at least three tracks fitted to it,
  - at least two combined `Muid` muons (the parameters used are always the ones of the combined muons),
  - trigger `EF_2mu4_DiMu` (data only, the simulated event samples are scaled by the trigger efficiency measured in data),
- Good quality muons (see Section 4.4.1),
- $p_T(LM) > 9$ GeV, $p_T(OM) > 6$ GeV and $|\eta| < 2.4$ for both muons,
- opposite sign muons (OS),
- $12 < M < 66$ GeV,

[1] The definition of the isolation variables is given in Section 5.4.1

- `PtRatio60` < 0.08 (both muons).

In Table 5.3 a cut flow showing the estimated number of signal and background events passing each of the main selection criteria is shown for each MC sample and for data.

Cut	Data	Drell-Yan	QCD	$Z \to \tau\tau$ $M > 60$ GeV	$Z/\gamma \to \tau\tau$ $10 < M < 60$ GeV	$W \to \mu\nu$	$\Upsilon \to \mu\mu$	Total MC
Preselection	1026519	30257	415120	279	51	680	512129	958516
Good quality muons	948836	29341	369489	267	48	579	495545	895269
$p_T, \lvert\eta\rvert$	130706	17864	142693	206	14	271	17859	178907
OS	129133	17851	76373	201	13	198	17718	112354
$12 < M < 66$ GeV	51958	6645	44754	191	12	152	161	51915
Isolation	**6109**	**4895**	**1009**	**137**	**7**	**14**	**34**	**6096**

Table 5.3: *Cut flow table for low-mass Drell-Yan di-muon selection with 2010 data.*

In Table 5.4 the percentage of events passing each selection criterion are given, relative to the preceding selection criterion.

Cut	Data	Drell-Yan	QCD	$Z \to \tau\tau$ $M > 60$ GeV	$Z/\gamma \to \tau\tau$ $10 < M < 60$ GeV	$W \to \mu\nu$	$\Upsilon \to \mu\mu$
Preselection	-	-	-	-	-	-	-
Good quality muons	92.4	97.0	89.0	95.7	95.0	85.1	96.8
$p_T, \lvert\eta\rvert$	13.8	63.2	38.6	77.2	29.2	46.8	3.6
OS	98.8	99.9	53.3	97.5	92.9	72.7	99.2
$12 < M < 66$ GeV	40.2	34.0	58.6	95.3	92.3	77.2	0.9
Isolation	11.8	73.7	2.3	71.4	58.3	9.2	21.1

Table 5.4: *Cut flow table showing the percentage of events passing each cut, for low-mass Drell-Yan di-muon selection with 2010 data. The percentage is with respect to the previous cut.*

The "Good quality muon" requirements have rather small impact on all MC samples. The p_T and η criteria have a larger impact on all samples, especially on the low mass samples such as the upsilon MC samples, for which low p_T muons contribute the most. The requirement that the muons are oppositely charged reduces the QCD background by about a factor of two, as expected since this source of background should have equal probability to produce opposite sign and same sign lepton pairs. The $W \to \mu\nu$ sample also has a significant reduction due to the OS requirement, while all other MC samples are almost 100% efficient with respect to this selection, as expected. The restriction of the mass range between 12 and 66 GeV has a large impact on the upsilon tail. Also the Drell-Yan sample is reduced considerably, mostly due to the low mass sample (dataset 113700) which is generated

above 8 GeV in mass, and to the Z sample (dataset 106047) which has most of the events concentrated around the Z peak. The isolation efficiency keeps a large amount of signal compared to the QCD background which is largely reduced by this requirement. The ratio between the total number of signal events and the total number of background events selected is 4.1.

5.3 Pile-up Reweighting

The LHC operation at high instantaneous luminosities results in several proton-proton interactions in every bunch crossing [60]. Each "interesting" physics event recorded by ATLAS therefore contains additional particles coming from several other proton-proton interactions and which represent a source of background. As the instantaneous luminosity delivered by the LHC increases, the average number of interactions per bunch crossing also increases, the correlation between the two being linear. Therefore the number of interaction vertices per event increases. The vertex corresponding to the interesting interaction and all other pile-up vertices are collectively call primary vertices (PVs). The hard interaction is assumed to be the one corresponding to the PV for which the sum of the momentum of all of the tracks fitted to it is maximum. Figure 5.3 shows an event display of ATLAS (2011). The event has 11 reconstructed vertices.

A pile-up model is included in MC samples, that covers the whole range of PV multiplicities observed in data. Therefore the distribution of the number of primary vertices in simulated events is weighted to describe the one observed in data.

The analysis adopts the weighting procedure used widely in 2010 ATLAS analyses [61]. An event weight is computed for each event following a minimal selection. This includes the requirement that the trigger has fired[2], the number of tracks fitted to the primary vertex is at least equal to three and that the event contains at least two oppositely charged `Muid` muons.

The weights are determined by considering the number of vertices distribution in data and dividing this by the corresponding distribution in MC samples. Because of the rapid increase of the instantaneous luminosity, a set of weights is obtained for periods $E + F$ [3], G, H and I. Moreover because of the linear dependence of the pile-up with the luminosity, the final weights are defined to be the luminosity weighted average of the periods above. Figure 5.4 shows the distribution of the number of vertices in data and MC samples, before (a) and after (b) the simulated

[2]This requirement is only applied on data, the trigger efficiency measured on data is applied on each simulated event samples.

[3]Periods E and F are combined in order to have a reasonable statistical uncertainty.

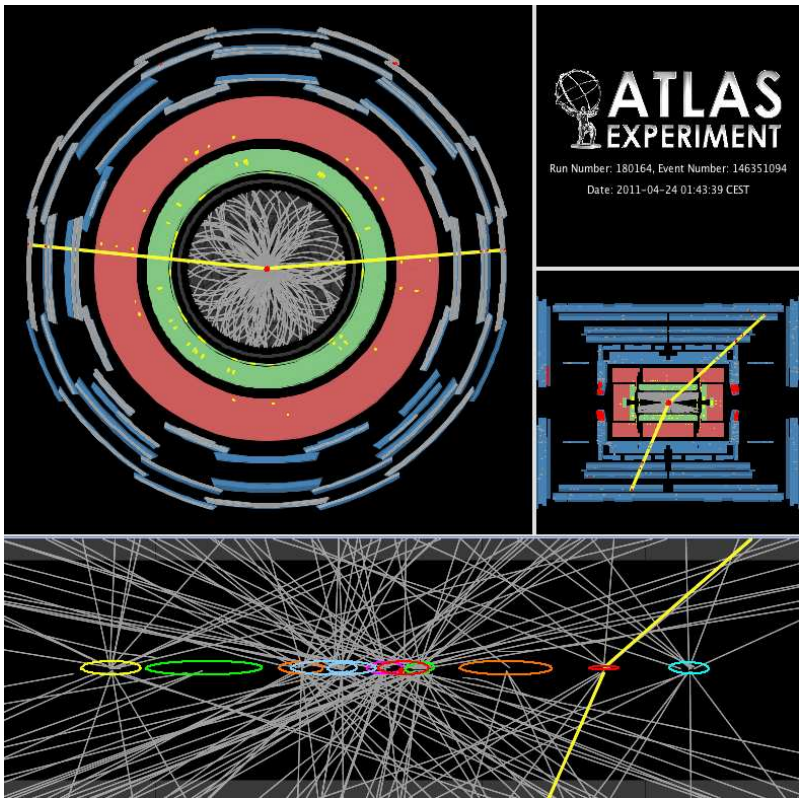

Figure 5.3: *Event display from the 24th of April showing a Z boson candidate decay in the di-muon channel. The di-lepton invariant mass is 93.4 GeV. The number of reconstructed vertices in this event is 11 [12].*

event samples has been re-weighted. As an example the MC sample shown in the Figure is the PYTHIA Drell-Yan sample (dataset 113701) and it is compared to data period I. The weights obtained for each MC sample as a function of the number of primary vertices reconstructed in the event are shown in (c) for data period I.

5.4 Isolation study and QCD background normalisation

As already mentioned in Section 5.1.3 at low di-muon invariant masses the dominant background to the Drell-Yan process is from QCD processes where muons are generated from the decay of b and c mesons. The PYTHIA predictions are thought to describe the shape of these processes moderately well, but not the overall normalisation. In order to correctly estimate the background contribution from QCD, a data-driven technique is performed by normalising the QCD background to the non-isolated region in data which is QCD background dominated. The suppression

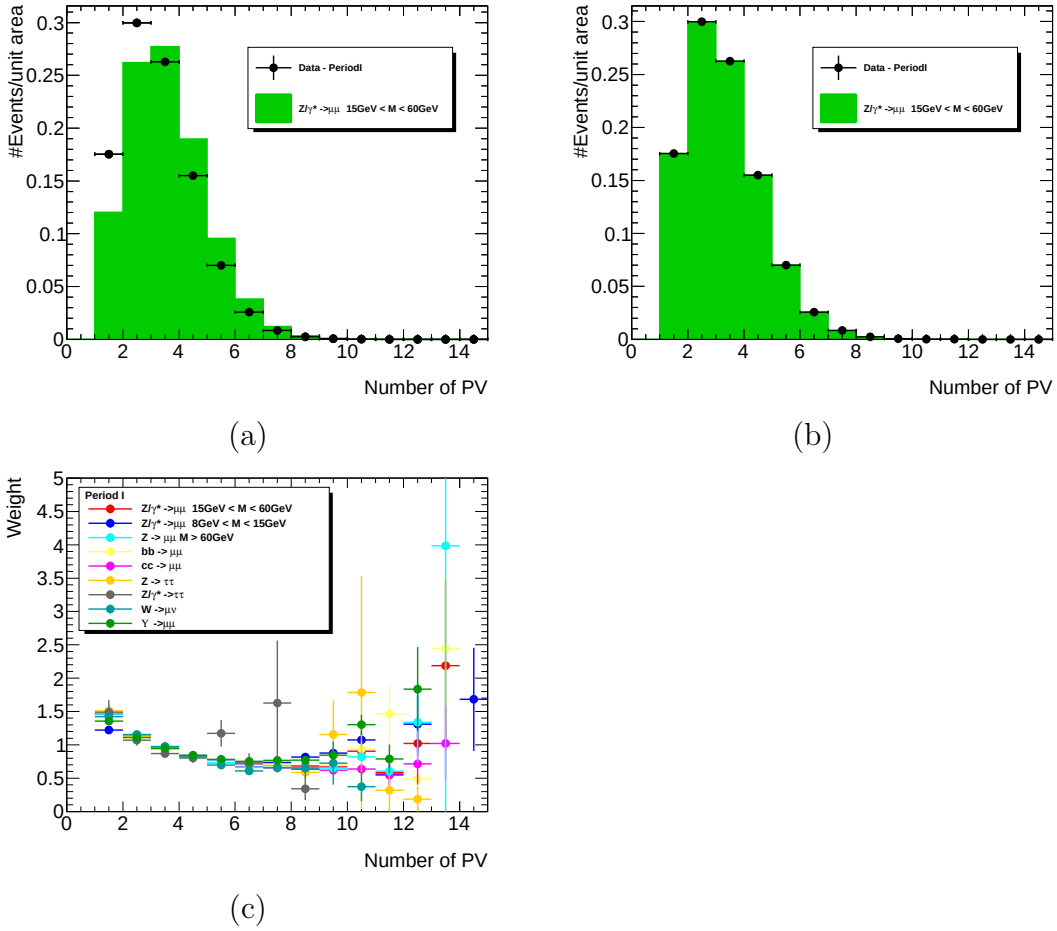

Figure 5.4: *Example of original pile-up description in data and MC samples (a), and after applying the weights (b). In (c) the weights determined for each simulated process in period I are shown collectively.*

techniques to reject the QCD background rely on the fact that leptons in QCD processes are produced in hadronic jets. Therefore they are not isolated, unlike the leptons from Drell-Yan signal events which are expected to be well isolated, but which can be spoilt by pile-up and QCD recoil activity from the same hard sub-process.

5.4.1 Isolation variable and pile-up

The muon isolation variables used for QCD background suppression are defined in the inner detector as well as in the calorimeter. A hollow cone is defined around the candidate muon. The inner cone is designed to collect the muon energy (and its energy loss) while the energy deposited between the inner cone and the outer cone, called the isolation energy, corresponds to the transverse energy deposited in

the electromagnetic calorimeter by tracks around the muon:

$$\texttt{etConeX} = \sum_{\Delta R = X/100} E_{T,EM} - \sum_{\Delta R = 0.05} E_{T,EM},$$

where $\Delta R = \sqrt{(\Delta\eta)^2 + (\Delta\phi)^2}$ defines the size of the cone and $\sum_{\Delta R=X/100} E_{T,EM}$ the sum of the energy in a cone of radius $X/100$. Similarly in the inner detector a variable is defined where instead the inner cone contains the muon track transverse momentum, and the outer cone the sum of transverse track momenta:

$$\texttt{ptConeX} = \sum_{\Delta R = X/100} p_{T,ID} - \sum_{\Delta R = 0.05} p_{T,ID},$$

where $\sum_{\Delta R=X/100} p_{T,ID}$ is the sum of transverse momentum of inner detector tracks in a cone of radius X/100. All the tracks which are considered to contribute to the outer cone are required to fulfil the following requirements:

- $p_T \geq 1\,\text{GeV}$,
- $|d_0| \leq 10\,\text{mm}$ (with respect to the interaction point),
- $|z_0|$[4] $\leq 10\,\text{mm}$ (with respect to the interaction point),
- $|z_{0,\text{origin}}| \leq 10\,\text{mm}$ (with respect to the origin of the ATLAS coordinate system),
- Number of Silicon Hits (Pixel + SCT) ≥ 4,
- If the pair of muons "a" and "b" is selected, and the track corresponding to muon "a" falls within the cone defined around muon "b", then the transverse momentum of muon "a" is subtracted from the sum.

The ratio of these variables with respect to the p_T of the muon is defined as:

$$\texttt{PtRatioX} = \frac{\texttt{ptConeX}}{p_{T,\mu}} \quad \text{and} \quad \texttt{EtRatioX} = \frac{\texttt{etConeX}}{p_{T,\mu}}.$$

The isolation variable used in the event selection is `PtRatio60` with $\Delta R = 0.60$.

Although the pile-up conditions during the 2010 data taking period were modest, pile-up has an effect on some of the isolation variables as can be seen by looking at the mean isolation as a function of the number of vertices in the event. This is shown in Figure 5.5(a) for data and 5.5(b) for simulated events; cones of $\Delta R = 0.40$

[4]The impact parameters z_0 is defined as the distance of closest approach of the muon track along the z-axis.

and $\Delta R = 0.60$ are considered for this study. The details of the fitted linear slopes are given in Table 5.5. The comparison between the slopes in data and simulated event samples shows that the calorimetric isolation variables are sensitive to pile-up and least well described; in contrast the relative track based isolation variables are insensitive to pile-up even with large cone size. This justifies the use of the `PtRatio60` isolation variable.

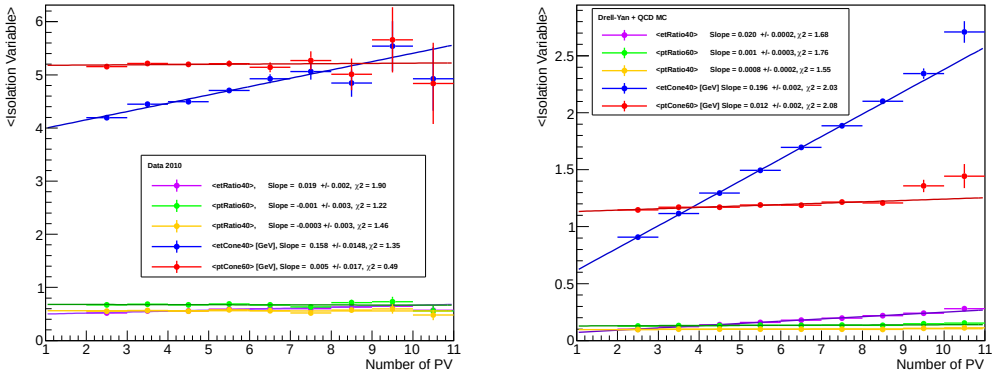

(a) Data (2010) (b) MC samples (2010)

Figure 5.5: *Mean isolation variables are shown as a function of the number of primary vertices for data (a) and MC samples (b). For each variable tested, the legend shows the value of the slope for the pile-up dependence. These results are also reported in Table 5.5.*

Isolation	ΔR	Data slope	χ^2/ndf	MC slope	χ^2/ndf
$\langle$`EtRatio40`$\rangle$	0.4	0.019 ± 0.002	1.90	0.0200 ± 0.0002	1.68
$\langle$`PtRatio60`$\rangle$	0.6	-0.011 ± 0.003	1.22	0.0010 ± 0.0003	1.76
$\langle$`PtRatio40`$\rangle$	0.4	0.000 ± 0.003	1.46	0.0008 ± 0.0002	1.55
$\langle$`EtCone40`$\rangle$ [GeV]	0.4	0.158 ± 0.015	1.35	0.1960 ± 0.0020	2.03
$\langle$`PtCone60`$\rangle$ [GeV]	0.6	0.005 ± 0.017	0.49	0.0120 ± 0.0020	2.08

Table 5.5: *Dependence of the mean isolation variable on the number of primary vertices.*

5.4.2 Isolation criteria optimisation

The lepton isolation requirements have a large impact on the QCD background rejection. However very harsh requirements also lower the signal efficiency. In Figure 5.6, each configuration of isolation variables `PtCone60` and `PtRatio60` is investigated by plotting the signal efficiency as a function of the maximum achievable background

rejection. The optimal isolation requirement is chosen to be `PtRatio60 < 0.08`. Using this value a 73% signal efficiency and 96% background rejection is achieved, with a signal over background ratio of about four. This is shown in Figure 5.6(b).

Note that this study has been performed with QCD heavy flavour MC samples only, and before the QCD normalisation study with the introduction of the light flavour QCD contribution. Moreover, the study was performed using a symmetric minimum p_T requirements on the two muons of 6 GeV. Nevertheless, the overall dependence of the background rejection from the signal efficiency is still valid. The analysis could be improved by requiring asymmetric minimum p_T on the two muons of 6 and 9 GeV, but has been left for reasons of time.

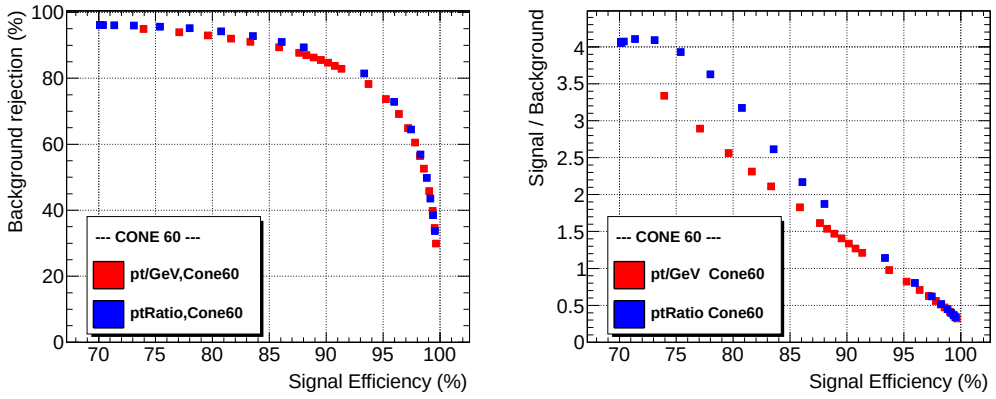

(a) (b)

Figure 5.6: *Signal Efficiency versus background rejection (a), and signal over background ratio (b), shown for the* `PtCone60` *and* `PtRatio60` *variables, and a selection of cut values.*

5.4.3 QCD Normalisation

To provide a reliable estimate of the selected number of background events from QCD processes, the first test to be performed is the comparison of the isolation variable `PtRatio60` distribution before the isolation criteria is applied, between data and MC samples. Figures 5.7(a), 5.7(d) and 5.7(g) show the comparison for different choices of cone size i.e. $\Delta R = 0.6, 0.4, 0.2$ for muons of 6 GeV minimum p_T. A large discrepancy between the shapes in data and simulated event samples is observed for all cone sizes. The same comparison has been repeated for increasing muon minimum p_T of 12 and 18 GeV and it is shown in Figures 5.7(b), 5.7(e) and 5.7(h) ($p_T > 12$ GeV) and 5.7(c), 5.7(f) and 5.7(i) ($p_T > 18$ GeV). As can be seen the discrepancy arises from the low-p_T muons in the range $6 < p_T < 12$ GeV whereas

high-p_T muons are well described by heavy flavour $c\bar{c}$ and $b\bar{b}$ PYTHIA MC samples. Note that the minimum p_T requirement is applied to both selected muons in each event, however only the contributions of the leading muon ($Mu1$) is shown in the figure. In each plot of Figure 5.7 the overall QCD normalisation is determined by inverting the isolation cut used in the analysis (the region `PtRatio60 >` 0.08 is QCD dominated) on both muons and normalising the MC samples to data. Note that since a minimum amount of signal and other MC samples fall in the non-isolated region, these are subtracted from data.

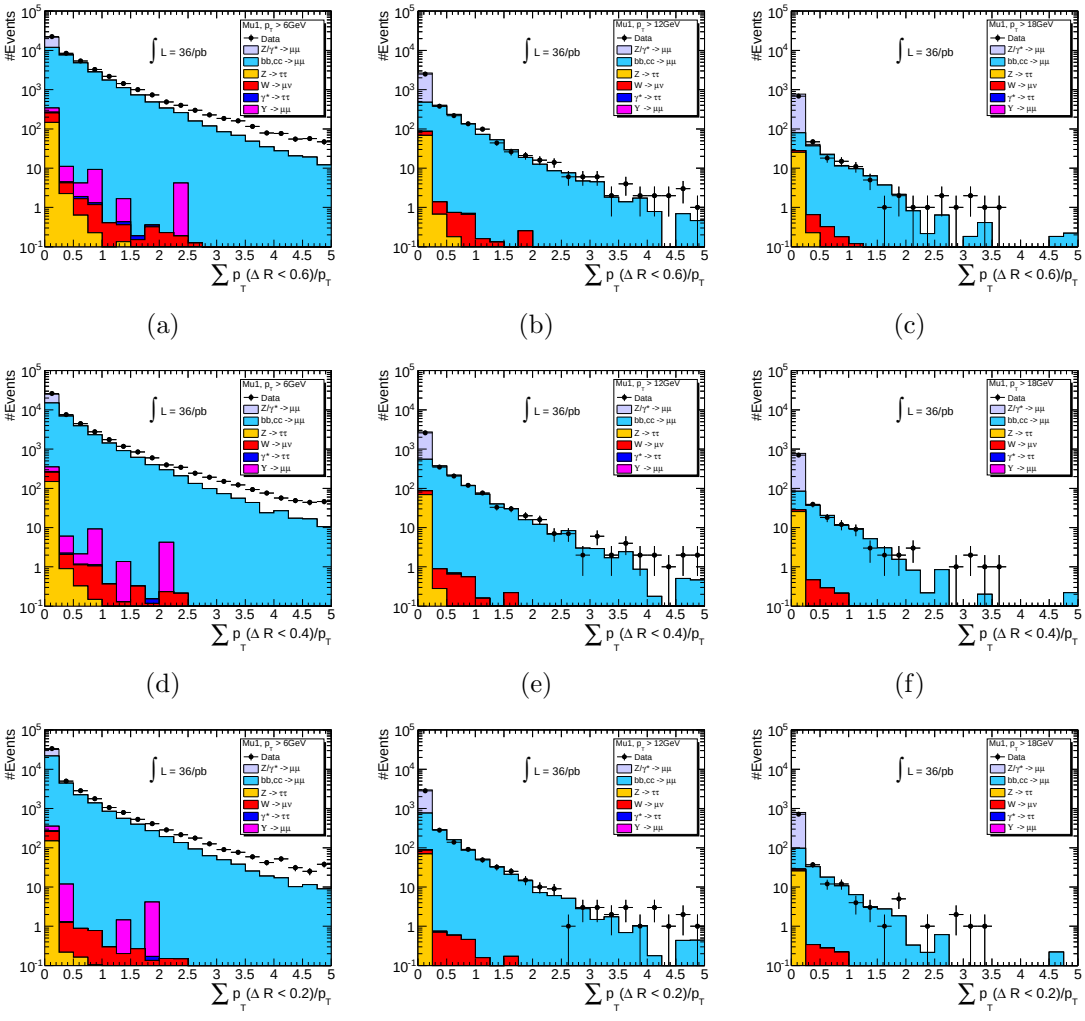

Figure 5.7: `PtRatio` *distribution for muons with* p_T *above* 6 *GeV (a), (d), (g),* 12 *GeV (b), (e), (h) and* 18 *GeV (c), (f), (i). In the first row the cone size used is* $\Delta R = 0.6$*, in the second is* $\Delta R = 0.4$ *and in the third is* $\Delta R = 0.2$*. Note the extended range over which the distributions are shown.*

The discrepancy is due to the missing contribution from light flavour (u, d, s)

interactions which are generated in QCD processes resulting in π and K meson decays. This sample of events is derived from data. Under the assumption that there is no preference for the light flavour background to contain Opposite Sign (OS) or Same Sign (SS) muon pairs, the SS component of data is considered as a proxy for the OS contribution from light flavour QCD.[5]

To ensure that the overall heavy flavour and light flavour QCD background is well described in particular for the isolation variable `PtRatio60`, the following method has been implemented.

A pure sample of QCD events is selected in data by applying the full selection except for the isolation cut. One of the muons is required to satisfy a *harsh anti-isolation* requirement `PtRatio60` > 1.0 such that no signal events are included in this sample. The other muon is not required to pass any isolation requirement. The choice of the anti-isolated muon is made randomly from the pair in order to avoid any correlations in p_T, η, or charge. This sample of events represents an unbiased estimate of the QCD background and the contribution in the isolation spectrum given by the other muon is over the full `PtRatio60` range down to zero.

The light flavour sample contributing to the `PtRatio60` distribution is given by the *harsh anti-isolated* SS data (N^{SS}_{data}) while the heavy flavour distribution of `PtRatio60` from *harsh anti-isolated* OS b and c simulated events.

However, the SS data sample N^{SS}_{data} includes heavy flavour and light flavour contributions. In order to avoid a double counting of the heavy flavour piece (from MC samples and data), the heavy flavour SS component from the MC samples is removed from the template such that the heavy flavour contributions is given by $N^{OS}_{b,cMC} - N^{SS}_{b,cMC}$.[6]

The relative fractions of b, c simulated event samples and SS data required to describe the entire `PtRatio60` spectrum for OS pairs are constrained such that:

$$N^{OS}_{data} = f_1 \cdot (N^{OS}_{b,cMC} - N^{SS}_{b,cMC}) + f_2 \cdot N^{SS}_{data}\,, \tag{5.5}$$

where f_1 is the fraction of b, c MC sample to be considered, and f_2 is the light flavour fraction. The relative fractions f_1 and f_2 are determined in `ROOT` by doing a likelihood fit using the `TFractionFitter` fitting template. The shape of the QCD prediction is then fixed by the use of the fractions f_1, f_2. In Figure 5.8(a) the two

[5]Throughout the analysis OS samples are obtained using the `EF_2mu4_DiMu` trigger. This requires that the two muons that trigger the event are oppositely charged. In order to select SS samples a different trigger is required. This is the `EF_2mu6` trigger which has no requirements on the muon charge and collected the same integrated luminosity during period E to I in 2010 as the `EF_2mu4_DiMu`.

[6]The assumption is made that the fraction of OS to SS in the PYTHIA $cc + bb$ samples is well modelled.

templates provided to the `TFractionFitter` are shown: OS data distribution, light flavour contribution (data SS) and the b, c simulated event samples (QCD OS - QCD SS) contribution. Figure 5.8(b) shows the result of the fit and the overall good description of the `PtRatio60` distribution. The relative fractions $f_1 \cdot (N^{OS}_{b,cMC} - N^{SS}_{b,cMC})$ and $f_2 \cdot N^{SS}_{data}$, where $f_1 = 0.304$ and $f_2 = 0.696$, are also separately shown.

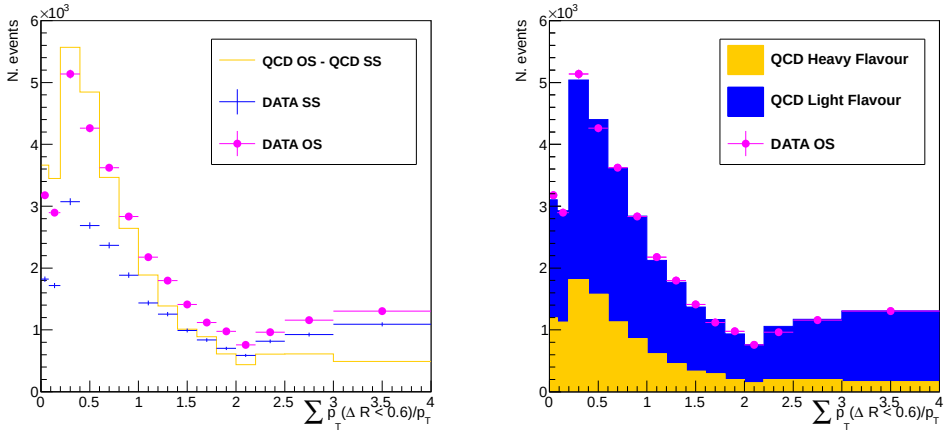

(a) (b)

Figure 5.8: *Figure (a) shows a comparison between* `PtRatio60` *spectrum for OS data, for the light flavour background (data SS), and the heavy flavour QCD background (QCD OS - QCD SS). The fit result is shown in (b).*

Once the shape of the QCD contribution is well described, an overall QCD normalisation factor to be applied to the MC samples, $\mathcal{N}$, is derived from the *non-isolated di-muon* selection in which all selection cuts are applied except the isolation, which is instead inverted for both muons, i.e. `PtRatio60` > 0.08. The *harsh anti-isolation* `PtRatio60` > 1.0 is dropped. The normalisation condition is expressed as:

$$\frac{N_{data} - N_{SigMC} - N_{EW,MC}}{[\mathcal{N} \cdot f_1 \cdot (N^{OS}_{b,cMC} - N^{SS}_{b,cMC})] + [f_2 \cdot N^{SS}_{data}]} = 1, \tag{5.6}$$

where N_{SigMC} and $N_{EW,MC}$ are the numbers of events predicted by the signal and EW background MC samples. In this way, the normalisation factor $\mathcal{N}$ is determined to be $\mathcal{N} = 0.75$.

After applying the normalisation factor the resulting `PtRatio60` spectrum is shown in Figure 5.9(a) for all events passing the analysis selection except the `PtRatio60` cut. As can be seen the discrepancy in shape visible in Figure 5.7(a) is no longer present, and a good overall agreement is achieved. Figure 5.9(b) shows the spectrum of the isolation variable for the *non-isolated* di-muon sample used to determine the overall QCD MC normalisation. Again good description is observed between data

and background.

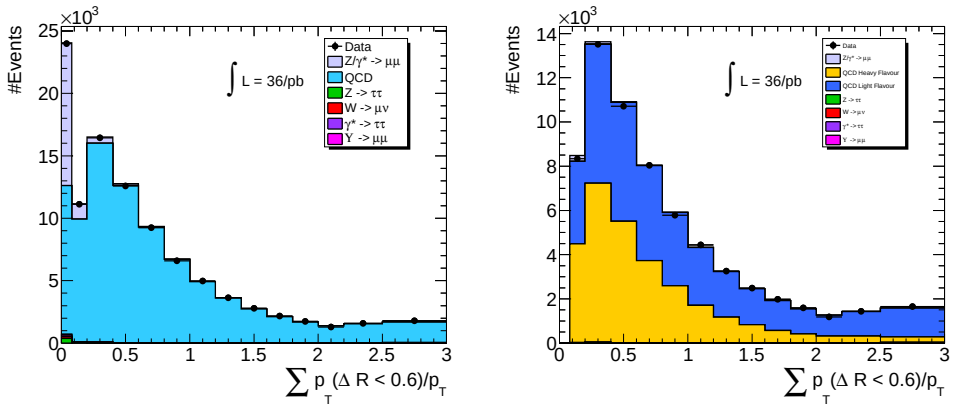

(a) (b)

Figure 5.9: *(a)* `PtRatio60` *for Data and MC samples, when all the analysis requirements have been applied except for the isolation requirement. The QCD contribution has been normalised using the method described in the text. (b)* `PtRatio60` *for data and MC samples, with the correct QCD normalisation applied after all selection, except for the isolation requirement. The inverted isolation cut* `PtRatio60` > 0.08 *is required instead.*

5.5 MC samples corrections

During the 2010 (and 2011) data taking period an intense program of calibration and understanding of the ATLAS detector has been performed. The data collected has been processed various times, in order to incorporate calibration and alignment corrections. Also the Monte Carlo simulations which mimic the detector activity have been accurately tuned to closely model its true response. However, a number of corrections to be applied to the simulated event samples still remain. These include differences in the modelling of pile-up, isolation efficiency, muon reconstruction and trigger efficiency.

The simulated event samples listed in Tables 5.1 and 5.2 were normalised to the integrated luminosity of the data sample. All of the corrections used in the analysis and the estimated uncertainties associated with them is described in what follows.

5.5.1 Isolation Efficiency

Due to the large QCD background in the low di-muon invariant mass region, the isolation criteria chosen in the analysis are extremely tight. Therefore the isolation efficiency and systematic uncertainty associated to it represent a critical aspect of

the analysis. A "tag and probe" data-driven method has been implemented following a similar study performed at the Z pole [62]. However, in the specific case of the low mass Drell-Yan analysis a clean sample of muons from the Z decay would not contain enough low p_T muons to be able to study the efficiency down to p_T of about 6 GeV due to a limited number of events available. Therefore the invariant mass range is selected to be wider and include the Drell-Yan spectrum. Making use of the QCD normalisation study discussed in Section 5.4.3, a background estimate is included and subtracted from the data, and believed to be well modelled. All other minor sources of background are also subtracted from data. The events are selected as follows:

- Minimum two `Muid` combined muons,
- at least one primary vertex with at least three tracks fitted to it,
- the event fires the `EF_2mu4_DiMu` trigger (for the estimation of the same sign background the `EF_2mu6` trigger is used instead).

In all events passing the above requirements, a "tag" muon is defined if it passes the following requirements:

- $p_T > 12\,\text{GeV}$,
- $|\eta| < 2.4$,
- $|z_0| < 10\,\text{mm}$,
- Good quality muon (see Section 4.4.1),
- `PtRatio60` < 0.08.

If the event is selected with at least one "tag" candidate, a "probe" muon is searched for, by requiring that the following criteria are satisfied:

- $p_T > 6\,\text{GeV}$,
- $|\eta| < 2.4$,
- $|z_0| < 10\,\text{mm}$,
- Good quality muon (see Section 4.4.1),
- opposite charge to tag,

- $|\Delta\phi(\text{tag}, \text{probe})| > 2\,\text{rad}$,
- $|\Delta z_0(\text{tag}, \text{probe})| < 3\,\text{mm}$,
- $|\Delta d_0(\text{tag}, \text{probe})| < 3\,\text{mm}$,
- $12 < M(\text{tag}, \text{probe}) < 110\,\text{GeV}$.

In the particular case of an event with two muons, both of which pass the tag selection, both combination of tag and probe are considered.

The efficiency of the isolation selection is defined as the number of probes passing the isolation requirement `PtRatio60` < 0.08, divided by the total number of probes selected:

$$\epsilon^{\text{iso}} = \frac{N(\text{isolated probes})}{N(\text{all probes})}. \tag{5.7}$$

Figure 5.10 shows the isolation efficiency as a function of the probe pseudo-rapidity, for both signal Monte Carlo simulations and background-subtracted data. In the figure a different discrepancy between the background-subtracted data and the signal MC samples in the Barrel region ($|\eta| < 1.05$) compared to the Endcaps ($|\eta| > 1.05$) is observed. Therefore the choice of performing the efficiency study as a function of p_T separately in the two regions of the detector.

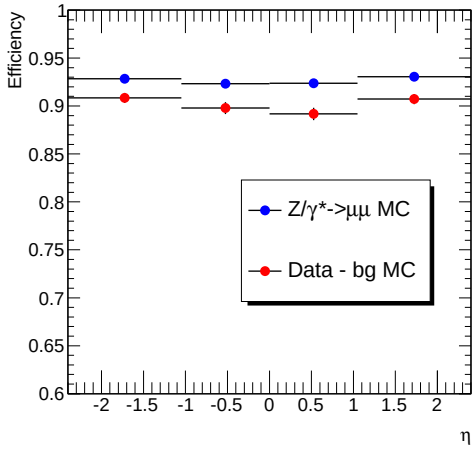

Figure 5.10: *Isolation efficiency for* `PtRatio60` < 0.08*, as function of* η *of the probe muon, for background-subtracted data and signal MC samples. Each* $|\eta|$ *region is divided in two bins, one corresponding to the Barrel and the other to the Endcap.*

In Figure 5.11 the isolation efficiency as a function of probe p_T is shown, for both the background-subtracted data and the signal MC samples. Figure 5.11(a)

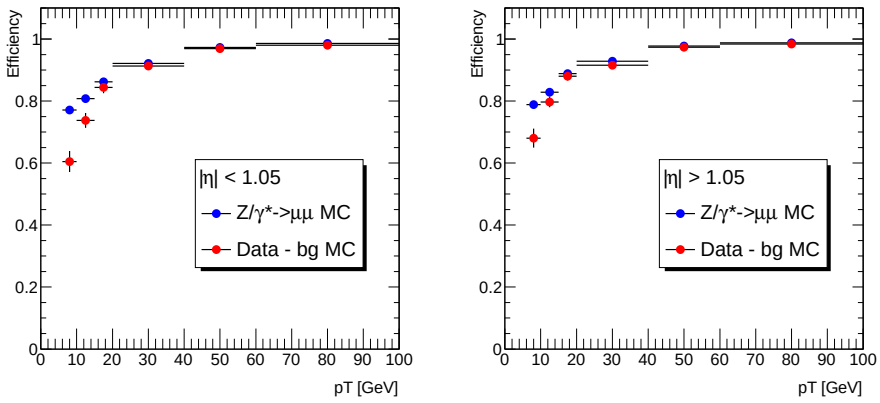

(a) (b)

Figure 5.11: *Isolation efficiency for* `PtRatio60` < 0.08 *as a function of* p_T*, for background-subtracted data and signal MC samples, in the Barrel (a), and Endcap (b) regions.*

corresponds to the Barrel region whereas Figure 5.11(b) shows the efficiency of muons reconstructed in the Endcaps. These efficiencies are used in the low mass Drell-Yan analysis ($12 < M < 66\,\text{GeV}$) by defining scale factors as the ratio between the background-subtracted data and the signal MC samples efficiencies. The scale factors are applied to each of the two muons selected in the signal MC samples in order to correct for any simulated event samples mis-modelling. The product of the two scale factors is then used as the isolation efficiency event weight.

The scale factors in bins of p_T are shown in Figure 5.12, both for the Barrel and Endcap regions; the shaded area represents the systematic uncertainty described in Section 5.6.2.

5.5.2 Trigger Efficiency

The requirement that the events are triggered by `EF_2mu4_DiMu` is not accounted for in the signal and background Monte Carlo simulations. Instead, as already mentioned, the trigger efficiency measured on data is applied to the MC samples. The problem that the trigger presented is related to the mis-identification of the muon charge in the `EF_mu4` part of the algorithm. Therefore, since the `EF_2mu4_DiMu` trigger is defined to select only oppositely charged muons, the matching could not be trusted. This problem is not present in data. Therefore instead of determining scale factors to correct for any differences, the trigger efficiency is derived directly from data and applied to the simulations.

The efficiency for the `EF_2mu4` part of the trigger is mapped in two variables,

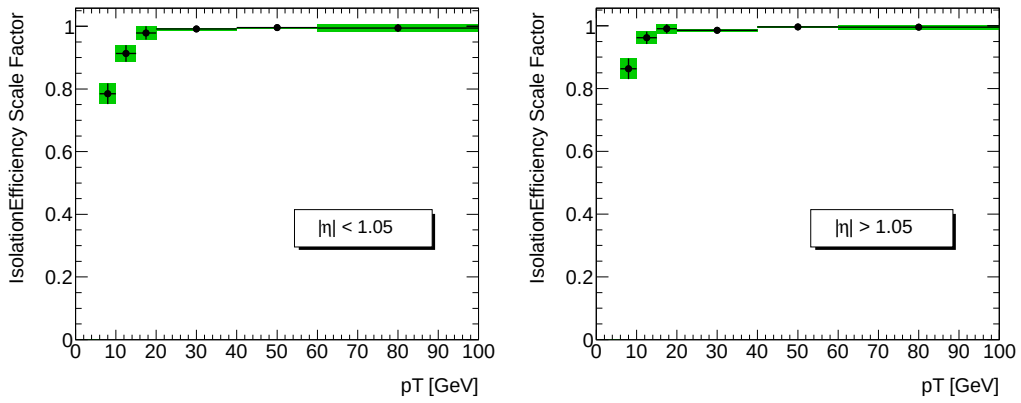

(a) (b)

Figure 5.12: *(a) and (b) show the isolation efficiency scale factor for* `PtRatio60`$<$ 0.08 *as a function of the muon* p_T*, for the Barrel and Endcap regions respectively.*

the p_T and $\eta \times Q$ of the muons, where Q is the muon charge. The remaining part of the trigger efficiency concerning the muon track fit to the vertex and opposite charge constraint (Vtx+OS) is applied as a function of the rapidity of the Z/γ^*.

The overall event trigger efficiency weight on MC samples is defined to be the product of the three efficiencies: `EF_mu4` efficiency applied to the leading muon, `EF_mu4` efficiency applied to the second muon, and the Vtx+OS efficiency applied once per event, as shown in Equation 4.7.

A detailed description of the trigger efficiency study is extensively presented in Chapter 4 by analysing each component of the algorithm.

5.5.3 Muon Momentum Resolution and Scale

An additional correction which must be applied to Monte Carlo simulations is the one that accounts for the mis-modelling of the muon momentum resolution and scale shifting during the reconstruction. The ATLAS collaboration performed early studies on this with muons from Z and $W^{\pm}$ decays in order to measure the difference in momentum scale and resolution between MC samples and data [63]. In this study the momentum resolution is measured from the width of the di-muon mass distribution in $Z \to \mu\mu$ decays and from the comparison with the individual ID and MS momentum determination for combined muons generated from $W \to \mu\nu_\mu$ decays. The measurement is performed on data as well as on simulated samples and smearing factors are obtained. These can be applied to simulated combined muons[7] through software routines which employ the method described in [63].

[7] *Muid* muons are used in the Drell-Yan analysis.

The values and accuracy of the smearing depend on which data and which reprocessing of data and MC samples is used. More recent analyses of the muon momentum resolution show that the agreement between data and simulated event samples has improved using more up-to-date alignment and calibration corrections.

Figure 5.13 shows the average difference of the p_T of the muon before and after the corrections are applied, as a function of the smeared muon p_T, for the Drell-Yan signal MC samples. The error bars show the RMS spread of the difference in p_T before and after the smearing is applied. The momentum scale does not affect the average difference in p_T. This is motivated by the fact that the scale factors determined in four distinct η regions ($|\eta| < 1.05, 1.05 < |\eta| < 1.7, 1.7 < |\eta| < 2.0, 2.0 < |\eta| < 2.4$) are greater than unity in some regions and smaller than unity in others, making the overall shift average to zero. An example of the effect of the muon momentum scale in different regions in shown in Figure 5.13(b).

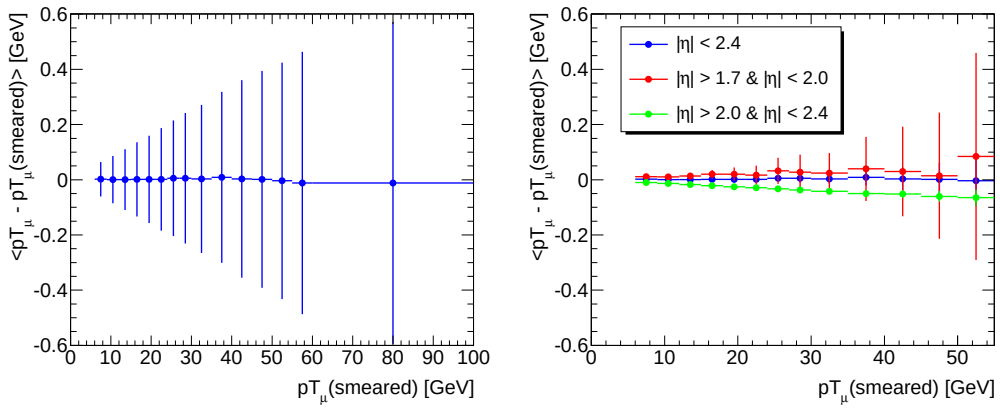

(a) (b)

Figure 5.13: *(a) effect of the p_T smearing and energy scale correction applied to the Drell-Yan signal MC samples. The error bars represent the RMS in each bin. (b) contribution of different η regions to the muon momentum scale.*

The selection presented in Section 5.2.1 is applied after the momentum smearing and scale shift is applied to each muon in the simulations.

5.5.4 Muon Reconstruction Efficiency

The reconstruction efficiency for the `Muid` algorithm has been studied elsewhere in ATLAS both for low p_T and high p_T muons [64, 65]. The study is based on the tag and probe method with $Z \to \mu^+\mu^-$, and $J/\psi \to \mu^+\mu^-$ decays from data and also using Monte Carlo simulations, in order for these to be appropriately correct for any differences. Scale factors have been determined as the ratio between data and

simulated event samples results and can be applied to correct the simulations of all signal and background samples for any efficiency differences.

The reconstruction of muons in the ATLAS detector depends on the muon transverse momentum, its charge (Q) and pseudo-rapidity. A software tool within the `ATHENA` framework is used to retrieve the scale factors as a two dimensional map of the muon p_T and η. The charge dependence of the efficiency has been studied and found to be well reproduced by the simulation. A strong charge asymmetry was only observed for muons with $p_T < 6\,\text{GeV}$. Since the Drell-Yan analysis only selects muons with $p_T > 6\,\text{GeV}$ the map has been implemented neglecting the charge dependence of the efficiency.

The scale factors are calculated after the p_T smearing and momentum scale have been applied to each muon; finally on an event basis the overall reconstruction scale factor to be applied is the product of the two weights determined separately for each muon.

Figure 5.14 shows the average scale factor (in blue) as a function of the muon p_T both in the Barrel (a) and Endcap (b) regions applied to the signal Monte Carlo simulations. Overall the MC samples describe the data very well, making the scale factors approximately equal to unity. However the corrections to be applied are different in the Barrel and in the Endcaps: in the Barrel the scale factors are everywhere closer to unity than in the Endcap region.

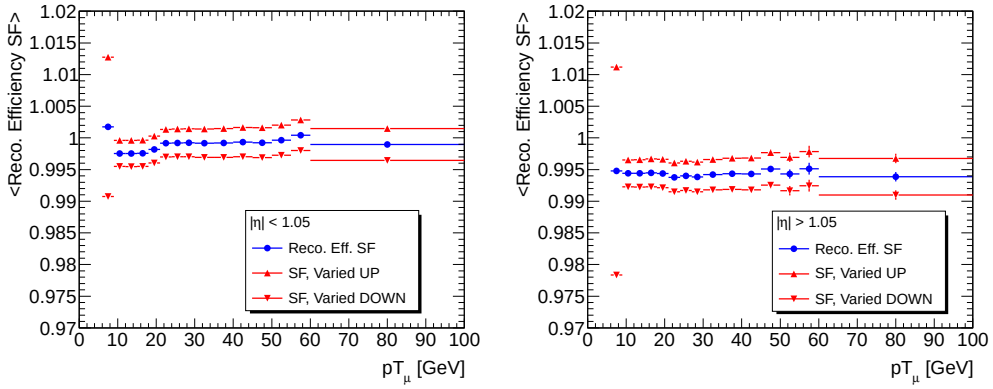

(a) Barrel (2010) (b) Endcap (2010)

Figure 5.14: *Average muon reconstruction efficiency Scale Factor, in bins of muon p_T, averaged over η.*

5.6 Systematic uncertainties

5.6.1 QCD background estimation

The uncertainty related to the normalisation of the QCD background has been estimated by comparing the data and MC samples di-muon mass spectrum in the *non-isolated region*, after applying the full selection except the isolation cut; instead both muons are required to pass the *non-isolation requirement* `PtRatio60` > 0.08. The comparison is shown in Figure 5.15(a). Figure. 5.15(b) shows the ratio of data over the total MC simulations. Although the maximum uncertainty is less than 5%, a conservative 10% uncertainty has been adopted for the QCD background estimation. This amply covers any deviations, and also accounts for any problems arising from the use of the 6 GeV threshold trigger for the SS samples, which is the same threshold as for the second muon p_T.

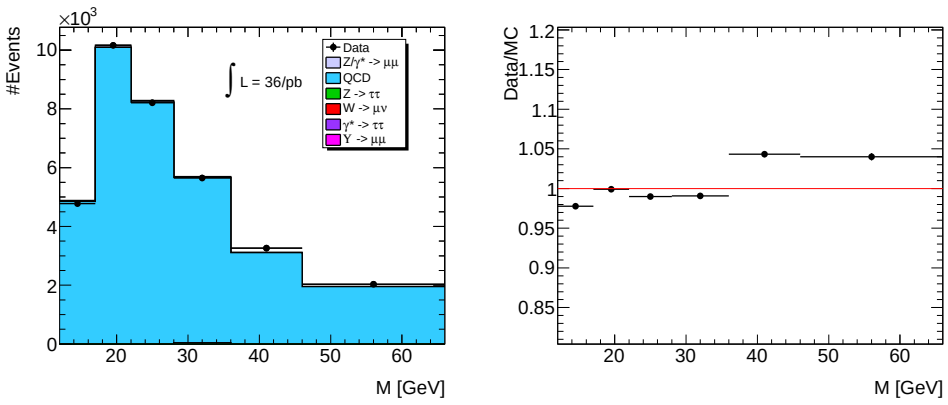

(a) (b)

Figure 5.15: *(a) Di-muon mass spectrum comparing data and total background in events where both muons fail the isolation requirement. (b) Ratio between data and total MC samples contribution in the same* non-isolation region.

5.6.2 Isolation efficiency

In order to understand any differences between the low mass method presented above and the default Z method, a comparison between the two has been performed. Any differences are to be accounted for as a systematic uncertainty. Figure 5.16 shows the comparison between the isolation scale factors determined using the two methods, where the p_T spectrum is integrated over all values of η. The "tag" and "probe" p_T for the Z pole selection were chosen to be 20 GeV and 12 GeV respectively and the invariant mass in the range between 81 GeV and 102 GeV. All other selection

criteria are the same for the two methods. Note how the Z sample is unable to provide an estimate for muons with $p_T < 12\,\text{GeV}$ as the probe minimal p_T is 12 GeV. Furthermore the statistical error increases dramatically in the bin between 10 GeV and 15 GeV.

The comparison between the two methods shows a good agreement in all bins where the comparison is possible, within the statistical uncertainty. Therefore the overall uncertainty is dominated by the limited statistics available. The systematic error is determined by shifting the scale factors coherently by $\pm$ the statistical error which covers the systematic deviation with respect to the Z method. In Figures 5.12(a) and 5.12(b) the systematic uncertainty associated with the scale factors is shown as the shaded green area.

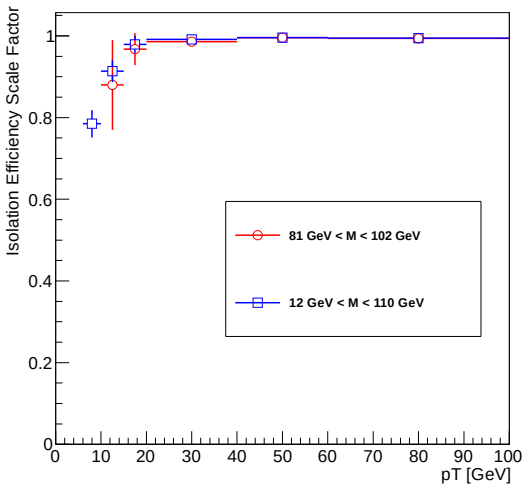

Figure 5.16: *Comparison of the isolation efficiency scale factors used in the Drell-Yan analysis with the Z tag and probe default analysis method.*

5.6.3 Trigger Efficiency

The systematic uncertainty correlated to the `EF_2mu4_DiMu` trigger efficiency is presented in Sections 4.5.1 and 4.6.1. Two independent sources of systematic uncertainty have been estimated, one associated to the `EF_mu4` efficiency, and one associated to the Vtx+OS requirement on the trigger. The uncertainty for muons of $p_T >$ 6 GeV is reported in Table 5.6.

5.6.4 Muon Momentum Resolution and Scale

The systematic uncertainty for the muon momentum smearing and energy scale has also been accounted for in the study. The main sources of uncertainties are claimed

	$\|\eta\| < 1.05$	2.1 %
EF_mu4		
	$\|\eta\| > 1.05$	0.65 %
	$\|Y\| < 1.2$	0.3 %
Vtx+OS	$1.2 < \|Y\| < 2.0$	1.0 %
	$\|Y\| > 2.0$	2.0 %

Table 5.6: *Summary of trigger efficiency systematic uncertainty associated to the* EF_2mu4_DiMu *trigger. η is the pseudo-rapidity of the offline muon, and Y is the rapidity of the Z/γ^*.*

to be the ID multiple scattering and MS alignment. The systematic uncertainty is less than 0.15% across the entire η spectrum.

Both these have been studied and the results are included in [63]. The software tool which extracts the smearing factor for each combined muon, also provides one standard deviation variation of all the parameters used in the analysis so that the source of systematic uncertainty from the momentum smearing can be propagated to the analysis and finally to the cross section measurement by increasing or decreasing each factor by its associated error.

The uncertainty on the momentum scale has been estimated as the difference in MC samples in the case when the scale is applied (this is the default setup) and the case when the scale is instead not applied.

The uncertainty on the cross section coming from these two contributions is very small, as shown in Section 6.5.

5.6.5 Reconstruction efficiency

The main sources of systematic uncertainties considered in the study of the reconstruction efficiency involve the fitting procedures used for the signal shape, the background shape and the distributions of the matched and unmatched probes to the combined muons. Details about the measurement of the overall systematic uncertainty can be found in [64, 65].

The software tool used to determine the reconstruction efficiency scale factor also returns an estimate of the systematic uncertainty for a $\pm$ one standard deviation variation. The uncertainty is approximately $\pm 0.2\%$ for $p_T > 10\,\text{GeV}$ whereas for lower transverse momentum this rises to $\pm 1.5\%$.

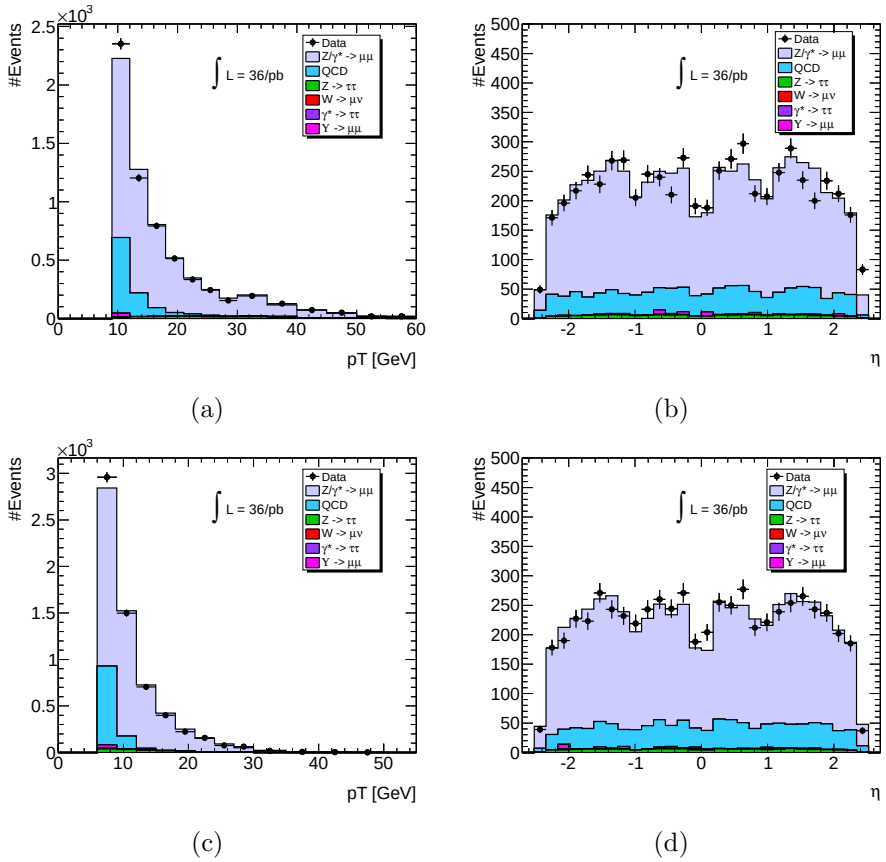

Figure 5.17: *(a) p_T and (b) η distributions corresponding to the leading muon in selected events. (c) p_T and (d) η distributions for the second muon in selected events.*

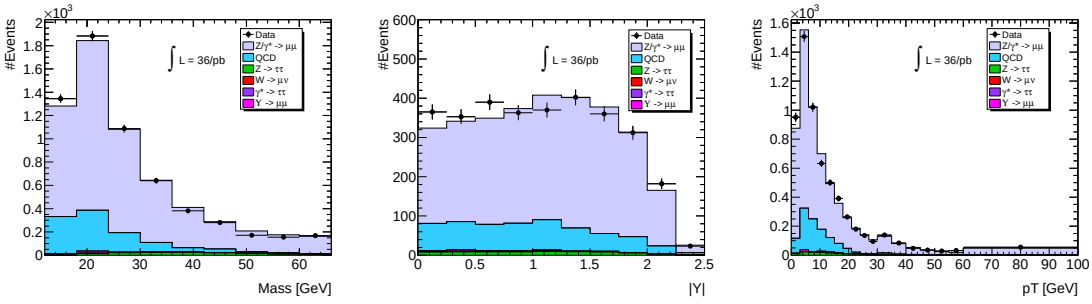

Figure 5.18: *(a) Mass, (b) absolute rapidity $|Y|$ and (c) transverse momentum p_T of the di-muon pair.*

5.7 Control distributions

Figure 5.17 shows the distributions for the p_T and η of the two muons. In Figure 5.18 the Z/γ^* mass, rapidity and transverse momentum are shown. The impact parameter distributions d_0 and z_0 respect to the primary vertex are shown in Figure

5.19. By selecting muons which are fitted to the same primary vertex, these distributions are centred around zero and fall very rapidly; for most of the muons the $|d_0|$ is less than 0.2 mm and the $|z_0|$ is less than 0.5 mm. The spatial separations in ϕ, η and R of the two muons are plotted in Figure 5.20. As can be seen in Figure 5.20(a) most of the muons are back-to-back in ϕ, but the distribution does not fall rapidly to zero. In these cases the Z/γ^* is produced with a boost, and therefore the final state muons are not completely back-to-back. The selected data is shown as well as the comparison with Monte Carlo predictions for signal and background contributions.

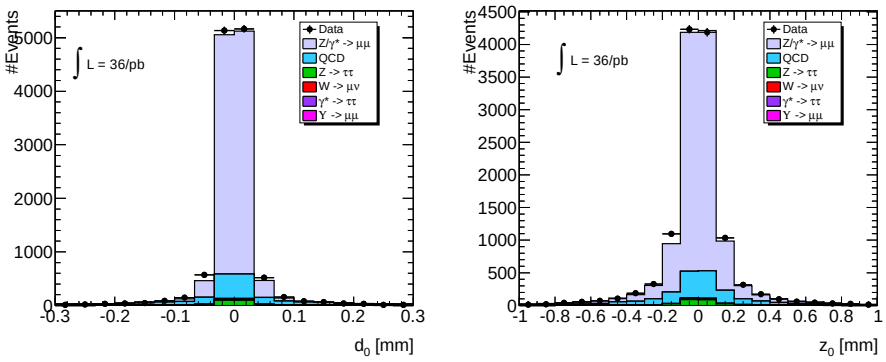

(a) (b)

Figure 5.19: *Distributions of the (a) transverse impact parameter and (b) longitudinal impact parameter of both muons.*

The event weight applied to the simulated event samples accounts for any known discrepancy with data and includes:

- the identification and reconstruction efficiency difference between data and simulation(see Section 5.5.4),
- differences in the reconstructed transverse momentum and energy scale of muons (see Section 5.5.3),
- differences in the modelling of event pile-up (see Section 5.3),
- the measured trigger efficiency (see Section 5.5.2 and Chapter 4 for details);
- differences between the isolation efficiencies in data and MC samples (see Section 5.5.1).

Furthermore, the event weight includes a luminosity scale such that every MC sample is weighted to the integrated luminosity collected in data, $\mathcal{L} = 36\,\text{pb}^{-1}$. Two extra

contributions to the event weight are taken into account, but only for selected MC samples. Each signal Drell-Yan simulated event is weighted by the NNLO k-factor as presented in Section 5.1.2, whereas a scale factor is used to correct the PYTHIA $b\bar{b}$ and $c\bar{c}$ visible cross sections to the one observed in the data. For more details on the QCD estimation and normalisation refer to Section 5.4. All of the distributions show a reasonable agreement between data and prediction.

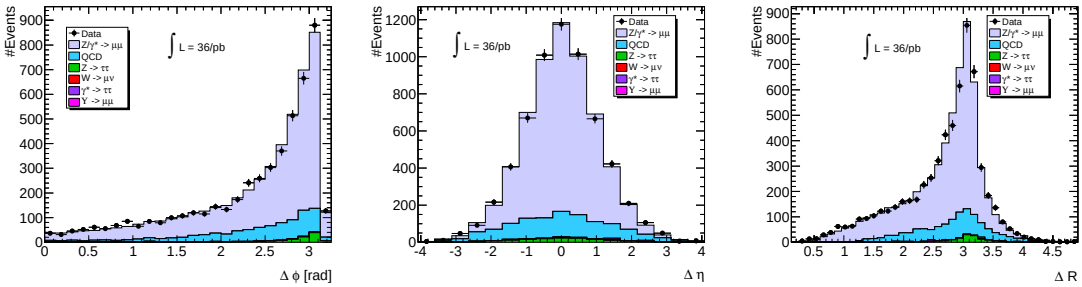

(a) (b) (c)

Figure 5.20: *Distributions of the relative (a) ϕ, (b) η and (c) R coordinate between the two muons.*

Chapter 6

Measurement of the di-muon Drell-Yan cross section in the low mass region

The analysis performed on $36\,\mathrm{pb}^{-1}$ of data collected by ATLAS in 2010 has allowed the measurement of the di-muon Drell-Yan cross section in the invariant mass range between 12 GeV and 66 GeV.

A motivation for the choice of binning scheme applied to the mass variable is presented in Section 6.1. Section 6.2 shows the details of how the differential cross section is measured within the fiducial acceptance and over the full phase space. In Section 6.3 the acceptance study is presented and the results used for the extrapolation of the cross section are detailed. Results are presented in Sections 6.4 and 6.5, for the measured cross sections, and comparisons to theoretical predictions show a reasonable agreement. The fiducial cross section measurement is dominated by the isolation and trigger efficiency uncertainties as well as the statistical uncertainty. Errors on the acceptance are dominated by the renormalisation and factorisation scale uncertainties. The total error on the measured cross sections is obtained by adding the individual sources of uncertainty in quadrature.

6.1 Binning scheme

As discussed in Chapter 1, the Drell-Yan differential cross section $d\sigma/dM$ falls sharply as the di-muon mass increases, with an approximate $1/M^3$ dependence (see Equation 1.20). Therefore the width of each mass bin is required to be small enough to reveal important features of the cross section and preserve the shape of the distribution. Furthermore the width of the bins must be large enough in order to

keep the statistical uncertainties small and to limit the effects of detector resolution smearing. This analysis is limited by the small number of expected events in the high M region, therefore the bin width must increase with increasing M.

A study has been performed elsewhere [11, 58] in order to set the number of bins to be used and their width. The binning scheme chosen for the differential cross section measurement is: $\{12,\ 17,\ 22,\ 28,\ 36,\ 46,\ 66\}$ GeV. This choice guarantees a statistical uncertainty below 5% in each bin as shown in Figure 6.1(a) where the expected uncertainty is studied as a function of the Born level M (assuming an integrated luminosity of $36\,\mathrm{pb}^{-1}$). Moreover, the binning scheme is checked to protect the analysis against the effect of bin-to-bin migration which has to be kept sufficiently small, and uniform, across the mass range. To quantify this effect a study of the purity has been performed [11, 58]. The purity is defined as:

$$P_i = \frac{N(\text{generated and reconstructed in bin } i)}{N(\text{reconstructed in bin } i,\ \text{generated anywhere})}. \tag{6.1}$$

With the binning scheme presented above, the purity is observed to be about 90%, uniformly across the entire mass region. The result of this study is shown in Figure 6.1(b). The high purity observed everywhere in the mass range considered justifies the choice of the bin-by-bin unfolding procedure adopted.

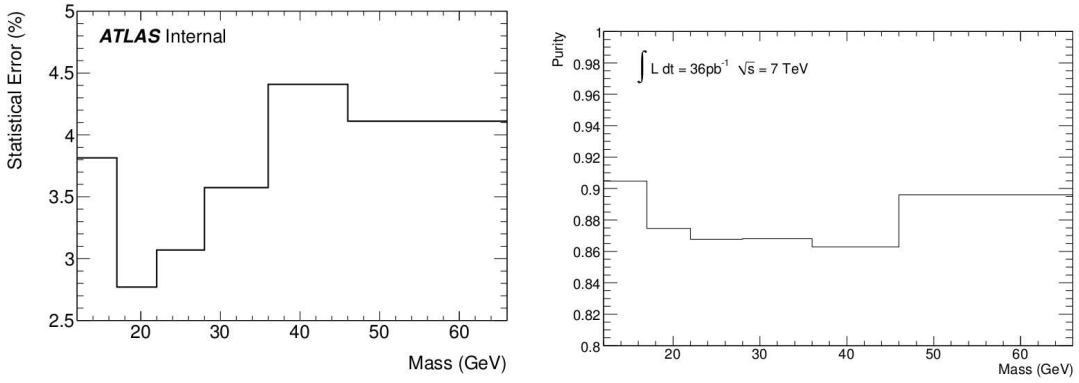

(a) (b)

Figure 6.1: *Statistical uncertainty (a) and purity (b) expected with the chosen binning scheme. The invariant mass is with respect to the Born level muons.*

6.2 Cross section calculation

The measurement of the fiducial cross section is performed within a fiducial acceptance region (also called fiducial volume) defined by constraining the p_T and η of the two final state muons within the geometrical acceptance region of the detector, the mass of the vector boson, and in some cases the p_T or rapidity of the vector boson. The extrapolated volume is obtained by correcting for the p_T and η constraints of the two final state muons.

Two different analyses have been performed. The so-called "**asymmetric analysis**" selects muons of different minimum p_T and does not require any other selection on the vector boson, except for the M constraint. Instead in the "**symmetric analysis**" muons of same minimum p_T are selected and a requirement on the rapidity of the Z/γ^* is applied. In Table 6.1 the two regions are defined for both analyses.

	Asymmetric analysis	**Symmetric analysis**
Fiducial	$p_{T,1} > 9\,\text{GeV}$, $p_{T,2} > 6\,\text{GeV}$ $\lvert\eta\rvert < 2.4$ for both muons $12 < M < 66\,\text{GeV}$	$p_{T,1} > 6\,\text{GeV}$, $p_{T,2} > 6\,\text{GeV}$ $\lvert\eta\rvert < 2.4$ for both muons $12 < M < 66\,\text{GeV}$ $\lvert Y\rvert < 2.5$
Extrapolated	$12 < M < 66\,\text{GeV}$	$12 < M < 66\,\text{GeV}$ $\lvert Y\rvert < 2.5$

Table 6.1: *Requirements defining the fiducial and extrapolated regions for the asymmetric and symmetric analyses.*

The choice of the pseudo-rapidity constraint is motivated by the performance capabilities of the ATLAS detector, i.e. the η coverage of the muon trigger system which is limited to $|\eta| < 2.4$. Furthermore, ATLAS cannot trigger on muons of p_T less than 4 GeV. The minimum p_T requirements are chosen to be above the minimum of 4 GeV in order to reduce the QCD background contribution in the low mass region and discard the threshold region where the `EF_mu4` trigger efficiency falls below 75% (see Figure 4.10). The M range is constrained to be above 12 GeV in order to avoid the upsilon resonance tail, and below 66 GeV where the measurement of the Z cross section starts. The rapidity constraint $|Y| < 2.5$ has been chosen for the symmetric analysis in order to keep the acceptance large, and allow the extrapolation of the cross section in a more constrained phase space.

The cross section unfolding procedure is performed using bin-by-bin correction factors rather than a more complex unfolding strategy. As motivated in Section 6.1, bin-to-bin migrations are found to be small enough to validate the use of this method.

Unless stated otherwise, the cross sections are measured at the Born level (as defined in Section 5.1.2). In data muons are measured at the Bare level, i.e. after QED radiation. In the cross section measurement at the Born level the correction in data from Bare to Born level is done through the C_γ factor defined below.

The fiducial bin integrated and differential cross sections measured are defined as:

$$\left(\sigma_{(pp\to Z/\gamma^*\to\mu^+\mu^-)}\right)_i^{Fid} = \frac{N_i - B_i}{\mathcal{L}\,\mathcal{C}_{\gamma^*_i}}, \tag{6.2}$$

and

$$\left(\frac{d\sigma_{(pp\to Z/\gamma^*\to\mu^+\mu^-)}}{dM}\right)_i^{Fid} = \frac{N_i - B_i}{\mathcal{L}\,\mathcal{C}_{\gamma^*_i}\,(\Delta M)_i}, \tag{6.3}$$

where M is the di-lepton invariant mass; N_i is the total number of data events in the i-th mass bin, reconstructed within the fiducial acceptance and passing all other selection criteria; B_i is the expected number of background events in the same bin; $(\Delta M)_i$ is the width of the i-th mass bin; $\mathcal{L}$ is the integrated luminosity and $\mathcal{C}_{\gamma^*_i}$ is the total signal efficiency in the i-th bin. The $\mathcal{C}_{\gamma^*}$ factor is defined as:

$$\mathcal{C}_{\gamma^*_i} = \frac{N^{MC}(\text{reconstructed and selected})_i}{N^{MC}(\text{generated})_i}, \tag{6.4}$$

where $N(\text{reconstructed and selected})_i$ is the number of Drell-Yan simulated event reconstructed and passing all selection criteria (the reconstruction and identification, trigger and isolation efficiencies are included in this factor) within the fiducial acceptance in the mass bin i and $N(\text{generated})_i$ is the number of generated (truth) Drell-Yan events which are generated in the same mass bin, within the fiducial acceptance. Figure 6.2 shows the $\mathcal{C}_{\gamma^*}$ factor used in the cross section measurement, both for the asymmetric (a) and symmetric (b) analysis. The two figures show very similar distributions: as the p_T of the muons, and therefore the invariant mass of the di-muon pair increases, the reconstruction, trigger and isolation efficiencies increase too. This results in the increase of the numerator of Equation 6.4 and therefore the overall $\mathcal{C}_{\gamma^*}$ factor.

To measure the extrapolated cross section, the correction for the geometric acceptance of the detector must be taken into account. In the asymmetric analysis the extrapolated differential cross section with respect to the di-muon invariant mass is measured by dividing Equation 6.3 by the acceptance. It is therefore defined as:

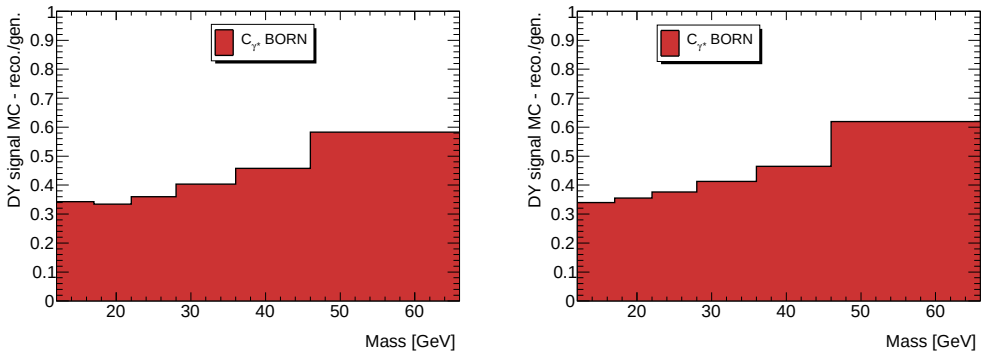

(a) (b)

Figure 6.2: *Unfolding factor $\mathcal{C}_{\gamma*}$ in bins of M. 6.2(a) for the asymmetric analysis and 6.2(b) for the symmetric analysis.*

$$\left(\frac{d\sigma_{(pp\to Z/\gamma^*\to\mu^+\mu^-)}}{dM}\right)_i^{Extra} = \frac{\left(\frac{d\sigma_{(pp\to Z/\gamma^*\to\mu^+\mu^-)}}{dM}\right)_i^{Fid}}{\mathcal{A}_i} = \frac{N_i - B_i}{\mathcal{L}\,\mathcal{A}_i\,\mathcal{C}_{\gamma*_i}\,(\Delta M)_i}, \tag{6.5}$$

where the factor $\mathcal{A}_i$ represents the geometrical acceptance in the i-th mass bin.

The extrapolated cross section determination using symmetric p_T requirements on the muons has been carried out using a different definition. A study has been performed [11] into the application of bin-centre-corrections in place of the bin-width correction being applied in the asymmetric analysis and results are applicable to the symmetric analysis. In general the bin-width correction is not recommended unless the function to be plotted $f(x)$ is linear in the variable x or considered to be linear in each bin of x [66]. This is not the case for the low mass Drell-Yan cross section since the cross section varies very rapidly over the mass range considered, especially at low masses. The differential cross section is measured in the symmetric analysis by applying a bin centre correction $\mathcal{B}_{cc}$ (in place of ΔM in Equation 6.5) obtained from a NLO or NNLO calculation and defined as:

$$\mathcal{B}_{cc} = \frac{\mathrm{d}\sigma/\mathrm{d}M}{\int \mathrm{d}M\ \mathrm{d}\sigma/\mathrm{d}M}. \tag{6.6}$$

The extrapolated Born level cross section can therefore be measured differentially in M accordingly:

$$\left(\frac{d\sigma_{(pp\to Z/\gamma^*\to\mu^+\mu^-)}}{dM}\right)_i^{Extra} = \frac{N_i - B_i}{\mathcal{L}\,\mathcal{C}_{\gamma^*_i}\,\mathcal{A}_i} \times \mathcal{B}_{cc}. \tag{6.7}$$

In summary the cross section results presented in the next sections are obtained using different approaches for the two analyses:

- **Asymmetric analysis:** the fiducial and extrapolated cross sections are measured differentially in M following the prescriptions given in Equations 6.3 and 6.5 respectively,
- **Symmetric analysis:** the VRAP program has been used to calculate the NNLO Born extrapolated differential cross section, however it is unable to provide fiducial cross sections. The fiducial bin-integrated cross section is measured as per Equation 6.2. The extrapolated differential cross section follows the recipe given in Equation 6.7.

6.3 Geometric acceptance

As mentioned in Section 6.2 the geometric acceptance allows the measurement of the cross section over the full phase space (considering muons of any transverse momentum and pseudo-rapidity) to be made within the di-muon invariant mass between 12 and 66 GeV.

The acceptance $\mathcal{A}_i$ is defined as:

$$\mathcal{A}_i = \frac{N_i^{visible}}{N_i^{total}}, \tag{6.8}$$

where $N_i^{visible}$ is the number of Monte Carlo signal events generated in bin i of the di-muon invariant mass, passing all fiducial criteria, and N_i^{total} is the total number of Monte Carlo signal events generated in the same bin, without any fiducial acceptance requirement. Only Born generator level muons are considered.

6.3.1 Asymmetric analysis

The acceptance corrections determined for the asymmetric analysis are based on the fiducial and extrapolated volume definitions given in Table 6.1.

The acceptance has been determined [67, 58] at NLO QCD using MCFM [68] interfaced with APPLgrid [69], using the MSTW2008 NLO PDF set [55], at the Born level. Figure 6.3 shows the acceptance as a function of the di-muon invariant mass using the binning scheme described in Section 6.1.

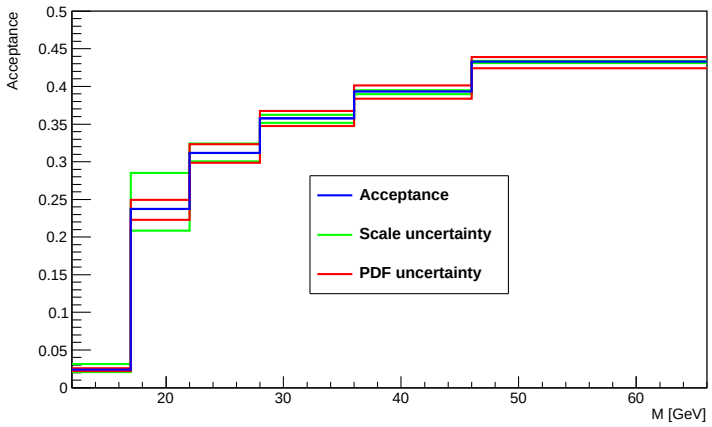

Figure 6.3: *The geometric acceptance factor $\mathcal{A}$ in bins of M used in the extrapolated cross section measurement with muons of asymmetric p_T requirements. The central value of the acceptance is shown as well as the systematic uncertainties related to the PDF error sets and scale used.*

The systematic uncertainty associated with the acceptance has also been studied. The two largest sources of systematics have been found to be the uncertainties on the PDFs and the ones on the renormalisation and factorisation scales used. Both the renormalisation scale and factorisation scale are by default chosen to be the partonic centre of mass M at the Born level. The procedure used in this study follows the prescription outlined in [70].

Statistical uncertainties associated to the acceptance have been found to be $\mathcal{O}(10)$ times smaller than the scale and PDF systematic uncertainties, therefore they are considered to be negligible. Moreover, MSTW NLO has been checked against the use of two different PDF sets, namely CT10 [71] and HERAPDF1.5 [72] (NLO). The MSTW errors are used since they are larger than the others.

Finally, a model dependency study has been carried out by comparing the results with the acceptance calculated using Pythia (LO and using NNLO k-factors). The results are found to be in agreement with the ones obtained using MCFM, within the margins of error.

The scale uncertainties have been calculated by increasing and decreasing the renormalisation and factorisation scales by a factor of two, while the calculation of the PDF uncertainties follows the MSTW PDF prescriptions outlined in [73]. A breakdown of the acceptance and associated systematic uncertainties used in the extrapolated cross section measurement is given in Table 6.2. In the two lowest mass bins the scale uncertainty is the dominant source of error, whereas for M above 22 GeV the PDF uncertainty is larger everywhere.

M [GeV]	$\mathcal{A}$	δ^-_{scale}[%]	δ^+_{scale}[%]	δ^-_{PDF}[%]	δ^+_{PDF}[%]
12-17	0.0241	-14.71	29.52	-8.97	7.07
17-22	0.2374	-12.24	20.09	-6.01	4.99
22-28	0.3115	-3.6	4.11	-4.16	3.72
28-36	0.3579	-1.71	1.19	-2.98	2.72
36-46	0.3934	-0.89	0.39	-2.48	1.97
46-66	0.4330	-0.43	0.18	-2.03	1.40

Table 6.2: *Bin-by-bin acceptance used in the asymmetric analysis. The systematic uncertainties relative to the scale and PDF used are also shown. These are expressed as a percentage of the acceptance factors.*

6.3.2 Symmetric analysis

A study has been carried out for the geometric acceptance determination relative to the symmetric analysis. The acceptance has been determined [74] using a private production LO Pythia 6.4 sample, of 10^5 events, with no fiducial requirements applied. The sample is produced using the CTEQ6.6 PDF set. Figure 6.4 shows the acceptance as a function of the di-muon invariant mass. The errors shown in the figure are only statistical; a systematic uncertainty study of scale and PDF uncertainties has not been done. Details of the acceptance and related statistical error are listed in Table 6.3 in each mass bin. Cross section results using the above setup are shown in Section 6.5.

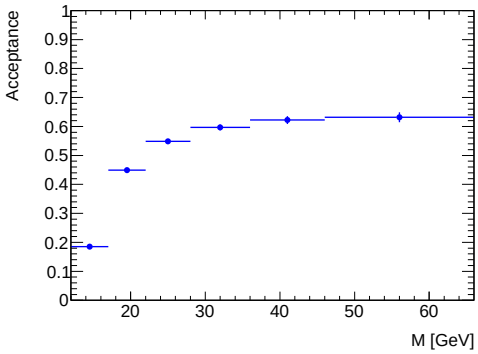

Figure 6.4: *Geometric acceptance $\mathcal{A}$ in bins of M for the symmetric analysis.*

M [GeV]	$\mathcal{A}$	δ_A^{stat}[%]
12-17	0.18	±0.3
17-22	0.45	±0.6
22-28	0.55	±0.8
28-36	0.60	±1.0
36-46	0.62	±1.4
46-66	0.63	±1.7

Table 6.3: *Bin-by-bin breakdown of the geometric acceptance use to extrapolate the symmetric analysis cross section.*

6.4 Cross section measurement: asymmetric analysis

The Born level differential fiducial cross section is shown in Figure 6.5. In (a) the measured cross section is compared to the MC@NLO simulation predictions determined at NNLO using k-factors (NLO $\rightarrow$ NNLO) obtained from `VRAP`.

The MC@NLO sample is made of three different datasets listed in Table 6.4.

Generator	M /GeV	PDF	σ_{tot} /nb	data set	ϵ_{filter}	Events
MC@NLO	10-15	CT10	2.627	113711	1	8M
MC@NLO	15-60	CT10	1.499	113712	1	8M
MC@NLO	>60	CTEQ6.6	0.953	106088	1	5M

Table 6.4: *Table of MC@NLO Monte Carlo signal samples used to compare the measured cross sections with the theoretical predictions.*

The first two samples in the table have been used before they were officially produced by the ATLAS Monte Carlo working group [75]. The generated samples (validated and later used for the official production) have been hadronised and the fiducial requirements applied in order to estimate the predicted cross section. The official datasets have the p_T and η constraints applied on both muons and therefore the total number of events is reduced to 4×10^6 and 2×10^6 for the datasets 113711 and 113712 respectively.

The comparison with the prediction from MCFM using the MSTW2008NLO PDF set is shown in Figure 6.5(b). The study of the theoretical prediction including the systematic uncertainty study is done using the same setup as in Section 6.3.1. Note that the theoretical comparison does not yet include electroweak corrections. These are estimated to be about 5% across the entire mass range considered [76]. The study performed to estimate the electroweak corrections will also be documented

in [58].

The measured cross section is in agreement with the prediction within the uncertainty.

The systematic sources of error which have been accounted for in the measured cross section in Figure 6.5 are shown in Table 6.5 for each mass bin. The uncertainties are associated to the scale factors and efficiencies used to correct the simulated event samples to better describe the data i.e. reconstruction, isolation and trigger efficiency, and QCD background. The uncertainties associated to the muon momentum resolution and scale are also considered. All the contributing factors are motivated and discussed in Section 5.6. The luminosity uncertainty for the 2010 dataset is not included in the overall uncertainty and it has been estimated to be 3.4% [77].

The central value of the cross section (in each bin of di-muon invariant mass) has been obtained taking into account the measured central value of each scale factor and efficiency considered. Moreover the cross section has been calculated two additional times for each source of uncertainty. This is done by increasing and decreasing the central value of the scale factor or efficiency by its associated error. In order to quote symmetric errors on the cross section, the largest deviation from the central value is chosen to be the systematic error on the cross section.

A graphical view of the relevant systematic uncertainties propagated through the cross section calculation is shown in Figure 6.6 as a function of the di-muon invariant mass. The total error is calculated by adding in quadrature each individual source, including the statistical error on data, listed in Table 6.6.

M [GeV]	δ^{syst}_{reco} [%]	δ^{syst}_{trig} [%] (EF_2mu4)	δ^{syst}_{trig} [%] (Vtx+OS)	δ^{syst}_{iso} [%]	δ^{syst}_{QCD} [%]	$\delta^{syst}_{Mom.Scale}$ [%]	$\delta^{syst}_{p_TSmear.}$ [%]
12-17	2.5	3.9	1.0	6.6	3.0	0.2	0.5
17-22	1.4	3.6	0.9	6.6	2.8	0.1	0.3
22-28	0.9	3.5	0.8	5.5	1.8	0.02	0.1
28-36	0.7	3.5	0.7	4.5	1.6	0.1	0.2
36-46	0.7	3.5	0.7	3.3	1.3	0.1	0.1
46-66	0.6	3.5	0.7	1.9	0.7	0.03	0.1

Table 6.5: *Bin-by-bin breakdown of the systematic uncertainties considered in the cross section measurements. The luminosity uncertainty (not included) is 3.4%.*

The breakdown of the measured differential fiducial cross section with details of each contributing factor is given in Table 6.6 where N and B are the number of signal and background events respectively. The statistical, total systematic percentage

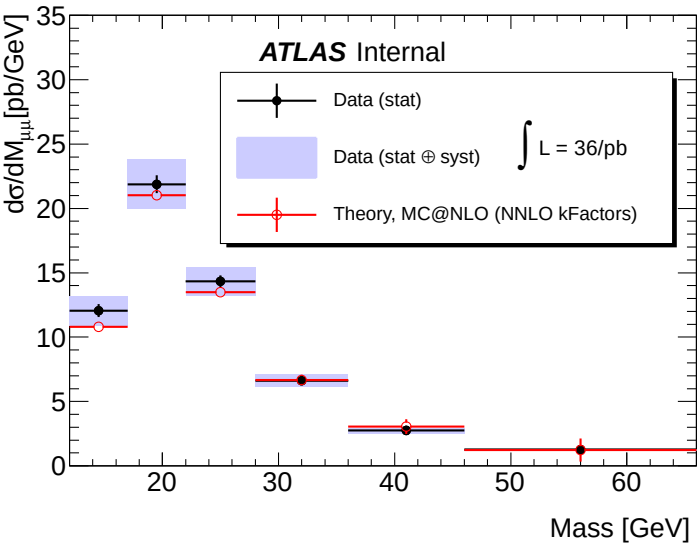

(a)

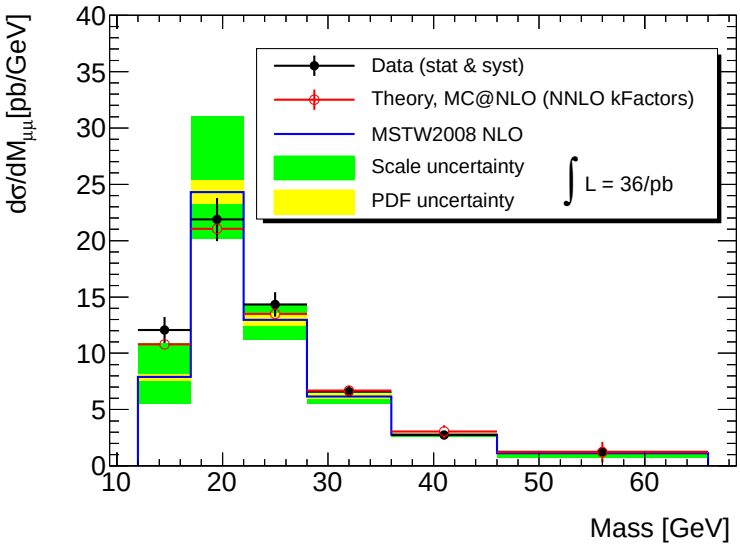

(b)

Figure 6.5: *Fiducial differential cross section at the Born level measured and compared to MC@NLO (a) and MCFM (b).*

errors and the total error (statistical and systematic added in quadrature) on the cross section are shown in separate columns.

In addition to the Born cross section, the fiducial cross section for Dressed muons has also been calculated and the correction factors with respect to the Born level are listed in Table 6.6. A Dressed lepton is defined considering the generated Born lepton after any QED radiation (this is called a Bare lepton) with the addition of all QED final state radiation (FSR) within a cone of $\Delta R < 0.1$. The FSR is simulated

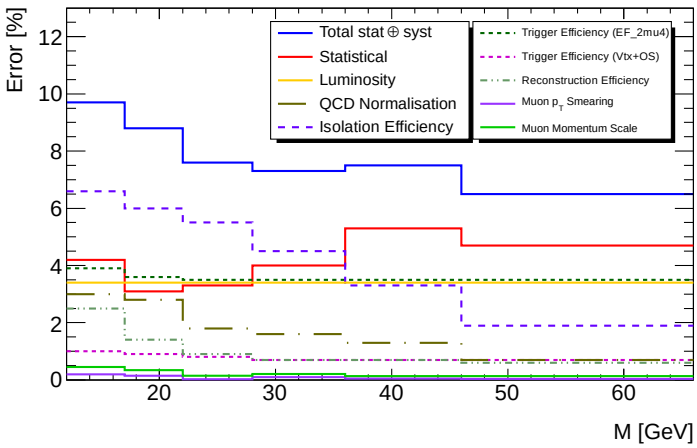

Figure 6.6: *Bin-by-bin break-down on the sources of systematic uncertainty for the cross section measurement.*

M [GeV]	N	B	$\mathcal{C}_{\gamma*}$	δ_{σ}^{stat} [%]	$\delta_{\sigma_{Fid}}^{syst}$ [%]	$\delta_{\sigma_{Fid}}^{tot}$ [%]	$\frac{d\sigma_{Fid}}{dM} \pm \delta_{\sigma_{Fid}}^{tot}$ (Born) [pb/GeV]	Dressed Correction Factors
12-17	979	236.68	0.34	4.2	8.7	9.7	12.1 ± 1.2	0.995 ± 0.006
17-22	1706	390.84	0.33	3.1	8.2	8.7	21.9 ± 1.9	0.983 ± 0.003
22-28	1342	230.74	0.36	3.3	6.9	7.6	14.3 ± 1.1	0.983 ± 0.004
28-36	927	161.23	0.40	4.0	6.1	7.3	6.6 ± 0.5	0.988 ± 0.005
36-46	555	103.23	0.46	5.2	5.3	7.4	2.7 ± 0.2	1.016 ± 0.006
46-66	600	77.74	0.58	4.7	4.5	6.5	1.3 ± 0.1	1.162 ± 0.007

Table 6.6: *Bin-by-bin breakdown of the differential fiducial cross section measured at the Born level. The Dressed correction factors (and the associated statistical uncertainties) are also given. The Luminosity uncertainty is not included.*

by PHOTOS [78]. A correction factor is determined by taking the ratio of the truth Dressed level predictions to the Born level ones, in each bin of the di-muon invariant mass [79]. In both cases only the fiducial volume selection is applied. Therefore the Dressed cross section is measured by applying a bin-by-bin correction factor to the Born level results. Figure 6.7(a) shows the correction factors, where the errors represent the statistical uncertainty in the MC samples. The differential fiducial cross section with Dressed level muons is shown in Figure 6.7(b) together with the MC@NLO theoretical comparison made using the samples listed in Table 6.4 with Dressed corrections applied.

As already mentioned the extrapolation of the cross section to the full phase space is done according to Equation 6.5, where the fiducial cross section is corrected by the geometric acceptance shown in Figure 6.3. Figure 6.8 shows the extrapolated Born level differential cross section, both on a linear and logarithmic scale. The

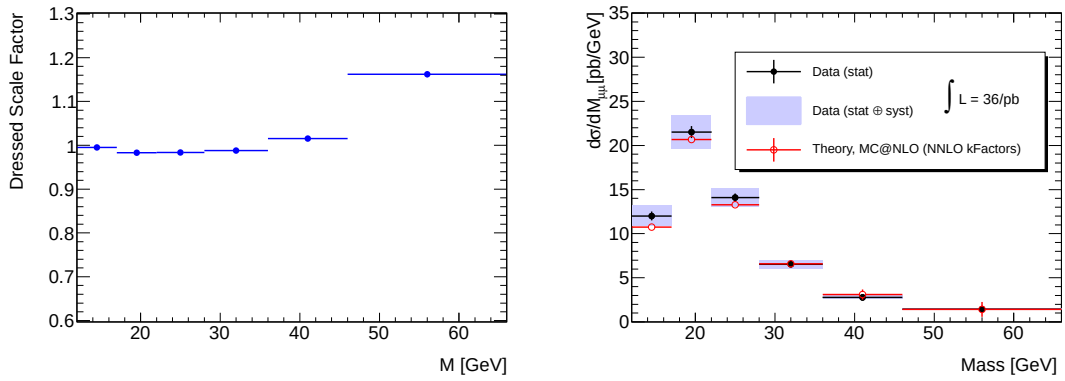

(a) (b)

Figure 6.7: *Correction factors for the Dressed level cross section measurement (a) and Dressed level fiducial differential cross section measured and compared to MC@NLO (b).*

details of the results and acceptance systematic uncertainties propagated to the cross section measurement are reported in Table 6.7. As for the other systematic uncertainties on the cross section, here the PDFs and scale errors are propagated through the cross section measurement, and the largest deviation in each bin quoted as symmetric uncertainty. The total error is calculated by adding in quadrature each individual source, which include also all of the ones listed in Table 6.5.

M [GeV]	Acc	$\delta^{syst}_{Acc(Scale)}$ [%]	$\delta^{syst}_{Acc(PDF)}$ [%]	δ^{stat}_{σ} [%]	$\delta^{syst}_{\sigma_{Extra}}$ [%]	$\delta^{tot}_{\sigma_{Extra}}$ [%]	$\frac{d\sigma_{Extra}}{dM} \pm \delta^{tot}_{\sigma_{Extra}}$ [pb/GeV]
12-17	0.0241	22.8	9.9	4.2	26.3	26.7	500.5 ± 133.4
17-22	0.2374	16.7	6.4	3.1	19.7	19.9	92.1 ± 18.4
22-28	0.3115	4.0	4.4	3.3	9.1	9.7	46.0 ± 4.4
28-36	0.3579	1.7	3.1	4.0	7.0	8.1	18.5 ± 1.5
36-46	0.3934	0.9	2.5	5.2	5.7	7.7	7.0 ± 0.5
46-66	0.4330	0.4	2.1	4.7	4.7	6.6	2.9 ± 0.2

Table 6.7: *Bin-by-bin breakdown of the extrapolated differential Born level cross section. The acceptance is also given, with the relative errors on the cross section.*

Figure 6.9 summarises all the main steps of the differential cross section measurement, showing the number of data events collected normalised by the integrated luminosity, the background subtracted data, the fiducial cross section and the extrapolated one. The measured cross sections are in this case compared to the Pythia predictions (shown with a solid line in the figure). The ratio between the measured and the predicted fiducial cross section shows a good agreement between the two, within the uncertainties.

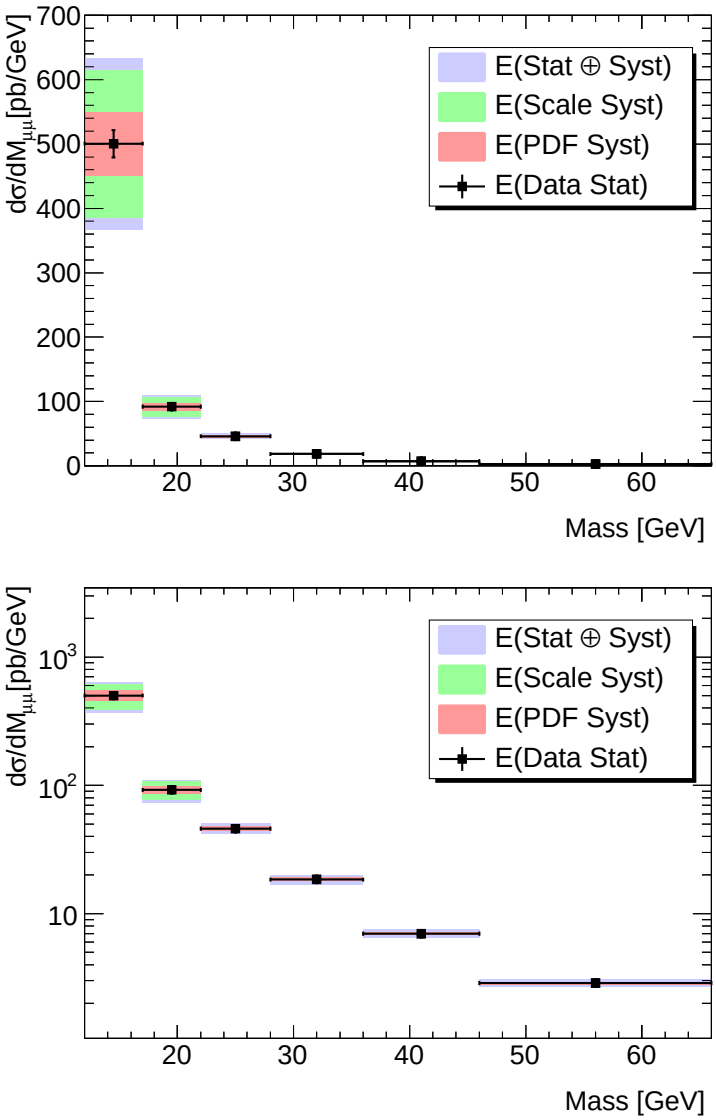

Figure 6.8: *Extrapolated Born level differential cross section (asymmetric analysis).*

6.5 Cross section measurement: symmetric analysis

The asymmetric analysis measurement presented in the previous section has been performed in order to compare with more stable theoretical predictions. In fact theoretical calculations of the Drell-Yan cross section at NLO and NNLO are expected to be unstable in the region where the minimum lepton p_T is about the same as half of the di-lepton invariant mass i.e. $2p_T \sim M$. This is because the phase-space limits the real NLO corrections, therefore virtual corrections are not fully cancelled. In some cases this can lead to large negative and therefore unphysical cross section

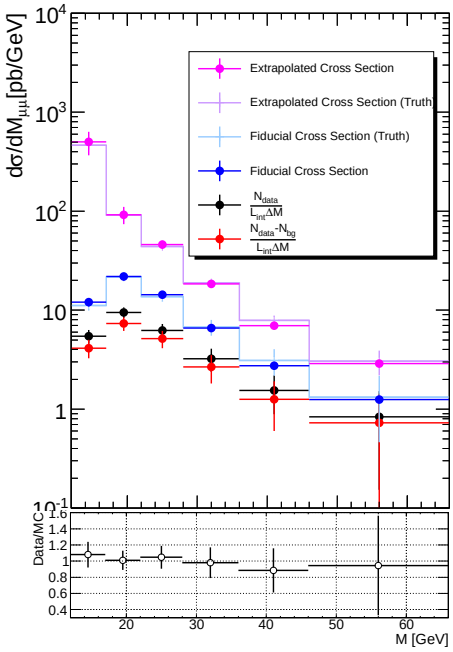

Figure 6.9: *Summary of all the main steps of the differential cross section measurement. The ratio between the measured fiducial cross section and the predicted one is shown at the bottom of the plot.*

predictions [80]. Table 6.8 shows the predicted cross section with symmetric minimum p_T requirements on the muons set to 6 GeV [67]. Note that the scale error decreases by a factor of ten in the second mass bin compared to the first bin in the table. Also, the cross section prediction for the symmetric analysis should be larger than the ones for the asymmetric analysis, because of the lower leading muon p_T. This is not the case in the second mass bin between 17 and 22 GeV. Here the asymmetric analysis prediction is $\frac{d\sigma_{Fid}}{dM} = 24.29$. Considering only the second mass bin the MCFM prediction results would imply that:

$$\begin{aligned}
&\frac{d\sigma_{Fid}}{dM}(p_{t,1} > 6\,\text{GeV}, p_{t,2} > 6\,\text{GeV}) - \frac{d\sigma_{Fid}}{dM}(p_{t,1} > 6\,\text{GeV}, p_{t,2} > 9\,\text{GeV}) \\
&= \frac{d\sigma_{Fid}}{dM}(p_{t,1} > 6\,\text{GeV}, 6 < p_{t,2} < 9\,\text{GeV}) \\
&= 23.35 - 24.29 = -0.94 < 0\,,
\end{aligned}$$

leading to a negative predicted cross section. The symmetric analysis explores this region of phase space. Before presenting the cross section results, an outline of the measurement is given and the main control distribution are shown.

The MC samples for signal and background used are the same as for the asymmetric analysis and are listed in Tables 5.1 and 5.2 respectively. All the selection

M [GeV]	$\frac{d\sigma_{Fid}}{dM}(MCFM)$	δ^-_{scale}[%]	δ^+_{scale}[%]	δ^-_{PDF}[%]	δ^+_{PDF}[%]
12-17	15.29	-110.26	28.84	-5.87	6.17
17-22	23.35	-13.20	6.14	-4.70	4.88
22-28	12.68	-13.19	5.57	-4.45	4.59
28-36	6.09	-11.60	4.65	-4.26	4.32
36-46	2.75	-9.87	3.77	-4.09	4.05
46-66	1.14	-7.98	3.78	-3.87	3.74

Table 6.8: *MCFM prediction for the fiducial differential cross section with symmetric minimum muon p_T requirement. The Scale and PDF uncertainties are expressed as a percentage of the cross section in each mass bin.*

criteria are identical as in Section 5.2.1, except for the minimum p_T requirement on the muons, which is set to 6 GeV. The NNLO k-factors are applied to the signal Drell-Yan simulated event samples as in the asymmetric analysis. Although the k-factors are evaluated both at NLO and NNLO, the calculation does not give unphysical results (as in the case of fiducial cross section NLO calculations with symmetric requirements on the minimum p_T). This is because `VRAP` makes a calculation in the extrapolated volume, and does not limit the fiducial volume in p_T for example.

The QCD background normalisation has been estimated with the symmetric requirements, following the same procedure as in Section 5.4.3. All other efficiencies and scale factors are applied to each event and the overall event weight is (as before) the product of all individual weights.

Figure 6.10 shows the p_T and η distributions of the two selected muons, whereas the mass, rapidity and p_T spectrum of the Z/γ^* are shown in Figure 6.11. The simulated event samples show a reasonable agreement with the data. Details about the number of selected events after each applied selection criteria are shown in Table 6.9. As in Section 5.2, the preselection includes the GRL selection (data only), the requirement that at least one primary vertex has been reconstructed in the event and at least three tracks fitted to it, the event contains at least two combined `Muid` muons, and that event has been triggered (data only, MC samples are scaled by the trigger efficiency derived in data). Table 6.10 shows the number of events selected after each requirement as a percentage with respect to the previous selection criteria. Note how the requirement on the rapidity of the vector boson to be constrained in the region $|Y| < 2.5$ does not reduce the number of selected events for data or for any of the MC samples. This is due to the requirement on the pseudo-rapidity range of the muons i.e. $|\eta| < 2.4$. This constrains the vector boson in the region of rapidity $|Y| < 2.5$.

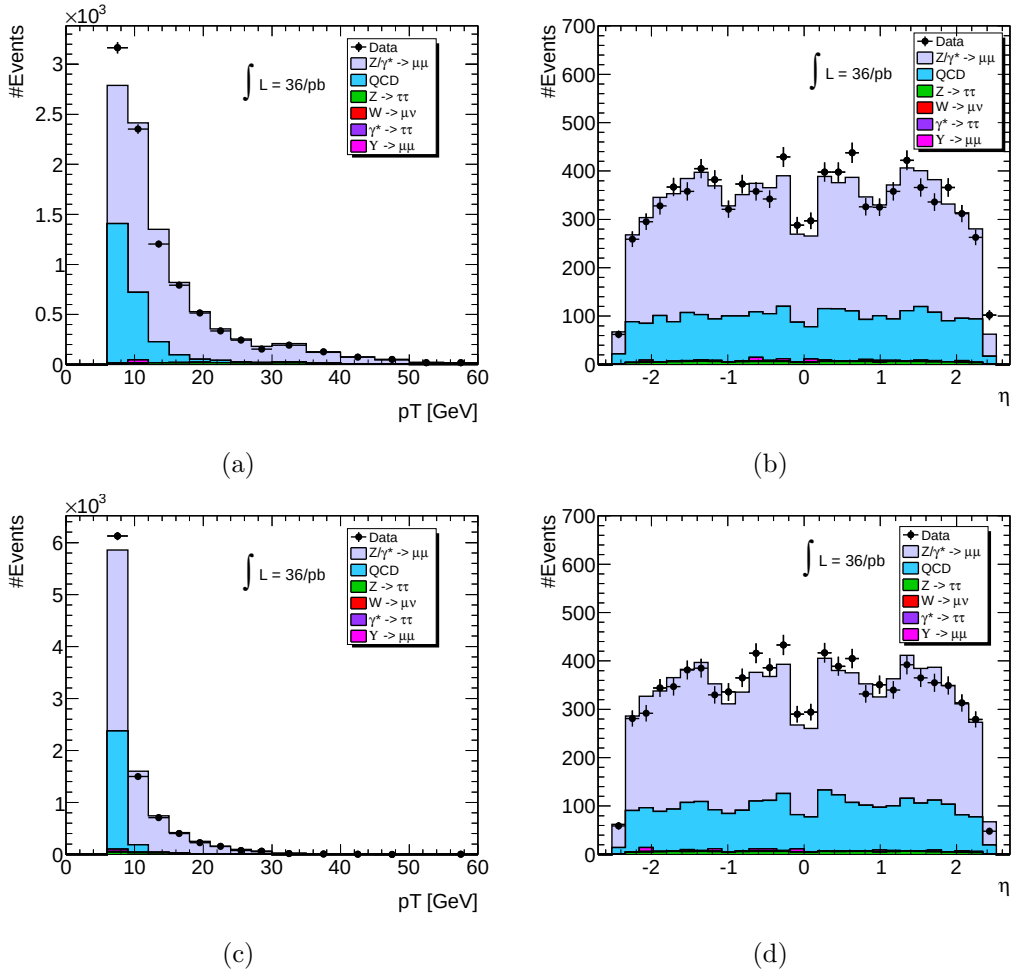

Figure 6.10: *(a) p_T and (b) η distributions for the leading muon in all selected events. (c) p_T and (d) η distributions for the second muon in all selected events.*

The ratio between the number of data events and the total number of MC events selected is about one, for the asymmetric and symmetric analysis. However the ratio between signal and background is very different between the two analyses (Signal/Background = 4.1 and 2.5 in the asymmetric and symmetric analysis respectively). This is expected and is due to the lower minimum p_T requirement in the symmetric analysis. The region of low p_T is where the large contribution of the QCD background is selected.

Figure 6.12 shows the bin-integrated fiducial Born level cross section compared to predictions from the MC@NLO simulation[1] (including NNLO k-factors obtained from `VRAP`). A breakdown of the results in each bin of mass is shown in Table 6.11. The table also contains information on the total uncertainty on the measurement.

[1]The MC@NLO sample used is the same presented in Section 6.4 and also used to compare the asymmetric analysis results.

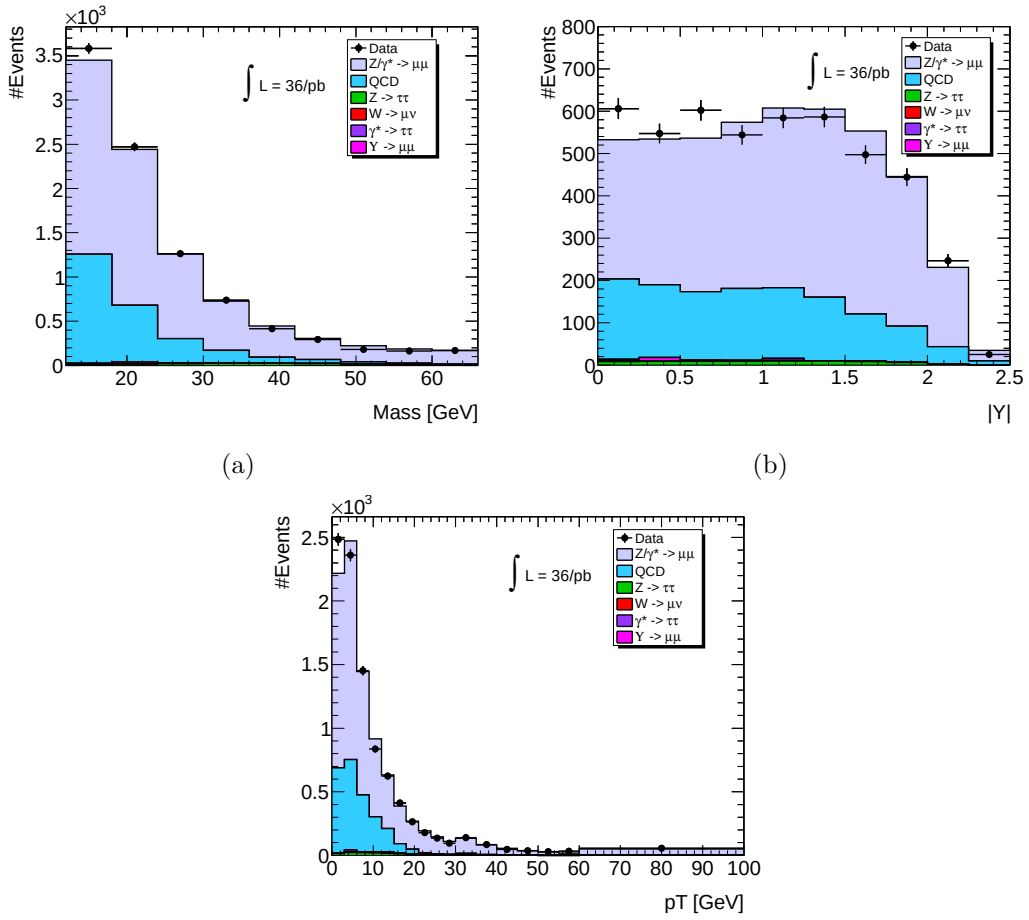

Figure 6.11: *(a) Mass, (b) absolute rapidity $|Y|$ and (c) transverse momentum p_T distribution of the $Z/\gamma*$.*

Cut	Data	Drell-Yan	QCD	$Z \to \tau\tau$ $M > 60$ GeV	$Z/\gamma \to \tau\tau$ $10 < M < 60$ GeV	$W \to \mu\nu$	$\Upsilon \to \mu\mu$	Total MC
Preselection	1026519	30162	415120	279	51	680	512129	958421
Good quality muons	948836	29249	369489	267	48	579	495545	895177
$p_T, \|\eta\|$	209379	20823	230794	214	20	273	36202	288326
OS	207160	20808	127627	208	19	198	35975	184835
Y	207160	20808	127627	208	19	198	35975	184835
$12 < M < 66$ GeV	82902	8933	72517	198	16	153	223	82040
Isolation	**9274**	**6557**	**2444**	**141**	**10**	**14**	**45**	**9211**

Table 6.9: *Cut flow table showing the number of events passing each of the selection criteria listed.*

Note that the bin integrated fiducial cross section is measured in this case, and not the differential cross section as in the asymmetric analysis. This has already been mentioned in Section 6.2.

The sources of systematic uncertainty considered for the measurement are the

Cut	Data	Drell-Yan	QCD	$Z \to \tau\tau$ $M > 60$	$Z/\gamma \to \tau\tau$ $10 < M < 60$	$W \to \mu\nu$	$\Upsilon \to \mu\mu$
Preselection	-	-	-	-	-	-	-
Good quality muons	92.4	97.0	89.0	95.7	95.0	85.1	96.8
$p_T, \lvert\eta\rvert$	22.1	72.9	62.5	80.2	40.6	47.2	7.3
OS	98.9	99.9	55.3	97.1	95.7	72.6	99.4
Y	100	100	100	100	100	100	100
$12 < M < 66\,\text{GeV}$	40.0	39.5	58.8	95.2	85.4	77.1	0.6
Isolation	11.1	73.4	3.4	71.1	63.1	9.31	20.1

Table 6.10: *Cut flow table showing the percentage of events passing each cut, for the symmetric p_T analysis. The percentage is with respect to the previous cut.*

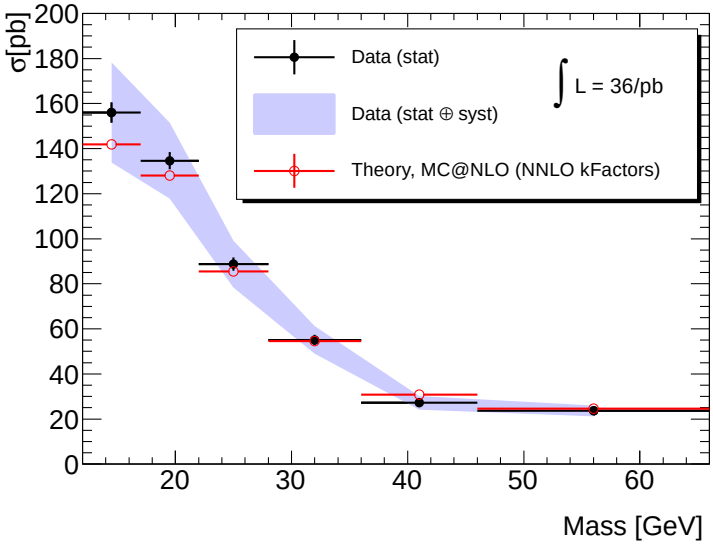

Figure 6.12: *Fiducial bin-integrated Born level cross section for the symmetric analysis. The shaded band represents the total uncertainty.*

M [GeV]	N	B	$\mathcal{C}_{\gamma*}$	δ_{σ}^{stat} [%]	$\delta_{\sigma_{Fid}}^{syst}$ [%]	$\delta_{\sigma_{Fid}}^{tot}$ [%]	$\sigma_i^{Fid} \pm \delta_{\sigma_{Fid}}^{tot}$ [pb]
12-17	2979	1073.63	0.34	±2.9	±13.7	±14.0	156.0 ± 22.2
17-22	2418	698.99	0.36	±2.9	±12.2	±12.5	134.6 ± 16.9
22-28	1586	387.07	0.38	±3.3	±11.2	±11.7	88.7 ± 10.4
28-36	1071	253.40	0.41	±4.0	±10.4	±11.1	55.1 ± 6.1
36-46	596	142.10	0.46	±5.4	±9.8	±11.2	27.2 ± 3.0
46-66	624	95.53	0.62	±4.8	±8.9	±10.1	23.6 ± 2.4

Table 6.11: *Bin-by-bin breakdown of the bin-integrated fiducial cross section measurement with details of each factor contributing. The Luminosity uncertainty is not included in the total uncertainty quoted.*

M [GeV]	δ^{syst}_{reco} [%]	δ^{syst}_{trig} [%] (EF_2mu4)	δ^{syst}_{trig} [%] (Vtx+OS)	δ^{syst}_{iso} [%]	δ^{syst}_{QCD} [%]
12-17	3.9	5.5	1.0	11.5	2.9
17-22	1.7	3.9	0.9	10.8	1.8
22-28	1.1	3.0	0.8	10.1	1.3
28-36	0.8	2.6	0.7	9.4	1.0
36-46	0.8	2.2	0.7	8.75	0.9
46-66	0.9	1.0	0.7	8.1	0.8

Table 6.12: *Bin-by-bin breakdown of the systematic uncertainties propagated to the cross section measurement. The Luminosity uncertainty is not included.*

same as for the asymmetric analysis, and they are listed in Table 6.12 where their impact on the cross section uncertainty is obtained. Although the use of looser p_T requirement on the muons reduces the statistical error on data, other systematic uncertainties are larger in this analysis. The reconstruction, isolation and the EF_mu4 trigger efficiencies error on the cross section are larger, since the leading muon is allowed to have a lower p_T, falling in the region of larger uncertainties for all of these contributing efficiencies. The Vtx+OS trigger efficiency remains identical as in the asymmetric analysis. This is because the scale factor is applied as a function of the rapidity of the vector boson, and not of the p_T of the muons. Finally the systematic error on the cross section arising from the QCD normalisation increases, since the amount of QCD background is larger in the symmetric analysis due to the lower p_T minimum requirement on the leading muon. As for in the previous section, all of the systematic sources of error and the statistical uncertainty on data are added in quadrature in order to obtain the total uncertainty on the measured cross section.

Figures 6.13(a) and 6.13(b) show the extrapolated Born level differential cross section evaluated at the middle point of each mass bin (see Equation 6.7), on a linear and logarithmic scale respectively. The comparison done using VRAP with NNLO k-factors shows the measured cross section in good agreement with the prediction, within the margins of error. Table 6.13 contains a breakdown on the measurement at each chosen value of the Z/γ^* mass. The VRAP predictions are also detailed in the table.

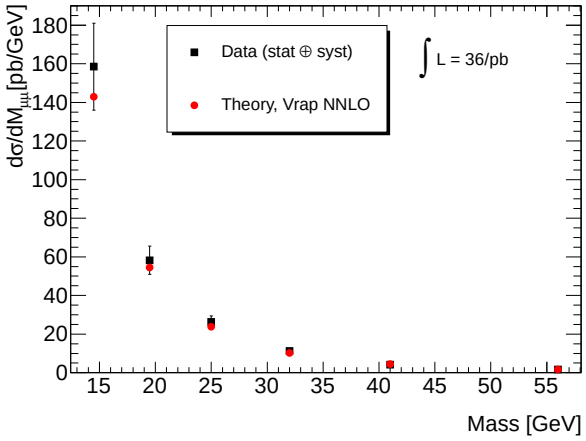

(a)

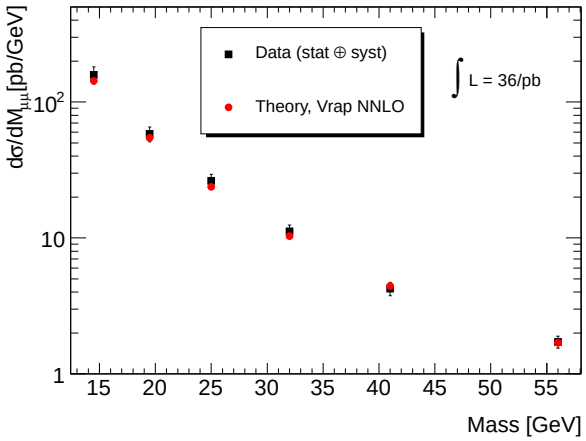

(b)

Figure 6.13: *Extrapolated Born level differential cross section for the symmetric analysis.*

M [GeV]	$\mathcal{B}_{cc}$	δ_{σ}^{stat} [%]	$\delta_{\sigma_{Extra}}^{syst}$ [%]	$\frac{d\sigma_{Extra}}{dM} \pm \delta_{\sigma}$[pb/GeV]	VRAP $\frac{d\sigma}{dM}$ [pb/GeV]
14.5	0.19	±2.9	±14.2	158.5 ± 22.5	142.8
19.5	0.19	±2.9	±12.6	58.2 ± 7.3	54.9
25	0.16	±3.3	±11.7	26.3 ± 3.1	23.8
32	0.12	±4.0	±11.2	11.2 ± 1.3	10.3
41	0.096	±5.4	±11.2	4.2 ± 0.5	4.4
56	0.045	±4.8	±10.2	1.7 ± 0.2	1.7

Table 6.13: *Bin-by-bin breakdown of the extrapolated differential cross section. The systematic uncertainties are also shown.*

Chapter 7

Conclusions

The Drell-Yan cross-section in proton-proton collisions depends on the Parton Distribution Functions (PDFs) for the proton. It is an important measurement to make at the LHC and ATLAS, where a new kinematic region of momentum fractions x and momentum transfer Q is accessible; the measurement could help to further constrain the PDFs. Most of the work presented in this thesis focuses on the measurement of the low mass Drell-Yan cross section $pp \to Z/\gamma^* \to \mu^+\mu^-$ in the di-muon channel with the ATLAS detector, using the $36\,\text{pb}^{-1}$ of integrated luminosity collected in 2010. The region of mass studied ranges between 12 and 66 GeV.

The trigger efficiency is one of the most important studies for the cross section measurement, since the Drell-Yan process at low masses is populated by soft muons of low p_T in the trigger threshold region. A data driven method has been implemented to measure the `EF_2mu4_DiMu` trigger efficiency. The efficiency of `EF_mu4` reaches about 80% and 95% for muons above $\approx$8 GeV in the Barrel and Endcap region respectively. The efficiency of the χ^2 of the vertex fit and opposite sign requirement on the trigger measured with respect to the di-muon pair rapidity, ranges from about 98% at di-muon rapidity of about zero and about 90% at rapidity of about 2.5.

Another important aspect of the measurement is the QCD background estimated to contribute to the cross section. This is the largest background in the low mass region. The normalisation is obtained using a data driven technique which employs the contribution of both heavy flavour and light flavour QCD processes, and relies on the fact that muons from Drell-Yan events, unlike QCD events, are well isolated. The isolation variables have been studied in detail and a very harsh requirement has been adopted in the analysis. The efficiency of the isolation has been estimated and scale factors determined in order to correct the simulated event samples for any differences. Other minor sources of background have also been taken into account.

The differential cross section measured, with respect to the di-muon invariant mass, at the Born level, has been measured in two different fiducial volumes and the results are in agreement with theoretical predictions within the margin of error. The mass binning scheme chosen for the cross section measurement is {12, 17, 22, 28, 36, 46, 66} GeV.

The luminosity uncertainty in 2010 is estimated to be 3.4%. The factors contributing to the systematic uncertainty in order of relevance are: the isolation and trigger efficiencies, the QCD background normalisation, the muon reconstruction efficiency and the muon momentum resolution and scale. The last two contributions are very small.

The asymmetric analysis applies different minimum p_T requirements on the muons of 6 and 9 GeV, and the $|\eta| < 2.4$ constraint. The signal-to-background ratio, after all requirements are applied, is about 4.1. The uncertainty ranges between 4.2% (stat.) and 8.7% (syst.) in the lowest mass bin, and 4.7% (stat.) and 4.5% (syst.) in the highest mass bin. In the low mass region between 12 and 17 GeV the measured differential cross section in mass is $\frac{d\sigma^{fid}}{dM}$[pb/GeV] = 12.1 ± 0.5 (stat.) ± 1.1 (syst.) ± 0.4(lumi.); instead in the highest mass bin between 46 and 66 GeV is $\frac{d\sigma^{fid}}{dM}$[pb/GeV] = 1.3 ± 0.1 (stat.) ± 0.1 (syst.) ± 0.05 (lumi.)

The fiducial bin integrated cross section has been measured for the symmetric analysis in which both muons are selected with a minimum p_T requirement of 6 GeV and $|\eta| < 2.4$. The signal-to-background ratio has been estimated to be 2.5, after all requirements have been applied.

The uncertainly ranges between 2.9% (stat.) and 13.7% (syst.) in the lowest mass bin, and 4.8% (stat.) and 8.9% (syst.) in the highest mass bin. In the lowest mass bin the measured cross section is $d\sigma^{fid}$ [pb] = 156.0 ± 4.5 (stat.) ± 21.3 (syst.) ± 5.3 (lumi.), whereas in the highest mass bin is $d\sigma^{fid}$ [pb] = 23.6 ± 1.1 (stat.) ± 2.1 (syst.) ± 0.8 (lumi.).

The systematic uncertainty has been determined considering the same factors as for the asymmetric analysis, except for the muon momentum and scale uncertainties which are negligible.

For both symmetric and asymmetric analyses the differential extrapolated cross section at the Born level has also been measured. The results are in agreement when compared to the theoretical prediction. Dressed correction factors have also been calculated for both analyses.

The Lorentz angle measurement for the ATLAS SCT has also been presented. Various studies have been performed using cosmic data such as the dependence of the Lorentz angle on the hit pattern and the voltage dependence. A first measure-

ment using 2010 collision data has also been performed with a new track selection optimised for collision data. A discrepancy between the model prediction and the measured Lorentz angle is observed.

Bibliography

[1] E. Lobodzinska, and S. Glazov, *Deutsches Elektronen-Synchrotron (DE)*, private communication.

[2] *CERN Accelerator Complex*, http://faculty.physics.tamu.edu/kamon/research/refColliders/LHC/2008_LHC_First_Beam/.

[3] D. Froidevaux, and P. Sphicas, *GENERAL-PURPOSE DETECTORS FOR THE LARGE HADRON COLLIDER*, Annu. Rev. Nucl. Part. Sci. **56**(2006) 375–440.

[4] *Computer generated image of the ATLAS inner detector*, http://cdsweb.cern.ch/record/1095926.

[5] *ATLAS SCT Gallery*, http://atlas.web.cern.ch/Atlas/GROUPS/INNER_DETECTOR/SCT/gallery/barrel_modules/barrelmodule.jpg.

[6] The ATLAS Collaboration, *Commissioning of the ATLAS Muon Spectrometer with cosmic rays*, Eur. Phys. J. **C70** (2010) 875–916.

[7] F. Bauer, *et al.*, *The first precision drift tube chambers for the ATLAS muon spectrometer*, Nucl. Instrum. Meth. **A478** (2002) 153–157.

[8] The ATLAS Collaboration, *Trigger Performance - Technical Design Report* (1998).

[9] *Luminosity Public Results*, https://twiki.cern.ch/twiki/bin/view/AtlasPublic/LuminosityPublicResults#Publications_and_Conference_Resu.

[10] *Data Quality Information for 2010 and 2011 Data*, https://twiki.cern.ch/twiki/bin/view/AtlasPublic/RunStatsPublicResults2010.

[11] R. Hickling, *PhD student at Queen Mary, University of London*, private communication.

[12] *ATLAS Experiment - Public results*, https://twiki.cern.ch/twiki/bin/view/AtlasPublic/EventDisplayPublicResults#11_vertices.

[13] C. Jacoboni, *et al.*, *A Review of some Charge Transport Properties of Silicon*, Solid State Electonics **20** (1977) 77.

[14] C. Anastasiou, *et al.*, *High precision QCD at hadron colliders: Electroweak gauge boson rapidity distributions at NNLO*, Phys. Rev. **D69** (2004) 094,008.

[15] J. Beringer, *et al.*, *Particle Data Group - 2012 Review of Particle Physics*, Phys. Rev. **D86** (2012) 010001.

[16] *Latest update in the search for the Higgs boson*, https://indico.cern.ch/conferenceDisplay.py?confId=197461.

[17] *SLAC Home Page*, http://www.slac.stanford.edu/.

[18] *HERA Home Page*, http://adweb.desy.de/mpy/hera/.

[19] M. Breidenbac, *et al.*, *Observed Behavior Of Highly Inelastic Electron-Proton Scattering*, Phys. Rev. Lett. **23** (1969) 935.

[20] R. K. Ellis, *et al.*, *QCD and Collider Physics*, Cambridge University Press, 1996.

[21] W. A. Bardeen, *et al.*, *Deep-inelastic scattering beyond the leading order in asymptotically free gauge theories*, Phys. Rev. **D18** (1978) 3998.

[22] Y. L. Dokshitzer, *Calculation Of The Structure Functions For Deep Inelastic Scattering And e^+e^- Annihilation By Perturbation Theory In Quantum Chromodynamics.*, Soviet Physics, JETP [Zh. Eksp. Teor. Fiz. **73** (1977) 1216] **46** (1977) 641.

[23] V. N. Gribov, and L. N. Lipatov, *e^+e^- Pair Annihilation And Deep Inelastic ep Scattering In Perturbation Theory*, Yad. Fiz. [Sov. J. Nucl. Phys. **15** (1972) 675] **15** (1972) 1218.

[24] V. N. Gribov, and L. N. Lipatov, *Deep Inelastic ep Scattering In Perturbation Theory*, Yad. Fiz. [Sov. J. Nucl. Phys. **15** (1972) 675] **15** (1972) 718.

[25] G. Altarelli, and G. Parisi, *Asymptotic Freedom In Parton Language*, Nucl. Phys. **B126** (1977) 298.

[26] R. Devenish, and A. Cooper-Sarkar, *Deep Inelastic Scattering*, Oxford University Press, 2004.

[27] W. F. G. Curci, and R. Petronzio, *Evolution of Parton Densities Beyond Leading Order: The Nonsinglet Case*, Nucl. Phys. **B175** (1980) 27.

[28] S. M. A. Vogt, and J. A. M. Vermaseren, *The Three-loop splitting functions in QCD: The Singlet case*, Nucl. Phys. **B691** (2004) 129.

[29] J. C. Collins, *et al.*, *Factorization of Hard Processes in QCD*, Adv. Ser. Direct. High Energy Phys. [hep-ph/0409313] **5** (1988) 1.

[30] J. M. Campbell, *et al.*, *Hard interactions of quarks and gluons: a primer for LHC physics*, Rep. Prog. Phys. **70** (2007) 89.

[31] W. L. van Neerven, and E. B. Zijlstra, *The $\mathcal{O}(\alpha_s)$ corrected Drell-Yan K-factor in the DIS and $\overline{\rm MS}$ schemes*, Nucl. Phys. **B382** (1992) 11, [Erratum-ibid.B 680 (2004) 513].

[32] L. Dixon, *A program for computing rapidity distributions for production of lepton-pairs via virtual photons, W or Z bosons at hadron colliders at NNLO in QCD [Online]* (2010), [Cited: July 2010], http://www.slac.stanford.edu/lance/Vrap/.

[33] The ATLAS Collaboration, *The ATLAS experiment at the CERN Large Hadron Collider*, JINST **3** (2008) S08003.

[34] The ALICE Collaboration, *The ALICE experiment at the CERN LHC*, JINST **3** (2008) S08002.

[35] The CMS Collaboration, *The CMS experiment at the CERN LHC*, JINST **3** (2008) S08004.

[36] The LHCb Collaboration, *The LHCb Detector at the LHC*, JINST **3** (2008) S08005.

[37] The ATLAS Collaboration, *Expected Performance of the ATLAS Experiment*, arXiv:0901.0512, CERN-OPEN-2008-020 (2008).

[38] *ATLAS Experiment - Good Run Lists for Analysis*, `https://twiki.cern.ch/twiki/bin/viewauth/AtlasProtected/GoodRunListsForAnalysis`.

[39] E. Coniavitis, *et al.*, *Lorentz Angle and Cluster Width Studies for the ATLAS SCT*, ATLAS note **ATL-COM-INDET-2009-039** (2009).

[40] M. Bona, *et al.*, *Lorentz Angle Analysis and Measurement for the ATLAS SCT*, ATLAS note **ATL-COM-INDET-2011-114** (2011).

[41] T. A. Collaboration, *The ATLAS Experiment at the Large Hadron Collider*, JINST 3 S08003 (2008) 53–109.

[42] S. Haywood, *Local Coordinate Frames for the Alignment of Silicon Detectors*, ATLAS note **ATL-COM-INDET-2004-001** (2004).

[43] S. Gadomski, *Model of the SCT detectors and electronics for the ATLAS simulation using Geant4*, ATLAS note **ATL-SOFT-2001-005** (2001).

[44] W. Shockley, *Electrons and holes in semiconductors*, Van Nostrand, Princeton N.J., 1950.

[45] T. Lari, *Lorentz Angle Variation with Electric Field for ATLAS Silicon Detectors*, ATLAS note **ATL-INDET-2001-004** (2001).

[46] T. Cornelissen, *et al.*, *The Measurement of Cosmic-Ray Time with the Transition Radiation Tracker*, ATLAS note **ATL-COM-INDET-2010-045** (2010).

[47] *ATLAS Luminosity Calculator*, `https://atlas-lumicalc.cern.ch/`.

[48] *ATLAS Muon Combined Performance - Guidelines for Analysis in Release 16*, `https://twiki.cern.ch/twiki/bin/viewauth/AtlasProtected/MCPAnalysisGuidelinesRel16`.

[49] The ATLAS Collaboration, *Tracking Results and Comparison to Monte Carlo simulation at* $\sqrt{s} = 900$ *GeV*, ATLAS note **ATLAS-CONF-2010-011** (2010).

[50] J. Kirk, *STFC - Science and Technology Facilities Council (GB)*, private communication.

[51] T. Bold, *AGH University of Science and Technology (PL)*, private communication.

[52] T. Sjöstrand, *et al.*, *PYTHIA 6.4 Physics and Manual*, JHEP **05** (2006) 026.

[53] S. Frixione, and B. R. Webber, *Matching NLO QCD Computations and Parton Shower Simulations*, JHEP **06** (2002) 029.

[54] P. M. Nadolsky, *et al.*, *Implications of CTEQ global analysis for collider observables*, Phys. Rev. **D78** (2008) 013004, [arXiv:0802.0007 [hep-ph]].

[55] A. D. Martin, *et al.*, *Parton Distributions for the LHC*, Eur. Phys. J. **C63** (2009) 189–285.

[56] A. Sherstnev, and R. Thorne, *Parton Distributions for LO Generators*, Eur. Phys. J. **C55** (2008) 553–575.

[57] `http://pprc.qmul.ac.uk/~hickling/kGridV4Ratio.html`.

[58] M. Corradi, *et al.*, *Measurement of the low mass Drell-Yan differential cross section with the ATLAS detector*, ATLAS note **ATL-COM-PHYS-2012-966** (2012).

[59] The ATLAS Collaboration, *Measurement of the $W \to \ell\nu$ and $Z/\gamma^* \to \ell\ell$ production cross sections in proton-proton collisions at $\sqrt{s}$ = 7 TeV with the ATLAS detector*, JHEP **12** (2010) 60.

[60] *Pileup Performance*, `https://twiki.cern.ch/twiki/bin/viewauth/Atlas/PileupPerformance`.

[61] The ATLAS Collaboration, *A measurement of the total W and Z/γ^* cross sections in the e and μ decay channels and of their ratios in pp collisions at $\sqrt{s}$= 7 TeV with the ATLAS detector*, ATLAS note **ATLAS-CONF-2011-041** (2011).

[62] M. Aharrouche, *et al.*, *Total and differential W→lnu and Z→ll cross-sections measurements in proton-proton collisions at sqrts =7 TeV with the ATLAS Detector*, ATLAS note **ATL-COM-PHYS-2011-751** (2011).

[63] The ATLAS Collaboration, *Muon Momentum Resolution in First Pass Reconstruction of pp Collision Data Recorded by ATLAS in 2010*, ATLAS note **ATLAS-CONF-2011-046** (2011).

[64] The ATLAS Collaboration, *Muon reconstruction efficiency in reprocessed 2010 LHC proton-proton collision data recorded with the ATLAS detector*, ATLAS note **ATLAS-CONF-2011-063** (2011).

[65] The ATLAS Collaboration, *A measurement of the ATLAS muon reconstruction and trigger efficiency using J/psi decays*, ATLAS note **ATLAS-CONF-2011-021** (2011).

[66] G. Lafferty, and T. Wyatt, *Where to stick your data points: The treatment of measurements within wide bins*, Nucl. Instrum. Meth. **A355** (1995) 541–547.

[67] E. Yatsenko, and S. Glazov, *Deutsches Elektronen-Synchrotron (DE)*, private communication.

[68] J. M. Campbell, and R. K. Ellis, *MCFM for the Tevatron and the LHC*, arXiv:1007.3492. FERMILAB-CONF-10-244-T (2010).

[69] T. Carli, *et al.*, *A posteriori inclusion of parton density functions in NLO QCD final-state calculations at hadron colliders: The APPLGRID Project*, Eur. Phys. J. **C66** (2010) 503–524.

[70] U. Klein and V. Radescu, *Guidance for scale choices and an estimate of their uncertainties*, ATLAS note **ATL-COM-PHYS-2012-419** (2012).

[71] H. L. Lai, *et al.*, *New parton distributions for collider physics*, Phys. Rev. **D82** (2010) 074024.

[72] *H1 and ZEUS Collaborations, preliminary result*, `http://www-h1.desy.de/publications/H1preliminary.short_list.html`.

[73] A. Martin, *et al.*, *Parton distributions for the LHC.*, Eur. Phys. J. **C63** (2009) 189–285.

[74] J. Goddard, *PhD student at Queen Mary, University of London*, private communication.

[75] *ATLAS Monte Carlo Working Group*, `https://twiki.cern.ch/twiki/bin/viewauth/AtlasProtected/MonteCarloWorkingGroup`.

[76] U. Klein, *EW corrections for ATLAS Drell-Yan measurements. Presented at "Working Group on Electroweak precision measurements at the LHC, and PDF4LHC"*, `https://indico.cern.ch/conferenceOtherViews.py?view=standard&confId=203748`.

[77] The ATLAS Collaboration, *Improved Luminosity Determination in pp Collisions at sqrt(s) = 7 TeV using the ATLAS Detector at the LHC*, ATLAS note **ATLAS-DAPR-2011-01-001** (2012).

[78] E. Barberio, and Z. Was, *PHOTOS: A Universal Monte Carlo for QED radiative corrections. Version 2.0*, Comput. Phys. Commun. **79** (1994) 291.

[79] J. Lilley, *Research associate at Queen Mary, University of London*, private communication.

[80] S. Frixione, and G. Ridolfi, *Jet photoproduction at HERA*, Nucl. Phys. **B507** (1997) 315–333.